UNIVERSIDAD AUTÓNOMA DE MADRID

Facultad de Ciencias

Departamento de Química Inorgánica

Nanoscale Coordination Polymers with Molecular Recognition. From Nanocarriers and Selective Separations to Inks for 3D Printing

Tesis presentada por

Verónica García Vegas

para optar al grado de Doctora en Química Aplicada

Directores de tesis

Pilar Amo Ochoa **Félix Zamora Abanades**

Madrid, 2021

CONTENTS

ABSTRACT

Coordination polymers are well-known compounds based on the self-assembly of metal ions and organic and inorganic ligands. However, the combination between metals and ligands is so versatile that not all the possibilities have already been studied. The use of nucleobases as ligands in combination with copper(II) as the metal ion is the thread of the work developed in the last four years, in which new potential biological applications for coordination polymers have been described.

The first chapter introduces the world of coordination polymers. Including a brief description of the evolution of these compounds from their first steps to current research, their design and principal obtention methods, their most characteristic properties and some applications related to the following chapters.

In Chapter 2, the synthesis at room temperature of a new nanoscale coordination polymer is described, including the process from single crystal obtention at high temperature and pressure to nanoscaling the compound under mild conditions. Then the combination between size and properties of the synthesized coordination polymer with a nucleobase derivative as ligand allows its study as oligonucleotide carrier.

Chapter 3 continues the study of the coordination polymer obtained in the previous chapter. The described synthesis of the nanoscale compound is transferred to a larger scale, enabling the use of this

compound in the industry as an ink for 3D printing. In addition, a deep study of the structure of the coordination polymer reveals its potential use as humidity sensor.

In Chapter 4, the rational design of two new coordination polymers is reported. Two isostructural compounds are synthesized with nucleobase derivatives with the difference that one of them is also the derivative from an anticancer agent. Complementary studies of their behavior in biological media and their cytotoxicity are carried out.

Finally, the last chapter introduces a new coordination polymer that is capable of changing from colloid to gel with a slight variation in the synthetic conditions. A later treatment of the gel enables to obtain new materials such as an aerogel or a xerogel. The properties of the aerogel and the potential of the structure with a nucleobase derivate ligand is studied as stationary phase of an HPLC column.

RESUMEN

Los polímeros de coordinación son compuestos basados en el autoensamblaje de iones metálicos y ligandos orgánicos y/o inorgánicos. Estos compuestos llevan años estudiándose, pero la combinación entre metales y ligandos es tan amplia que todavía es un campo con múltiples posibilidades. El hilo conductor del trabajo de estos últimos cuatro años son los polímeros de coordinación con centro metálico de cobre(II) y nucleobases como ligando principal, la combinación de ambos nos lleva al desarrollo de nuevos materiales con potenciales aplicaciones biológicas.

El primer capítulo es una introducción al mundo de los polímeros de coordinación. Esto incluye un breve repaso de la historia de estos compuestos, desde los primeros hallazgos a la situación actual de los mismos. Esta introducción también hace un repaso por el diseño y los principales métodos de obtención de los polímeros de coordinación, así como sus principales propiedades y algunas de las aplicaciones que se describen en los capítulos siguientes.

El capítulo 2 describe la síntesis a temperatura ambiente de un nuevo polímero de coordinación de tamaño nanométrico. La síntesis incluye el proceso desde la obtención de monocristales con altas temperaturas y presiones hasta el nanoescalado en condiciones suaves. Así la combinación entre el tamaño y las propiedades del nuevo polímero de coordinación que tiene como ligando un derivado de nucleobase permite llevar a cabo su estudio como portador de oligonucleótidos.

En el capítulo 3 continúa el estudio del polímero de coordinación sintetizado en el capítulo anterior. Concretamente se describe la inusual síntesis de un polímero de coordinación de tamaño nanométrico a gran escala, lo que permite su uso a escala industrial como tinta de impresión 3D. Además, un estudio más completo de la estructura de este polímero de coordinación revela su potencial uso como sensor de humedad.

El capítulo 4 recoge el diseño y obtención de dos nuevos polímeros de coordinación. Estos compuestos son isoestructurales y ambos tienen como ligando un derivado de nucleobase con la diferencia de que uno de ellos es además un derivado de un agente anticancerígeno. Una vez sintetizados y caracterizados ambos compuestos, se estudia su comportamiento en medios biológicos y la toxicidad que presentan en células.

Por último, el quinto capítulo introduce un nuevo polímero de coordinación que es capaz de cambiar su forma de coloide a gel con una pequeña modificación en las condiciones de síntesis. Además, dependiendo del tratamiento que se le dé al gel se pueden obtener nuevos materiales como un aerogel o un xerogel. Todos estos materiales se caracterizan y se aprovechan las propiedades del aerogel junto con la estructura del polímero de coordinación para estudiar su comportamiento como fase estacionaria de una columna de HPLC.

CHAPTER 1. INTRODUCTION

1.1. Coordination Polymers

Coordination chemistry comprises those compounds with a central atom (usually a metal cation) joined to ligands (that can be organic molecules or inorganic anions) through coordination bonds. Many of them are present in nature, such as hemoglobin, vitamin B12, or pigments and they were described before they were recognized as coordination compounds[1,2]. The history of coordination compounds had a turning point with the contribution of Alfred Werner, who defined and established the basis of coordination chemistry and was awarded with the Nobel Prize in chemistry in 1913. He was capable of identifying the terms now known as oxidation state and coordination number and defined the linkage of atoms in coordination compounds, which represented a breakthrough in inorganic chemistry[3].

Based on Werner's basic concept and modern coordination theory, various kinds of coordination compounds have been prepared and synthesized, such as coordination polymers. The term "coordination polymer" was used for the first time in 1916 and it can be defined as extended arrays based on self-assembly processes of metal centers and organic or inorganic ligands to create polymeric structures which extend in one, two, or three dimensions (Figure 1.1). However, this area began to grow in the 1990s with the contribution of seminal work by Robson[4,5], followed by important developments by Kitagawa and Yaghi, who demonstrated that it was possible to synthesize

families of compounds systematically with specific structural topologies[6,7]. These advances allowed the understanding of the effect of structure, chemical functionality, or porosity in the versatile coordination framework structures. Combining the properties of metals and ligands, the obtained structures can show cooperative properties such as magnetism, molecular recognition, electrical conductivity, or luminescence that turn them into multifunctional materials with application in different areas[8–11]. Properties of CPs can be easily tuned by the structural architecture and they are directly related to their application[12]. Obtaining CPs with one or more physico-chemical properties makes these functional materials good candidates for common applications such as drug delivery, catalysis, gas storage[13–15], and more original ones like 3D printing or optoelectronic devices[16,17]. Thus, structure, properties, and applications have a close relationship among them. In this way, those CPs with a 3D architecture and cavities in their structure are named Metal Organic Frameworks (MOFs). This type of materials has grown in the last years thanks to applications such as gas storage, purification, and separation or catalysis, that facilitate progress in current problems like air pollution[7,18,19].

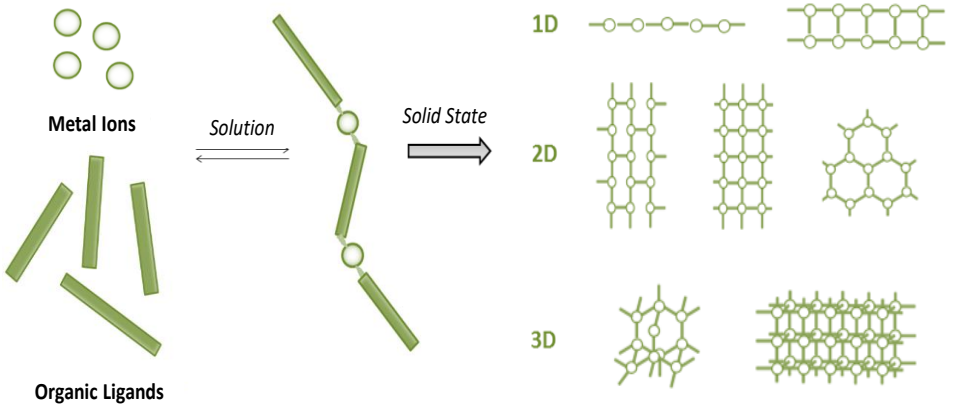

Figure 1.1. Schematic representation of coordination polymers formation.

1.2. Design and Synthesis of Coordination Polymers

Creating new coordination polymers is not fully predictable because the self-assembly process to obtain a supramolecular structure happens in a spontaneous way. However, coordination polymers have a crystalline nature that involves a direct relation between chemical composition and structure and if attention is paid to the different combinations between the building blocks, their possible interactions, and the desired properties, a set of probable structures can be predicted[20]. Knowing these structures, it can be seen if any of them is likely to display the desired property. However, the architecture of coordination polymers depends also on other factors like synthetic methods or chemical aspects such as kinetic and thermodynamic stability of the final compound.

1.2.1. Crystal engineering

Crystal engineering is the branch of chemistry that studies the intermolecular interactions of crystal structures and their relationship with the chemical and physical properties of crystalline materials to design new solids with targeted properties[21]. The crystal structure is the internal periodic structure that describes the ordered arrangement of molecules, atoms, or ions connected by intermolecular forces forming a regular infinite network. Understanding the arrangement of molecules and their possible interactions is the key to control the properties of materials[22].

This field plays an important role in the design of new functional materials like coordination polymers and MOFs. The terminology of crystal engineering applied to coordination polymers gives, as a result, the division in *synthons* and *tectons*[23]. Synthons are defined as spatial arrangements of interactions between the ligands through coordination bonds. Although there are other weaker synthons in the coordination polymer arrays, like hydrogen bonds or π-π interactions, that can generate an overall 3D net from a 1D one, the infinite array is defined by coordination bonds. *Tectons* are considered the building blocks used to create the structure, ligands, and metal ions for coordination polymers.

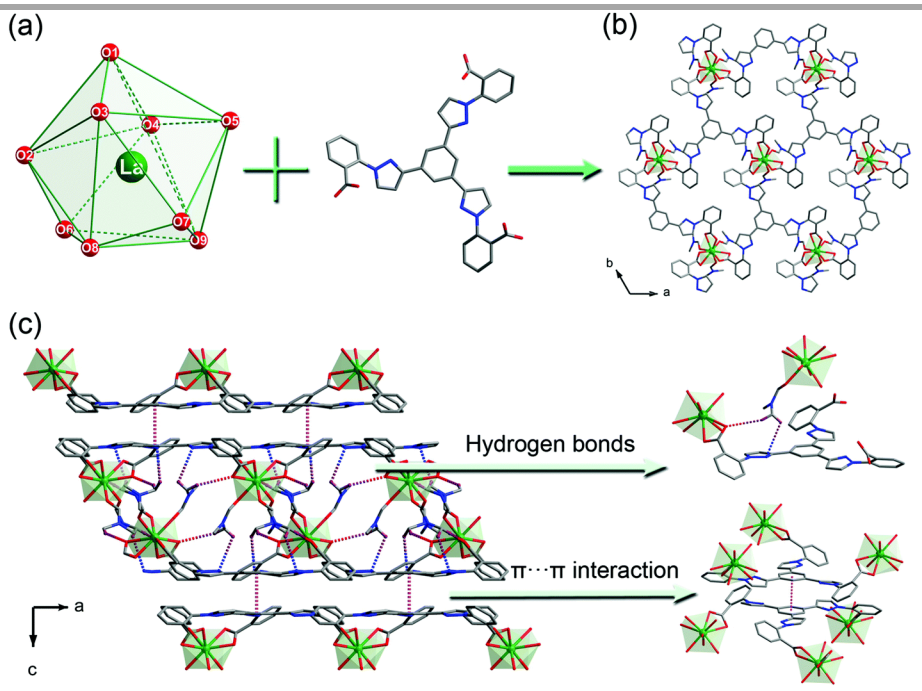

Figure 1.2. Representation of *synthons* and *tectons* in a coordination polymer. Adapted from Reference 23.

The design of these materials starts with defining the desired network topology by an appropriate selection of building blocks[6]. Building blocks are principally chosen by geometry and individual properties[12]. Different arrangements can be obtained depending on the number and orientation of the donor atoms in ligands and the coordination number of the metal ions. However, the structure does not depend only on geometric patterns, it will also be affected by secondary interactions such as hydrogen bonding or π–π stacking interactions, the size and electronic configuration of metal ions or donor-acceptor capacity, size or flexibility of connecting ligands. All these variables allow the synthesis of different one (1D)-, two (2D)- and three-dimensional (3D) architectures.

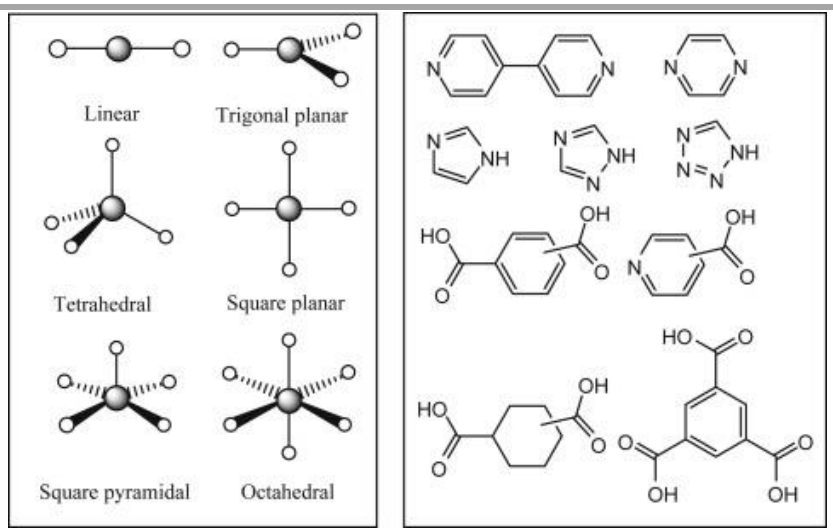

Figure 1.3. Typical coordination geometries of d-block metal ions (left) and multitopic ligands (right). Adapted from Reference 12.

Early in the 90's Robson was the pioneer to approach the crystal structure as a modular concept with metal ions like nodes of a network and ligands like the linkers that connect these nodes simplifying the solid design[4]. Applying this strategy implies knowing the usual coordination geometries of metal ions and the preferred coordination modes of ligands and allow their classification in molecular libraries based on the number of binding positions and their angle (Figure 1.3).

In this context, Yaghi introduced the term *reticular chemistry* to describe the process of linking rigid molecular building blocks, which maintain their geometry during the reaction, by strong bonds to metals to form predetermined ordered structures[24]. This assembly allows the control of the construction of frameworks because the molecular building blocks have a clearly defined structure and geometry, and the strong bonds provide architectural and chemical stability throughout extended structures. This approach is principally used in the construction of porous materials like metal-organic frameworks, whose development has generated the concept of secondary building units (SBUs)[25]. SBUs are rigid and directional clusters in which the flexibility around the metal ion is locked and the points of extension of the cluster are defined by the geometry of the units (Figure 1.4). This modular architecture enables to design and classify the MOF structures into their underlying topology.

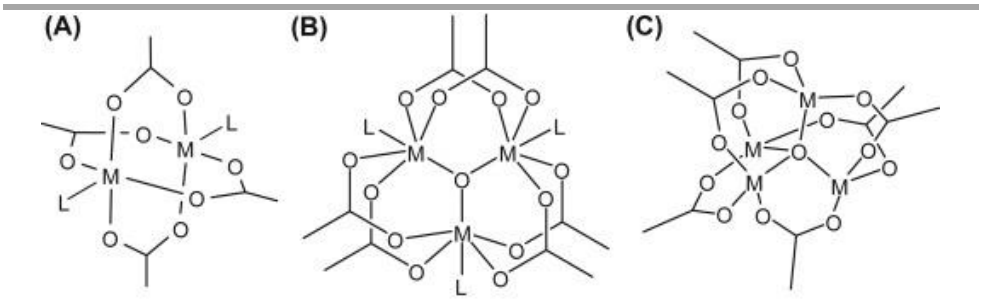

Figure 1.4. Three well-known metal-cluster SBUs. Adapted from Reference 24.

1.2.2. Synthesis of Coordination Polymers

The obtention of single crystals is the first objective in coordination polymer synthesis because with them it is possible to solve the crystal structure using single-crystal X-ray diffraction (SCXRD) and therefore to know the distribution of the building blocks in the resulting material. Once a coordination polymer is formed, it is difficult to recrystallize them because they are usually insoluble, so the formation of high-quality single crystals during the synthesis process turns into a necessary challenge[26].

There are several methods with the potential to yield single crystals. The simplest is a conventional synthesis mixing the building blocks in a solvent. Then, crystallization is triggered in the resulting solution by supersaturating it, either by solvent evaporation or solution cooling. In another approach, supersaturation is achieved by exposing the mixture to another solvent in which the solubility of the coordination polymer is reduced. The controlled addition of the so-called anti-solvent forms an interface where the crystal growth is favored. If it is a volatile solvent, vapor diffusion will be preferentially used. In case

of poorly soluble products, liquid-liquid diffusion is common, in which the building blocks are dissolved in two separate solutions and mixed slowly by the addition of one reactant(s) solution to the other. Then, the diffusion of the reagents through the interface allows a slow and controlled reaction (Figure 1.5).

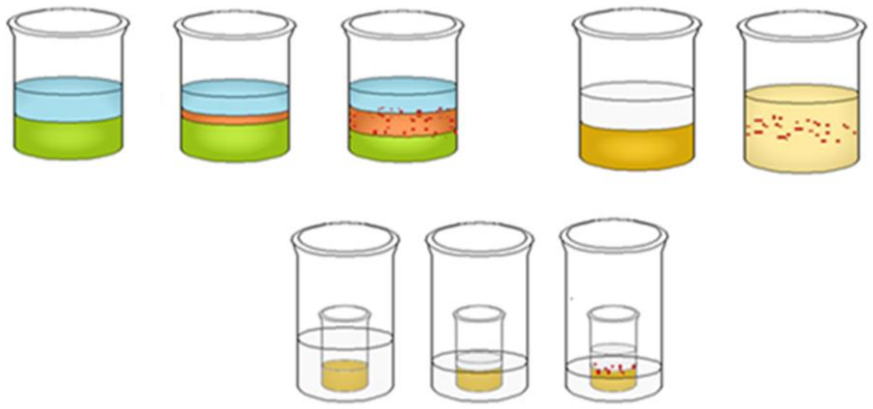

Figure 1.5. Schematic representation of three different methods of crystallization by diffusion.

The previous methods are based on supersaturation and slow mixing of building blocks. However, it is possible to change the reaction conditions to obtain crystals. Solvothermal synthesis is an experimental technique in which the mixture of building blocks and solvent(s) is added to a sealed reactor and heated beyond the boiling point of the solvent increasing the autogenous pressure in the reactor. Once higher pressures and temperatures are used, some properties of the solvents such as density or viscosity radically change favoring the reactivity and the crystallization of poorly soluble compounds. It is possible to reduce reaction times and increase

product yields with microwave-assisted solvothermal synthesis, but this technique usually produces smaller crystals, which limits the study of new products.

1.2.3. Reaction Conditions

The final structure of coordination polymers is affected by several physical and chemical factors including the influence of solvent, temperature, pH value, or stoichiometry.

The solvent plays an important role in synthesis. Different factors can influence the selection of the solvent, being the solubilization of the starting reactants the principal. However, there are other factors such as searching for sustainable solvents or how the solvent can interact with the coordination polymer, becoming part of the structure as a ligand or being trapped inside the pores. Nowadays a principal focus of attention is the environment, so it is expected that the obtention of new materials tries to be as sustainable as possible, which in the case of coordination polymers, affects the selection of building blocks and solvents based on the principles of *green chemistry*[27], being the most common solvents water or ethanol. On the other hand, the influence that the solvent can exert over coordination polymers is well-known[28]. The donor atoms present in solvents favor their coordination to metal centers, turning the solvent into another potential ligand, although sometimes the coordination polymer is obtained directly from the reaction, in other cases an exchange between a ligand from the coordination sphere and the molecules of the solvent present in the media is performed, which

results in a new structure. When the solvent acts as a ligand, its influence over the structure can be reflected in the dimensionality of the coordination polymer or in its properties[29] (Figure 1.6).

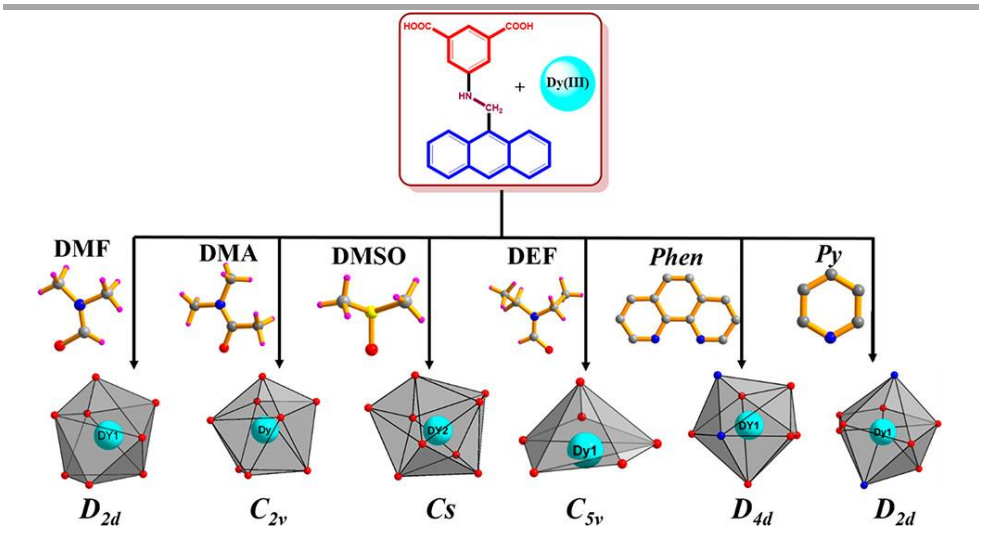

Figure 1.6. Reaction between Dy(III) and 5-[(anthracen-9-ylmethyl)-amino]-isophthalic acid using different solvents and the resulting coordination spheres around the metal center[29].

Solvents can also be part of the structure as host molecules in porous coordination polymers, so the crystal structure can be determined by the size or the polarity of the solvent molecules. This effect can be observed in the case of two polymorphous MOFs obtained by the reaction between a Cu(II) salt and a linear tetracarboxylate ligand and whose topology differs depending on the solvent. If the solvent is *N,N*-dimethylacetamide (DMA), the result is a 3D structure with **fof** topology, meanwhile if the solvent is a mixture of dimethylformamide (DMF), dioxane, and water (2:1:1), a 3D structure based in **stx** topology is obtained (Figure 1.7). This dramatic change

in the net of the MOF, can be explained as a consequence of thermodynamic stability and a stabilizing effect of the solvent[30].

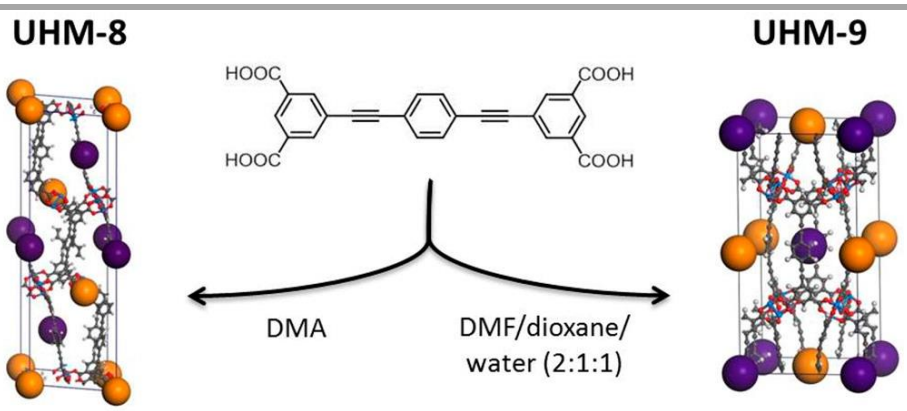

Figure 1.7. Scheme of reaction between the cooper(II) salt and the linear ligand giving as result two polymorphic MOFs, whose topology depends on if the solvent is DMA or the mixture DMF, dioxane, water (2:1:1). Adapted from Reference 30.

The solvent can affect the net topology but can be also used as a template to control the size and morphology of MOFs. This happens in a 3D MOF with the formula $[Zn_2(bdc)_2(dabco)]_n$, whose size and morphology can be controlled by the solvent mixture of DMF/MeOH. Depending on the volume ratio, if the solvent is only DMF nanoscale hexagonal rods are obtained, but when the ratio of MeOH increases gradually, so does the size of the hexagonal rods until a ratio of 50:50, in which the morphology starts to change from micrometric tetragonal plates to nanoscale tetragonal plates[31].

Figure 1.8. Scheme of reaction between zinc(II) and the ligands benzene-1,4-dicarboxylic acid (bdc) and 1,4-diazabicyclo[2.2.2]octane (dabco), in which a change in the volume ratio of solvent mixture DMF/MeOH has as result in a change in morphology and size of $[Zn_2(bdc)_2dabco]_n$ MOF. Adapted from Reference 31.

Other determinant factors in the obtention of coordination polymers are temperature and stoichiometry. The slightest change in one of these parameters can give as a result different structures or a change in their morphology or size. High temperature is usually necessary to obtain, directly from the reaction, crystals from coordination polymers suitable for SRXD and a simple change up or down in temperature can favor the process of making or breaking bonds, giving, as a result, one or another compound or a mixture of both. There are different studies like the example of a Zn(II)-MOF based in a benzobistriazolate (BBTA) ligand, whose solvothermal synthesis in DMF takes place at different temperatures from 140 to 60 °C for 24 h. The product obtained from 140 to 80 °C is always a 3D coordination polymer with the formula $[Zn_5Cl_4(BBTA)_3]\cdot 3$ DMF, but at 70 °C a

mixture of compounds is obtained and at 60 °C the second compound can be isolated. This second compound is a 2D coordination polymer with the formula $[ZnCl(BBTA)_{0.5}(DMF)]$, in which only four of the six nitrogen atoms of the benzobistriazolate ligand are coordinated and a DMF molecule is coordinated as ligand to the zinc(II) metal center (Figure 1.9)[32].

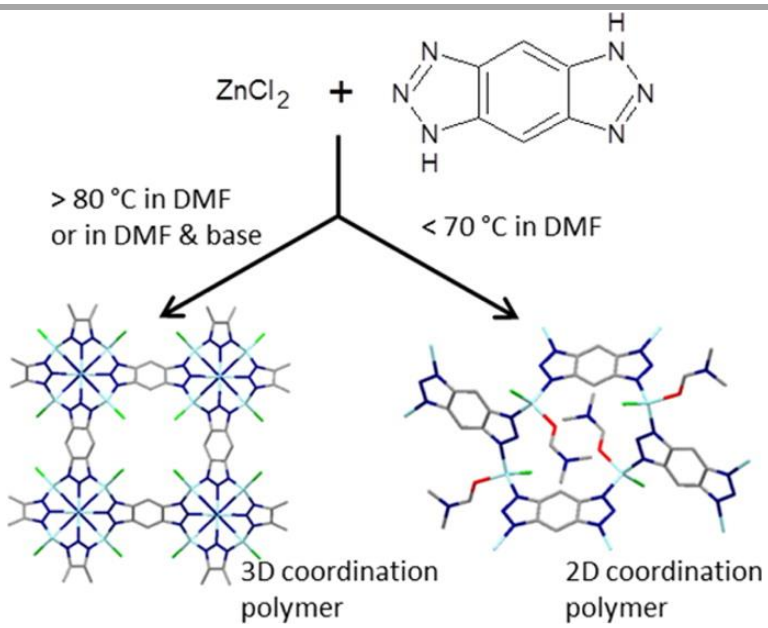

Figure 1.9. Scheme of reaction between Zn(II) and a benzobistriazolate ligand to obtain two different coordination polymers depends on the temperature of the reaction. Adapted from Reference 32.

Temperature controls the rate of the nucleation process and crystal growth, so it can sometimes favor the appearance of new species but in other cases it causes only a reorganization of the building blocks, resulting in a polymorph from the initial coordination polymer. This strategy was employed in two porous coordination polymers based

on a zinc(II) paddle-wheel cluster with dicarboxylate and diamine ligands with formula $[Zn_2(bdc)_2(dabco)]_n$ or $[Zn_2(bdc)_2(bpy)]_n$, (poner significado de acrónimos) whose obtention a 120 °C results in a tetragonal framework with square-grid motif (**sql**) but if the same building blocks are mixed at 25 °C a Kagomé motif (**kgm**) is obtained (Figure 1.10)[33].

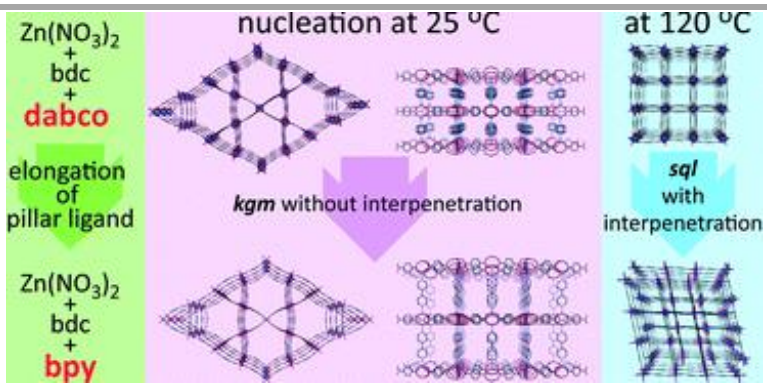

Figure 1.10. Scheme of reaction between Zn(II), benzenedicarboxylate (bdc), and diazabicyclo[2,2,2]octane (dabco) or 4,4'-bipyridine (bpy) at different temperatures to control the nucleation process and determine the framework topology. Adapted from Reference 33.

On other occasions, finding the desired coordination polymer lies in the variation of stoichiometry from reactant agents, so modifications of the metal/ligand ratio can produce slight variations such as the case of a family of 3D coordination polymers with Co(II) in which a considerable change in the molar ratio between metal salt and both ligands changes the topologies of the 3D networks[34]. However, the change is usually limited to one of the reagents and provides improvements in the yield or the properties of the product[35] or can result in a different and structure[36,37] (Figure 1.11).

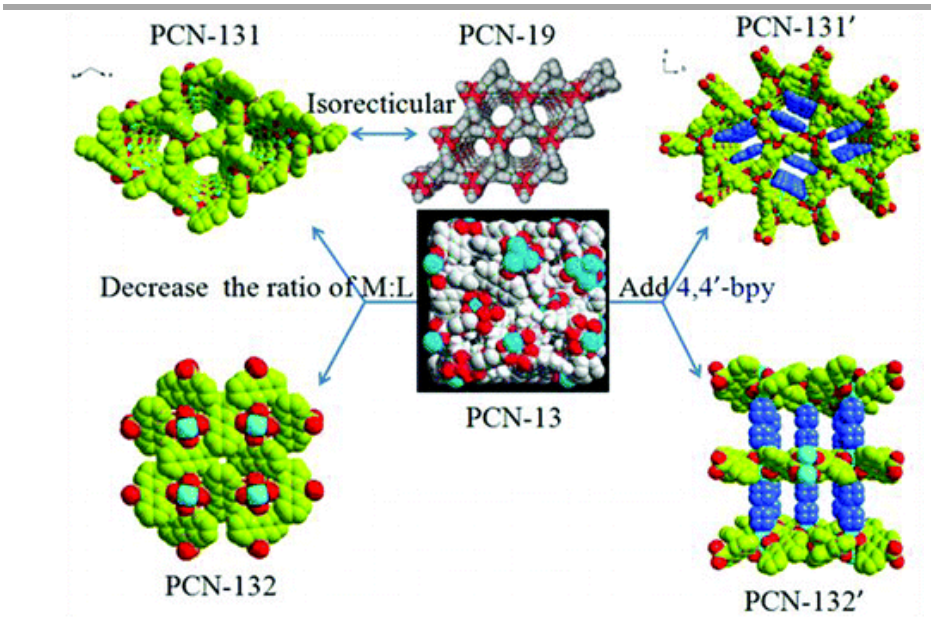

Figure 1.11. Scheme of synthesis through variation of molar ratio. Adapted from Reference 36.

Finally, the pH of the medium can direct the reaction to obtain the desired products. Usually, coordination polymers are neutral entities, but their starting building blocks can have basic or acidic groups that are affected by the pH of the reaction. In a similar way to the other reaction conditions, if a pH range is tested for the synthesis of a coordination polymer, different structures and topologies can be obtained (Figure 1.12)[38–41].

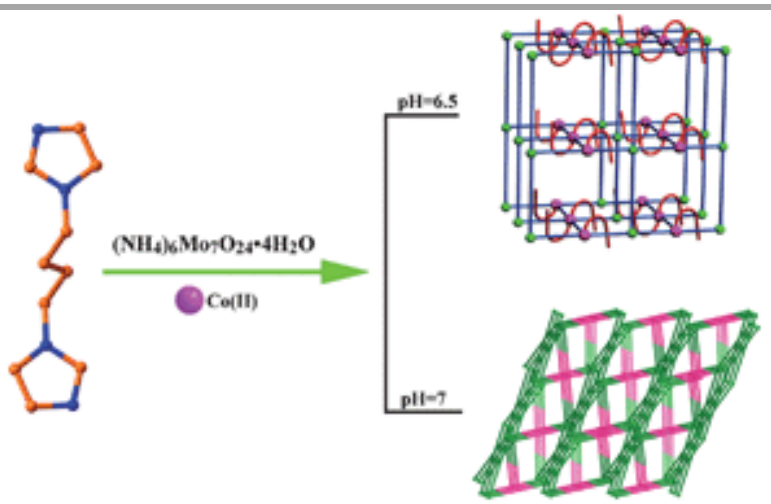

Figure 1.12. Scheme of synthesis of coordination polymer by changing pH. Adapted from Reference 39.

Sometimes to obtain the desired coordination polymer with the optimum properties it is necessary to change the reaction conditions several times or play with more than one factor.

1.3. Properties of Coordination Polymers

Properties and applications are the main goals in the design of new materials. In the case of coordination polymers that are tailorable materials, the building blocks play an important role in the search for properties[42]. Therefore, the building blocks are chosen with the future properties in mind, because metals or ligands can favor some properties over others[43–45]. Thus, the selection of the building blocks in coordination polymers can be focused on searching for a particular property or in combining more than one to obtain a multifunctional material[46,47].

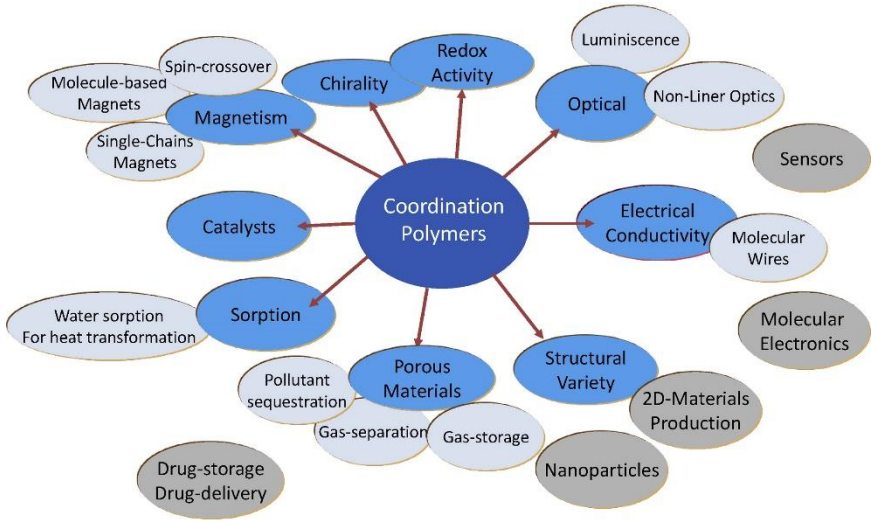

Figure 1.13. Scheme of the different properties (dark blue) and applications (clear blue) of coordination polymers. Adapted from Reference 42.

A coordination polymer can present an extensive number of properties such as electrical conductivity, magnetism, catalysis, porosity, molecular recognition, or luminescence, which can result in

a wide range of applications. Some of the principal properties of coordination polymers will be discussed below.

1.3.1. Electrical Conductivity

The ability to let electrical current pass through a material is measured by electrical conductivity and depends on the structure and the components of the material. The diversity of the two main building units and the wide variety of structures allows coordination polymers to perform as ionic or electronic conductive materials. Usually, coordination polymers are insulators, or their electronic/ionic conductivity is very low because the combination between hard metal ions and redox-inactive organic ligands that bind via oxygen or nitrogen donor atoms does not provide effective pathways for charge transport[48]. However, recent developments in coordination polymers based on conductive materials have showed the superior properties of these materials[10,49]. Two different approaches can be considered to provide electrical conductivity in coordination polymers, using the pores in MOF or CP structures or directly modifying the pristine compound.

- ***Ionic Conductivity***

In the case of porous coordination polymers, it is more often the ionic conductivity that is exploited, since mobile ions such as protons, metal ions, or ionic liquids can be trapped in their cavities. Proton conductivity can be found in humid or anhydrous conditions, being more common in the examples mediated by water. The properties in

a humid environment can be adjusted by modulating the framework structure like the 3D-MOF known as **KAUST-7**, which suffers a structural phase change at 90 °C and 95 % relative humidity (RH) into a novel 2D-MOF named **KAUST-7'**. The new phase shows a protonic conductivity up to $2.0 \cdot 10^{-2}$ $S \cdot cm^{-1}$ and its structure is maintained over one week of experiments (Figure 1.14)[50].

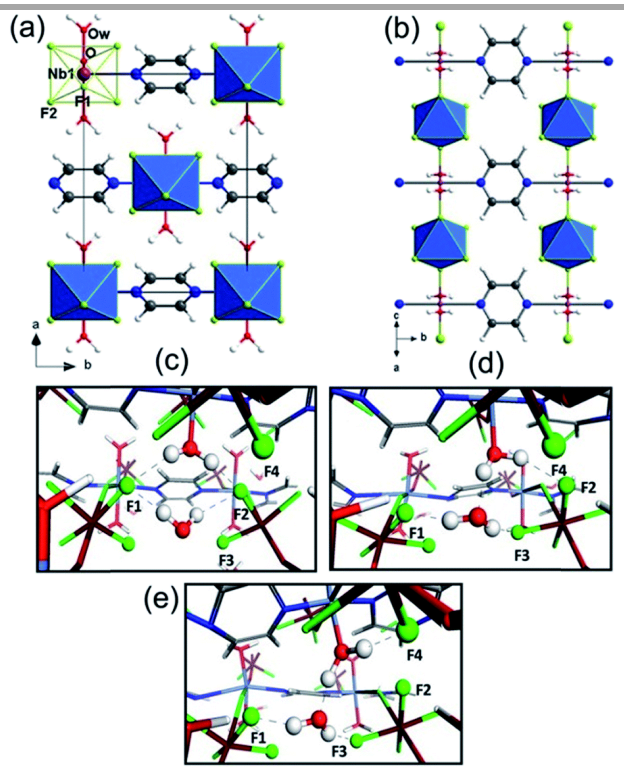

Figure 1.14. Crystal structure of KAUST-7' along the a) [001] and b) [101] directions. Reorganization of the hydrogen-bond network along the [101] direction after a) 0.009 ps, b) 1.072, and c) 1.879 ps of the molecular dynamic calculations run. The atoms are represented as: F, green; C, gray; O, red; N, blue; Ni, Nb, brown, and H, white. Adapted from Reference 50.

Proton conductivity properties can be also tuned by guest molecules such as the example of the polyoxometalate-based MOF ($[Cu_{12}(BTC)_8(H_2O)_{12}]$ $[HPW_{12}O_{40}]$)·guest (**NENU-3**), in which the incorporation of free imidazole groups as guest molecules (**Im-Cu@(NENU-3**) or as molecules coordinated in the framework occupying the space available in the cages (**Im-Cu@(NENU-3a**) (Figure 1.15a-b) means a change in the proton conductivity from $1.82 \cdot 10^{-2}$ S·cm^{-1} to $3.16 \cdot 10^{-4}$ S·cm^{-1} at 90% RH and 70 °C, respectively (Figure 1.15c-d)[51]. The imidazole molecules bound to the framework are immobilized and isolate the lattice water molecules blocking the proton transport pathway.

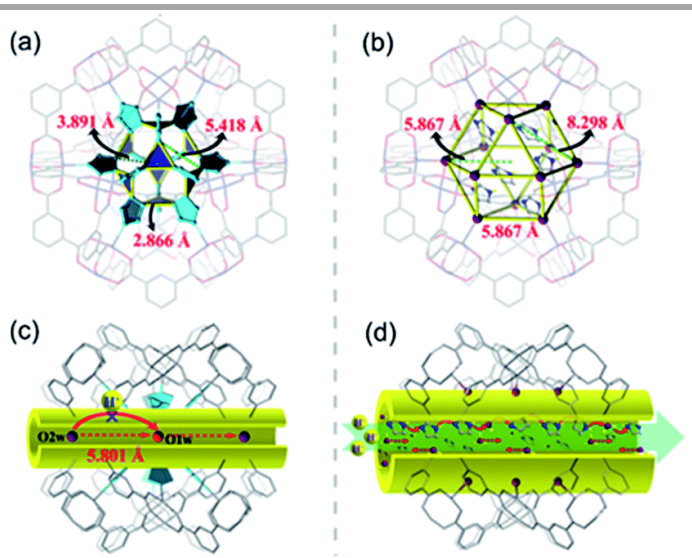

Figure 1.15. The cubooctahedral cage in a) Im-Cu@(NENU-3a) after its exposure to water vapor atmosphere (at 70 °C and 90% RH) and b) original NENU-3 which shows the different pore spaces and window size that allow more free imidazole molecules inside the pore. c) Possible pathway of the proton conduction for Im-Cu@(NENU-3a) based on the SCXR analysis. d) Schematic diagram of the probable proton transport pathways for Im-Cu@(NENU-3). Adapted from Reference 51.

Finally, the proton conductivity under humid conditions can be improved by the functional groups of the organic linkers. These groups can be positioned on the surface of the channels, making them more hydrophilic and encouraging the proton transport pathways under humid conditions. One example of this fact is the flexible 3D-MOF **BUT-8(Cr)** which possesses 1D channels lined with high-density sulfonic acid (-SO_3H) on their surface for proton conduction. When **BUT-8(Cr)** is exchanged with H_2SO_4 to replace the $NH_2(CH_3)_2^+$ counter ions, **BUT-8(Cr)A** is obtained as a result (Figure 1.16 a-d). The proton conductivity was studied in both structures and at 100% RH and 80 °C high values of $4.63 \cdot 10^{-2}$ and $1.27 \cdot 10^{-1}$ $S \cdot cm^{-1}$ were acquired, respectively. The flexible and chemically stable structure enables to self-adapt of the framework under variable humidity conditions, ensuring steady proton conduction pathways (Figure 1.16 e-f)[52].

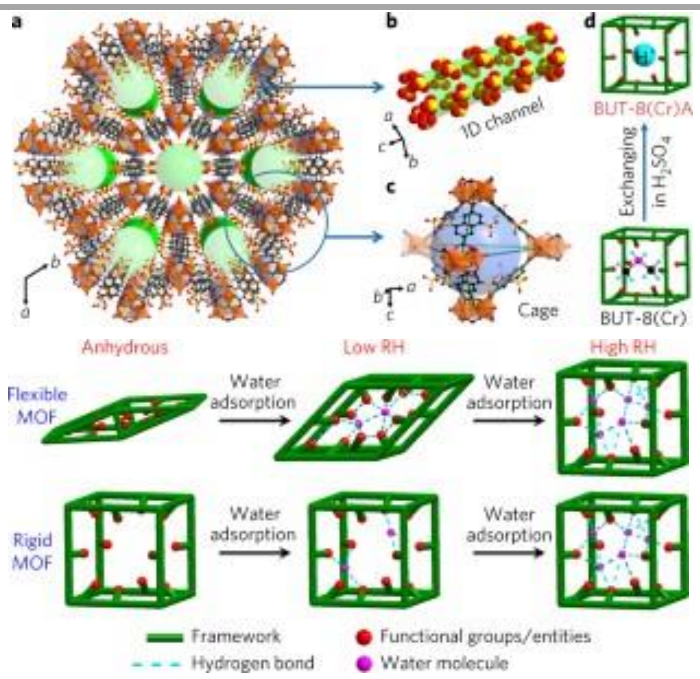

Figure 1.16. a) Crystal structure of BUT-8(Cr) along the *c* direction. Ampliation of b) the 1D porous channel functionalized by sulfonate groups and d) the polyhedral cage unit. d) Scheme of the ion exchange in BUT-8(Cr) to form BUT-8(Cr)A. Schematic illustration of water adsorption in e) a flexible and f) a rigid MOF. Adapted from Reference 52.

The anhydrous proton conductivity can be found in hybrid materials in which the coordination polymer is uniformly covered of proton carriers in an organized manner, so the composite shows proton conductivity at temperatures above 80 °C. These materials are useful in applications that require high conductivity at high temperatures, like fuel-cell hydrogen conversion technology which operates at temperatures up to 120 °C. For example, if the MOF MIL-101 is impregnated with H_2SO_4 or H_3PO_4, they exhibit an anhydrous proton conduction with values around to $1 \cdot 10^{-2}$ $S \cdot cm^{-1}$ for **H_2SO_4@MIL** and

$3 \cdot 10^{-3}$ S·cm^{-1} for **H_3PO_4@MIL** when they are heated at 150 °C and low humidity[53].

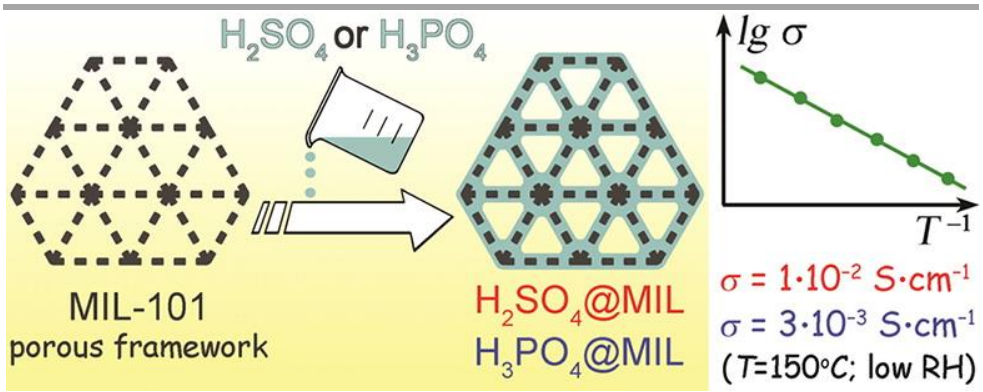

Figure 1.17. Schematic representation of the impregnation process of MIL-101 and the temperature dependance of the conductivity of the hybrid materials **H_2SO_4@MIL** and **H_3PO_4@MIL**. Adapted from Reference 53.

However, the brittleness of MOF materials prevents to use them directly for applications in fuel cells, and, as an alternative to solve this problem, MOF hybrid materials with high proton conductivity can be introduced into polymer membranes[54].

Ionic conductivity of metal ions is an outstanding field, particularly on Li^+ conduction. The principal purpose is commercial lithium batteries, which are based on the movement of lithium ions between the anode and the cathode. Although they are essential in many areas today, these batteries have many disadvantages such as volatility or flammability, so it is necessary to explore new solid electrolyte materials that can replace liquid systems. Thus, coordination polymers are good candidates for metal ion conduction because of their rationally design structures and their capability to suffer post-

synthetic modifications. There is a recent work inspired by the ionic channels found in biological systems that uses a well-known MOF like **HKUST-1** as a matrix. **HKUST-1** possesses 3D channels with coordinated molecules inside, so generating pores with open metal sites is indispensable. Once the coordinated molecules have left the pores, $LiClO_4$ is inserted into the framework allowing ClO_4^- ions to coordinate to the open metal sites and forming the anionic framework **LPC@HKUST-1**. Therefore, the framework is negatively charged and is able to transfer Li^+ ions with an ion conductivity of $3.8 \cdot 10^{-4}$ $S \cdot cm^{-1}$ and low activation energies (< 0.21 eV)[55].

The transport of Li^+ cations is the main focus in metal ion conductivity, but the transport of alkaline earth metal ions like Mg^{2+} also has been explored. However, these ions have higher charge density and larger sizes, so the mobility through the channels is difficult and obtaining materials with good values of conductivity is laborious[56,57].

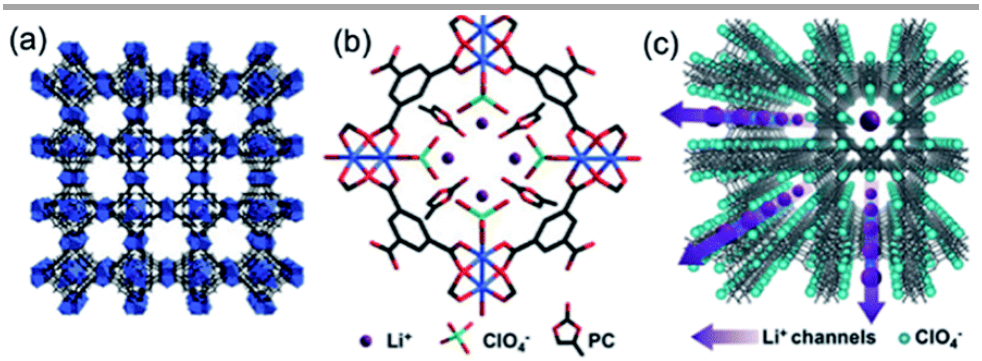

Figure 1.18. a) 3D network of HKUST-1 in which the copper nodes are blue and the BTC ligands are black. b) Ampliation of the ionic channels in HKUST-1 with ClO_4^- anions coordinate to the open metal sites and solvated Li^+ ions inside the channels (Cu, blue; C, black; O, red). c) Schematic representation of biomimetic ionic channels in HKUST-1 (dark gray) with ClO_4^- ions (cyan dots) and solvated Li^+ ions (purple dots). Adapted from Reference 57.

The use of ionic liquids (ILs) combined with coordination polymers to generate new hybrid materials is still recent. These composite materials enable to operate under extreme conditions like low temperature and in a safe way. Therefore, the combination between ILs and coordination polymers is attractive for their application in electrochemical devices such as solid electrolytes for fuel cells or secondary batteries[58]. One of the contributions in this area studies the ionic conductivity in the popular **ZIF-8** after loading it with two different ILs. The experimental results show that the hybrid material possesses higher ionic conductivity than only the ILs at low temperature, because the IL is efficiently trapped inside the MOF structure[59].

- ***Electronic Conductivity***

On the other hand, electronic conductivity is commonly found in non-porous coordination polymers. This type of conductivity is useful for its application in electrochemical energy storage and conversion, so the design and synthesis of new materials with electrical conductivity has attracted increasing attention. Despite the wide variety of combinations between metal ions and ligands, the values of electrical conductivity obtained hitherto in coordination polymers are still not good enough for the applications mentioned above, although there are various approaches that have improved the values of these materials and their use in technological applications becomes closest every time. One of the approaches is the use of halogens as ligands in the coordination polymers to form 1D chains with M-X (where M is the metal ion and X the halogen) as the main motif. There are numerous works proving the fact that when the halogen atoms bridge heterobimetallic units the delocalization of the inter-dimer electrons is favored, and it is reflected in an improvement in conductivity[60–62]. A recent work shows two 1D coordination polymers with Cu(I)-I chains, with semiconductor behaviors, whose best value at room temperature is $3 \cdot 10^{-3}$ $S \cdot cm^{-1}$. This work shows the relevance of the Cu-I skeleton in the electrical conductivity when a slight change in the main ligand provokes a decrease in the electrical conductivity as demonstrated by the theoretical calculations (Figure 1.19)[63].

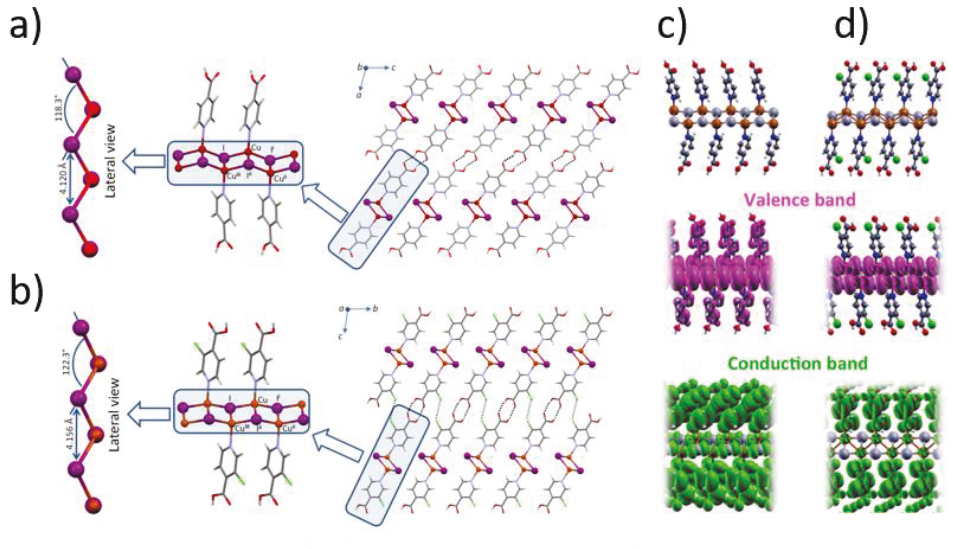

Figure 1.19. Crystal structure of 1D coordination polymers a) $[Cu(HIN)I]_n$ and b) $[Cu(Cl\text{-}HIN)I]_n$ showing the differences between distances and angles depending on the ligand. Computed 3D orbital of the VBs and CBs for c) $[Cu(HIN)I]_n$ and d) $[Cu(Cl\text{-}HIN)I]_n$. Adapted from reference 63.

However, the organic linkers can also play an essential role in electronic conductivity as charge carriers. Their structure with electron-donating or electron-withdrawing moieties can be used to modulate the density and distribution of the charge along the continuous network formed with the metal nodes. For example, it is common the use of multidentate ligands rich in π-π interactions bonded to metal ions with square planar geometry to yield 2D coordination polymers[64–66], among which stands out the high value of electrical conductivity of 1580 $S \cdot cm^{-1}$ at room temperature obtained by the 2D coordination polymer formed by Cu(II) and benzenehexathiol (BHT)[67].

Sometimes the insulating behavior obtained in a coordination polymer can be improved by doping the material with redox-active molecules like pyrrole or TCNQ, which are introduced as guest molecules. Although it is difficult to tune a poor conductivity, some examples have shown the change in the conductivity value between the original and the doped coordination polymer[66,68,69].

1.3.2. Magnetism

Searching for coordination polymers with magnetic properties is a great aim within materials chemistry. The advantage of coordination polymers over other materials is the ability to select the ideal combination of metal ions and linkers. Usually, the metal ions are the spin carriers, but organic ligands can also fulfill that role. The linkers employed in coordination chemistry are normally too long and are inadequate to transmit magnetic information, although they can be replaced by short bridging ligands that achieve a strong coupling or radicalic organic ligands can be used directly as spin carriers. In addition, the coordination bonds established between metal centers and bridging ligands are more effective to communicate magnetic information than intermolecular interactions through space.

One of the more studied magnetic phenomena is the spin-crossover (SCO), based on the competition between the spin paring energy and the energy gap of the orbitals e_g and t_{2g} of transition metal ions with an octahedral environment (Figure1.20). Spin-crossover is the ability to switch between low-spin (LS, when the energy gap is greater than spin pairing energy and d-electrons remain paired filling the lowest

energy orbitals) and high-spin (HS, when the spin pairing energy is greater than energy gap and d-electrons can unpaired filling both orbitals) by an external stimulus such as temperature, pressure, light irradiation, magnetic field, or guest sorption.

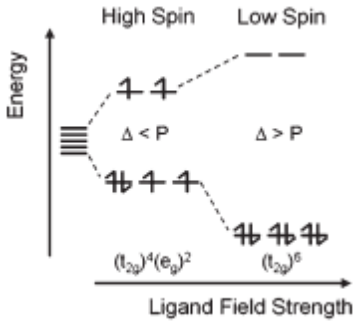

Figure 1.20. Scheme representation of an octahedral crystal field splitting diagram showing the high-spin and low-spin states for Fe^{2+}.

On the other hand, the development of molecular magnetism has advanced from studying the magnetic properties of molecule-based compounds in the eighties[70] to designing new materials and devices based on these molecular materials[71]. The examples in coordination polymers are varied, 1D coordination polymers have shown their value as single-chain magnets (SCM), in which the intermolecular magnetic interactions between chains are weaker than the dominant intra-chain spin coupling along the infinite chain[72]. Single-chain magnets are characterized by slow magnetic relaxation times at a finite temperature, and they can be effective as magnetic nanowires for data storage. Although the SCM behavior is not easy to obtain, from 2001, when the first 1D coordination polymer with SCM behavior[73] was described with Co(II) as metal center, other studies

have followed it until their obtention as multifunctional materials[74–77].

However, recent advances in the field of molecular materials have been focused on 3D and 2D coordination polymers, which have shown their potential application in the emerging areas of molecular spintronics and quantum computing. For example, monolayers of 2D coordination polymers with transition metal ions regularly distributed can exhibit exotic magnetic order and remarkably higher Curie temperatures (T_c)[78]. In the case of 3D coordination polymers, the presence of pores in the structure has increased the attention to these materials in the magnetism field[79]. Therefore, three different possibilities can be distinguished in MOFs, a magnetic MOF with a magnetic framework regardless of the guest molecule, a non-magnetic MOF with functional molecules as guests, or a MOF with the magnetic framework and also a functional guest (Figure 1.21). Designing a porous structure with magnetic properties conveys a certain complexity because longer linkers favor larger pores, but shorter linkers are the best option for magnetic properties. However, it has been possible to obtain porous materials starting from short linkers like carboxylate, imidazolate or cyanide ligands that show magnetic ordering and BET surface areas of 360 or 480 $m^2 \cdot g^{-1}$. [80,81]

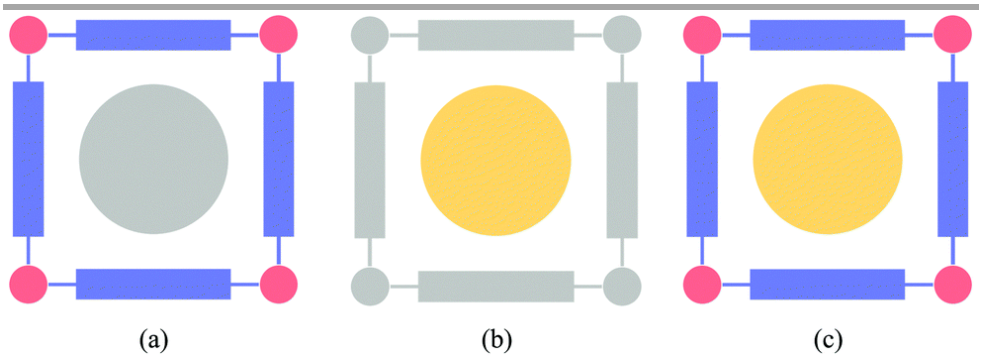

Figure 1.21. Scheme of a) MOF with a magnetic framework and non-functional guest, b) MOF without a magnetic framework, but a functional guest, and c) MOF with a magnetic framework and functional guest. Adapted from Reference 80.

These compounds have a dense metallic packing with certain porosity, but the porosity can be improved by combining short and long bridging ligands. This method enables to obtain MOFs with BET surface areas over 1000 $m^2 \cdot g^{-1}$, although it limits the magnetic order to low temperatures[82]. Other approaches to achieve magnetic frameworks are the use of radicalic ligands that favor the coupling between the metal centers[83] or the use of a metal complex as a building block, also known as the metallo-ligand approach[84]. However, these two methods have disadvantages too, the compounds obtained using radicalic ligands make the exchange coupling between metal ions easier, but they are not too stable; and even though the metallo-ligands approach seems a good option, searching for the ideal combination limits the options to prepare magnetic MOFs.

On the other hand, MOFs based on the phenomenon of spin-crossover do not need a detailed design of the framework, only first row transition metals and an environment which favors the switching

between HS and LS states are required. Therefore, either the length of the bridging ligands or the connectivity between metal nodes are not a restriction since the polymeric nature of the framework contributes to connecting the spin-crossover centers ignoring the distance. In the cases of these MOFs, the guest molecule can play a key role in the spin-crossover properties, for example depending on the number of molecules occupying the voices, the type of guest molecule, or what kind of adsorption happen[85–87].

Finally, MOFs can combine a magnetic network and a functional guest, resulting in a hybrid material with multifunctional properties. They can be obtained directly from the synthesis or by post-synthetic methods, in which the guest molecule is introduced. These types of materials can contain guests complexes exhibiting spin-crossover or single-molecule magnet behavior, resulting in magnetic structures with potential electronic applications (Figure 1.23)[88–91].

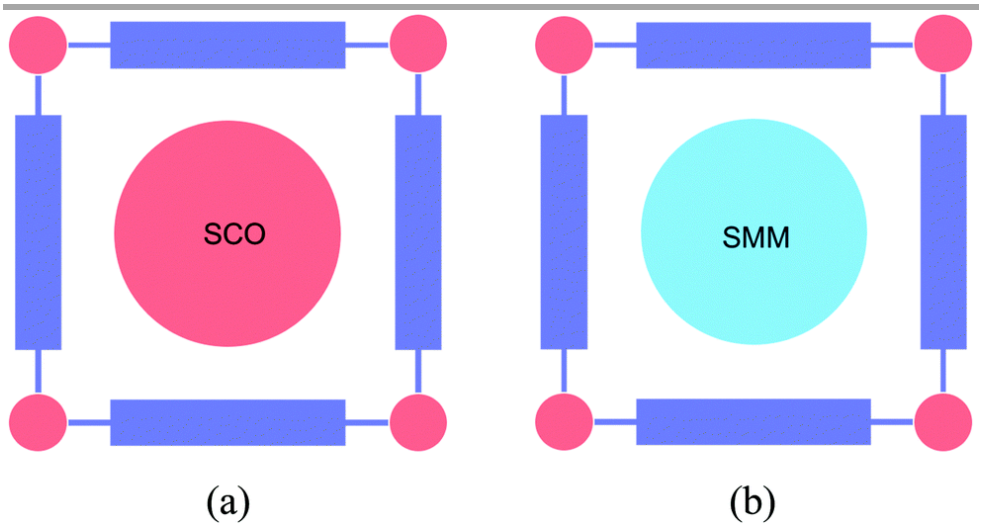

Figure 1.23. Schematic representation of MOFs frameworks incorporating as a magnetic guest a) spin-crossover complex and b) single-molecule magnets. Adapted from Reference 80.

1.3.3. Luminescence

Luminescence is a phenomenon of emission of radiation from an excited state and can be generated by different sources such as photonic excitation, mechanical forces, or chemical/electrochemical reactions. The mechanism related with this process involves transitions of electrons from the ground state to an excited state by the absorption of a photon followed by the return to the ground state with emission of a photon through relaxation processes, which can be radiative or nonradiative (Figure 1.24). There are two categories of luminescence, depending on the nature of the excited state, it can be distinguished between fluorescence and phosphorescence. In the case of fluorescence, the transition occurs from the singlet excited

state (S_1) to the singlet ground electronic state (S_0), resulting in an excited state with short lifetime between 1-100 ns. On the other hand, the phosphorescence occurs more slowly because first, an intersystem crossing (ISC) occurs from the singlet excited state (S_1) to the triplet excited state (T_1), followed by a forbidden photon-emitting transition to the singlet ground electronic state (S_0), resulting in an excited state with a long lifetime of 1 µs or longer.

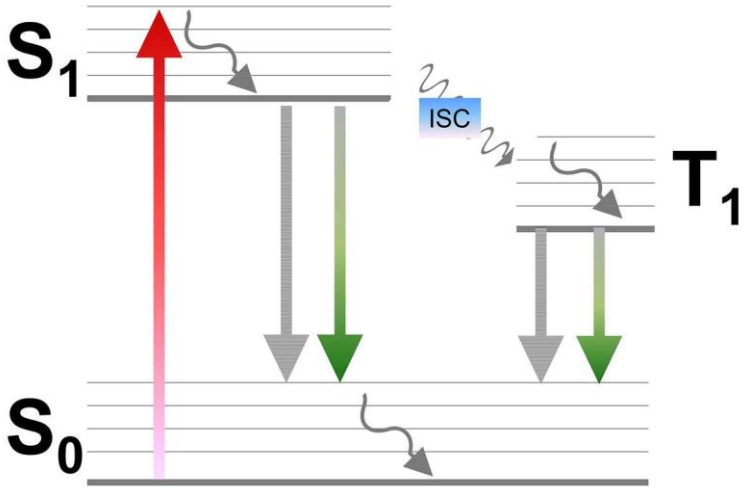

Figure 1.24. Simplified representation of Jablonski diagram with the processes of molecular excitation/emission. Adapted from Reference 93.

The wide variety of metal ions and ligands as well as the different topologies that can be adopted by the coordination polymers make the mechanism of luminescence richer. Coordination polymers can present metal-centered (MC) emission based on d-d or f-f transitions from the metal ions, ligand-centered (LC) emission based on π-π^* transitions from the organic ligands and different charge transfer emissions such as metal-to-metal charge transfer (MMCT), metal-to-

ligand charge transfer (MLCT), ligand-to-metal charge transfer (LMCT) and ligand-to-ligand charge transfer (LLCT). In addition, this mechanism of emission can be affected by the guest molecule in porous coordination polymers. The metal nodes commonly used for luminescent properties are rare-earth metal ions, which possess long luminescence lifetimes and are able to give a wide range of coordination polymers, being the most typical the coordination polymers with europium, terbium and gadolinium[92–94]. These lanthanoid ions have larger energy gaps and are notably more emissive, Eu and Tb emit in the visible range while Gd in the UV range. Although numerous studies have been made about 4f metals, the d^{10} transition metal ions such as Zn(II), Cd(II), Cu(I) or Ag(I) have also attracted the attention for coordination compounds with luminescent properties[95–98].

There are different applications for luminescent coordination polymers, being one of the more characteristic ones their use as sensors because of their selectivity, sensitivity, and rapid response. They can be used as sensors for volatile organic molecules (VOC) taking advantage of porous structures[99] or sensors for detecting explosive materials[100], but they are best-known as biosensors or fluorescent probes. There is a recent example that shows Tb-based coordination polymer microspheres with the ability to detect traces of the anthrax biomarker (dipicolinate acid or DPA) showing fluorescence response (Figure 1.25)[101].

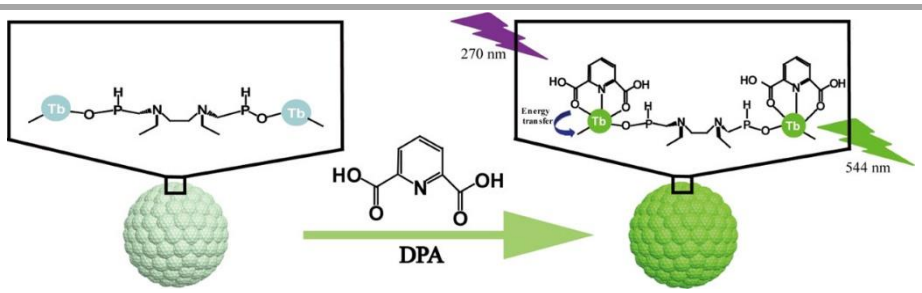

Figure 1.25. Schematic representation of Tb coordination polymers microspheres acting as fluorescent probes when detect the biomarker DPA. Adapted from Reference 76.

1.4. Nanoscale Coordination Polymers

Coordination Polymers are well-studied materials, whose wide variety of combinations between metal ions and organic and inorganic ligands achieves different network constructions (1D, 2D, or 3D). In addition, the chemical and physical properties are also diverse and can be integrated into multifunctional materials. Thus, it is not surprising that their quick development in leading fields like medicine or technology has concluded in an adjustment of the materials to the necessities. An essential requirement is the decrease of the size of the materials to the nanometer scale, in which at least one dimension has to be below 100 nm. There are two different approaches to synthesize nanomaterials: bottom-up and top-down. The first approach is based on the organization of atoms or molecules to start to build-up nanostructures through self-assembly. On the other hand, the top-down method is based on the miniaturization of bulk materials until the obtention of a product with the desired size and shape[102,103].

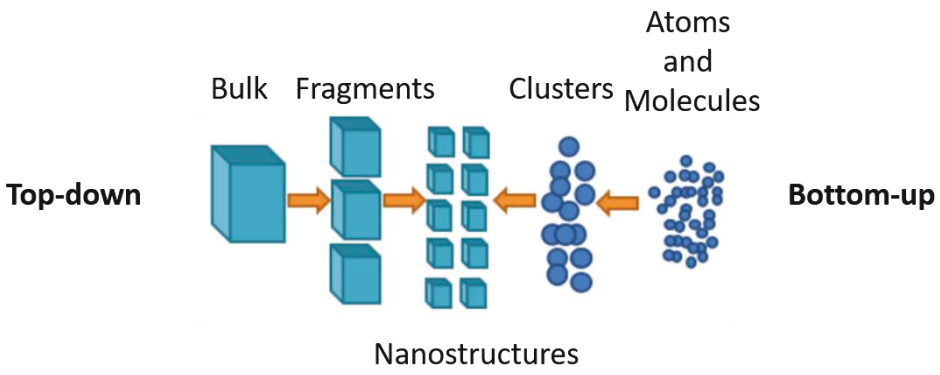

Figure 1.26. Schematic representation of approaches top-down and bottom-up. Adapted from Reference 102.

In the case of coordination polymers it is more common for the obtention of nanoscale materials to use bottom-up approach since their synthesis is by self-assembly of building blocks in a one-pot reaction and as it was shown before the key role of the reaction conditions may be also crucial to modify the size[104]. Although it is less common, the use of the top-down approach is possible due to the insolubility of coordination polymers once they are obtained; exfoliation methods of the bulk compound are employed to decrease the size usually in liquid phase[105].

When the size of materials is reduced, the surface exposed increases compared to the bulk material, being the clearest example in nanoparticles[106]. Therefore, the properties shown by bulk materials may change when the material is nanoprocessed, resulting in a new and interesting size-dependence of physical and chemical properties[107]. Although coordination polymers are not an exception of this dependence between size and properties, these changes in

properties are not dramatic when the size is modified. However, nanoscale coordination polymers have attracted more attention in recent years because they are capable of adding their different physical and chemical properties to other materials like polymeric matrixes to yield hybrid materials with improved properties. This connection between size and properties will be discussed below.

Biological and medical applications are one of the principal niches for nanoscale coordination polymers. Their structural design, their stability, and their tailored size make these materials good candidates in these fields. Their principal uses are as carriers for drug delivery or as theragnostic agents (the combination between therapy and diagnostic) since nanoparticle-based coordination polymers or the porous structures have high loading capacity and exhibit control over release upon slight modifications. For example, a nanoscale coordination polymer of Mn(II) with mesoporous structures is capable of loading the chemotherapeutic doxorubicin (DOX) and releasing the drug after self-dissociating by redox-response (Figure 1.27)[108].

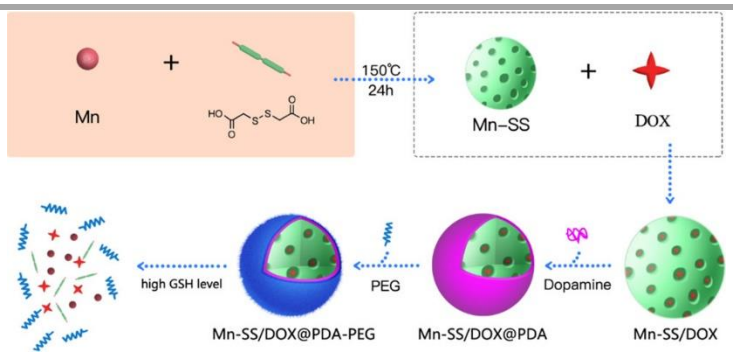

Figure 1.27. Scheme of synthesis of nanoscale coordination polymer and the processes of loading, coating, and releasing of DOX drug. Adapted from Reference 108.

Other characteristic applications of nanoscale coordination polymers are as imaging agents and biosensors. Luminescent properties are common in the case of biosensors, being a typical approach to the enhancement, quenching, or shifting of fluorescence signals when the target appears[109]. In the case of imaging agents, nanoscale coordination polymers are used to show the presence of certain molecules, proteins, receptors, or cell types and they can act as optical or contrast agents[110,111].

The other field in which the use of nanoscale coordination polymers shines is nanotechnology. Obtaining the smallest devices is the objective nowadays, so finding components with nanometric sizes and interesting properties is a milestone. The advantages that nanoscale coordination polymers can provide are the cheap prices of starting reactants, the simplicity of being obtained in one-pot reactions, and the combination of multiple properties. In the case of electrical conductivity, there are some improvements of three to four orders of magnitude between bulk materials and nanoscale 1D coordination polymers[112], although recent research showed that structural defects prevent the obtention of better values[113]. However, the conductivity of 2D coordination polymers with planar structures analogous to 2D materials like graphene maintains their good conductivity values at the nanoscale and they are promising candidates as transparent electrodes for photovoltaic solar cells[114]. Although the high cost of some organic materials prevents their use at a large scale, so new hybrid materials of nanoscale coordination

polymers of Cu(I) can be appreciated as reasonable competitors with interesting optoelectronic propeties[115].

The other property that shows a change in its values when the size is decreased is magnetism. Nanoscale coordination polymers with magnetic properties are interesting incorporation in quantum computing architectures. Molecular qubits or quantum bits show all the requirements to be used as hardware in quantum processors, but they need to be implemented into hybrid-solid state devices and a good alternative is to use this molecular cubit as nodes in nanoscale coordination polymers to ensure their homogeneous orientation and control over the localization[116].

1.5. Objectives

This trip along the history of coordination polymers shows that starting from simple building blocks like metal ions and organic or inorganic linkers a wide range of structures can be obtained, which may be useful in different fields depending on their properties. However, the quick development in medical and technological areas suggests that there is still a long way to go.

Thus, this thesis tries to deepen the design of new coordination polymers using Cu(II) as the metal center and well-known biomolecules as nucleobases as ligands. Their synthesis and characterization will be discus as well as their reduction in size until the nanoscale. Once the full characterization is completed, different factors will be considered such as stability, structure, or processability to the potential applications of each material.

1.6. References

(1) West, F. The Detection of Prussian Blue in Tea. *J. Ind. Eng. Chem.* **1912**, *4* (7), 528–528.

(2) Perutz, M. F. Hemoglobin Structure and Respiratory Transport. *Sci. Am.* **1978**, *239* (6), 92–125.

(3) Constable, E. C.; Housecroft, C. E. Coordination Chemistry: The Scientific Legacy of Alfred Werner. *Chem. Soc. Rev.* **2013**, *42* (4), 1429–1439.

(4) Hoskins, B. F.; Robson, R. Infinite Polymeric Frameworks Consisting of Three Dimensionally Linked Rod-like Segments. *J. Am. Chem. Soc.* **1989**, *111* (15), 5962–5964.

(5) Hoskins, B. F.; Robson, R. Design and Construction of a New Class of Scaffolding-like Materials Comprising Infinite Polymeric Frameworks of 3D-Linked Molecular Rods. A Reappraisal of the Zinc Cyanide and Cadmium Cyanide Structures and the Synthesis and Structure of the Diamond-Rela. *J. Am. Chem. Soc.* **1990**, *112* (4), 1546–1554.

(6) Eddaoudi, M.; Moler, D. B.; Li, H.; Chen, B.; Reineke, T. M.; O'Keeffe, M.; Yaghi, O. M. Modular Chemistry: Secondary Building Units as a Basis for the Design of Highly Porous and Robust Metal−Organic Carboxylate Frameworks. *Acc. Chem. Res.* **2001**, *34* (4), 319–330.

(7) Kitagawa, S.; Kitaura, R.; Noro, S. Functional Porous Coordination Polymers. *Angew. Chemie Int. Ed.* **2004**, *43* (18), 2334–2375.

(8) Haldar, R.; Matsuda, R.; Kitagawa, S.; George, S. J.; Maji, T. K. Amine-Responsive Adaptable Nanospaces: Fluorescent Porous Coordination Polymer for Molecular Recognition. *Angew. Chemie Int. Ed.* **2014**, *53* (44), 11772–11777.

(9) Näther, C.; Wöhlert, S.; Boeckmann, J.; Wriedt, M.; Jeß, I. A Rational Route to Coordination Polymers with Condensed Networks and Cooperative Magnetic Properties. *Zeitschrift für Anorg. und Allg. Chemie* **2013**, *639* (15), 2696–2714.

(10) Givaja, G.; Amo-Ochoa, P.; Gómez-García, C. J.; Zamora, F. Electrical Conductive Coordination Polymers. *Chem. Soc. Rev.* **2012**, *41* (1), 115–147..

(11) Heine, J.; Müller-Buschbaum, K. Engineering Metal-Based Luminescence in Coordination Polymers and Metal–Organic Frameworks. *Chem. Soc. Rev.* **2013**, *42* (24), 9232.

(12) Janiak, C. Engineering Coordination Polymers towards Applications. *J. Chem. Soc.*

Dalt. Trans. **2003**, *3* (14), 2781–2804.

(13) Abrahams, B. F.; Dharma, A. D.; Donnelly, P. S.; Hudson, T. A.; Kepert, C. J.; Robson, R.; Southon, P. D.; White, K. F. Tunable Porous Coordination Polymers for the Capture, Recovery and Storage of Inhalation Anesthetics. *Chem. - A Eur. J.* **2017**, *23* (33), 7871–7875.

(14) Doonan, C. J.; Sumby, C. J. Metal–Organic Framework Catalysis. *CrystEngComm* **2017**, *19* (29), 4044–4048.

(15) Zhu, W.; Zhao, J.; Chen, Q.; Liu, Z. Nanoscale Metal-Organic Frameworks and Coordination Polymers as Theranostic Platforms for Cancer Treatment. *Coord. Chem. Rev.* **2019**, *398*, 113009.

(16) Dey, S.; Sil, S.; Dutta, B.; Naskar, K.; Maity, S.; Ray, P. P.; Sinha, C. Designing of Pb(II)-Based Novel Coordination Polymers (CPs): Structural Elucidation and Optoelectronic Application. *ACS Omega* **2019**, *4* (22), 19959–19968.

(17) Halevi, O.; Chen, J.; Thangavel, G.; Morris, S. A.; Ben Uliel, T.; Tischler, Y. R.; Lee, P. S.; Magdassi, S. Synthesis through 3D Printing: Formation of 3D Coordination Polymers. *RSC Adv.* **2020**, *10* (25), 14812–14817.

(18) Furukawa, H.; Cordova, K. E.; O'Keeffe, M.; Yaghi, O. M. The Chemistry and Applications of Metal-Organic Frameworks. *Science (80-.).* **2013**, *341* (6149), 1230444.

(19) Konnerth, H.; Matsagar, B. M.; Chen, S. S.; Prechtl, M. H. G.; Shieh, F.-K.; Wu, K. C. W. Metal-Organic Framework (MOF)-Derived Catalysts for Fine Chemical Production. *Coord. Chem. Rev.* **2020**, *416* (1), 213319.

(20) Batten, S. R.; Champness, N. R. Coordination Polymers and Metal–Organic Frameworks: Materials by Design. *Philos. Trans. R. Soc. A Math. Phys. Eng. Sci.* **2017**, *375* (2084), 20160032.

(21) Desiraju, G. R. *Crystal Design: Structure and Function*; Desiraju, G. R., Ed.; Perspectives in Supramolecular Chemistry; John Wiley & Sons, Ltd: Chichester, UK, 2003.

(22) Desiraju, G. R.; Gavezzotti, A. From Molecular to Crystal Structure; Polynuclear Aromatic Hydrocarbons. *J. Chem. Soc. Chem. Commun.* **1989**, *53* (10), 621.

(23) Desiraju, G. R. The Supramolecular Synthon in Crystal Engineering. In *Stimulating Concepts in Chemistry*; Wiley-VCH Verlag GmbH & Co. KGaA: Weinheim, FRG, 2005; pp 293–306.

(24) Yaghi, O. M.; O'Keeffe, M.; Ockwig, N. W.; Chae, H. K.; Eddaoudi, M.; Kim, J.

Reticular Synthesis and the Design of New Materials. *Nature* **2003**, *423* (6941), 705–714.

(25) Kalmutzki, M. J.; Hanikel, N.; Yaghi, O. M. Secondary Building Units as the Turning Point in the Development of the Reticular Chemistry of MOFs. *Sci. Adv.* **2018**, *4* (10), 9180.

(26) Stuart R Batten, Suzanne M Neville, D. R. T. *Coordination Polymers*; Royal Society of Chemistry: Cambridge, 2008.

(27) Engel, E. R.; Scott, J. L. Advances in the Green Chemistry of Coordination Polymer Materials. *Green Chem.* **2020**, *22* (12), 3693–3715.

(28) Wan, X.; Jiang, F.; Chen, L.; Wu, M.; Zhang, M.; Pan, J.; Su, K.; Yang, Y.; Hong, M. Structural Diversity Modulated by the Ratios of a Ternary Solvent Mixture: Syntheses, Structures, and Luminescent Properties of Five Zinc(II) Metal-Organic Frameworks. *Cryst. Growth Des.* **2015**, *15* (3), 1481–1491.

(29) Phukan, N.; Goswami, S.; Lipstman, S.; Goldberg, I.; Tripuramallu, B. K. Solvent Influence in Obtaining Diverse Coordination Symmetries of Dy(III) Metal Centers in Coordination Polymers: Synthesis, Characterization, and Luminescent Properties. *Cryst. Growth Des.* **2020**, *20* (5), 2973–2984.

(30) Frahm, D.; Hoffmann, F.; Fröba, M. Two Metal-Organic Frameworks with a Tetratopic Linker: Solvent-Dependent Polymorphism and Postsynthetic Bromination. *Cryst. Growth Des.* **2014**, *14* (4), 1719–1725.

(31) Hwang, J.; Yan, R.; Oschatz, M.; Schmidt, B. V. K. J. Solvent Mediated Morphology Control of Zinc MOFs as Carbon Templates for Application in Supercapacitors. *J. Mater. Chem. A* **2018**, *6* (46), 23521–23530.

(32) Bunzen, H.; Grzywa, M.; Hambach, M.; Spirkl, S.; Volkmer, D. From Micro to Nano: A Toolbox for Tuning Crystal Size and Morphology of Benzotriazolate-Based Metal–Organic Frameworks. *Cryst. Growth Des.* **2016**, *16* (6), 3190–3197.

(33) Kondo, M.; Takashima, Y.; Seo, J.; Kitagawa, S.; Furukawa, S. Control over the Nucleation Process Determines the Framework Topology of Porous Coordination Polymers. *CrystEngComm* **2010**, *12* (8), 2350.

(34) Liu, Y.; Qi, Y.; Su, Y.-H.; Zhao, F.-H.; Che, Y.-X.; Zheng, J.-M. Five Novel Cobalt Coordination Polymers: Effect of Metal–Ligand Ratio and Structure Characteristics of Flexible Bis(Imidazole) Ligands. *CrystEngComm* **2010**, *12* (10), 3283.

(35) Fatima, R.; Park, S.; Kim, J.-O. Effect of Molar Ration of Ti/Ligand on the Synthesis of MIL-125(Ti) and Its Adsorption and Photocatalytic Properties. *J. Ind. Eng. Chem.* **2020**, *90*, 166–177.

(36) Gao, Q.; Xie, Y.-B.; Li, J.-R.; Yuan, D.-Q.; Yakovenko, A. A.; Sun, J.-H.; Zhou, H.-C. Tuning the Formations of Metal–Organic Frameworks by Modification of Ratio of Reactant, Acidity of Reaction System, and Use of a Secondary Ligand. *Cryst. Growth Des.* **2012**, *12* (1), 281–288.

(37) Zhang, J.; Wang, C.; Wang, Y.; Chen, W.; Cifuentes, M. P.; Humphrey, M. G.; Zhang, C. Single Cyanide-Bridged Mo(W)/S/Cu Cluster-Based Coordination Polymers: Reactant- and Stoichiometry-Dependent Syntheses, Effective Photocatalytic Properties. *J. Solid State Chem.* **2015**, *231*, 230–238.

(38) Kan, W.-Q.; Ma, J.-F.; Liu, Y.-Y.; Wu, H.; Yang, J. PH-Dependent Assembly of Two Octamolybdate Hybrid Materials: A Self-Threading CdSO4-Type Framework and a 3D 4-Connected Framework. *CrystEngComm* **2011**, *13* (23), 7037.

(39) Li, S.-L.; Tan, K.; Lan, Y.-Q.; Qin, J.-S.; Li, M.-N.; Du, D.-Y.; Zang, H.-Y.; Su, Z.-M. PH-Dependent Binary Metal−Organic Compounds Assembled from Different Helical Units: Structural Variation and Supramolecular Isomers. *Cryst. Growth Des.* **2010**, *10* (4), 1699–1705.

(40) Gabriel, C.; Perikli, M.; Raptopoulou, C. P.; Terzis, A.; Psycharis, V.; Mateescu, C.; Jakusch, T.; Kiss, T.; Bertmer, M.; Salifoglou, A. PH-Specific Hydrothermal Assembly of Binary and Ternary Pb(II)-(O,N-Carboxylic Acid) Metal Organic Framework Compounds: Correlation of Aqueous Solution Speciation with Variable Dimensionality Solid-State Lattice Architecture and Spectroscopic Signatures. *Inorg. Chem.* **2012**, *51* (17), 9282–9296.

(41) Chi-Durán, I.; Enríquez, J.; Manquian, C.; Wrighton-Araneda, K.; Cañon-Mancisidor, W.; Venegas-Yazigi, D.; Herrera, F.; Singh, D. P. PH-Controlled Assembly of 3D and 2D Zinc-Based Metal-Organic Frameworks with Tetrazole Ligands. *ACS Omega* **2018**, *3* (1), 801–807.

(42) Amo-Ochoa, P.; Zamora, F. Coordination Polymers with Nucleobases: From Structural Aspects to Potential Applications. *Coord. Chem. Rev.* **2014**, *276*, 34–58.

(43) Lu, X.; Ye, J.; Sun, Y.; Bogale, R. F.; Zhao, L.; Tian, P.; Ning, G. Ligand Effects on the Structural Dimensionality and Antibacterial Activities of Silver-Based Coordination Polymers. *Dalt. Trans.* **2014**, *43* (26), 10104.

(44) Bozdemir, Ö. A.; Büyükcakir, O.; Akkaya, E. U. Novel Molecular Building Blocks Based on the Boradiazaindacene Chromophore: Applications in Fluorescent Metallosupramolecular Coordination Polymers. *Chem. - A Eur. J.* **2009**, *15* (15), 3830–3838.

(45) Journaux, Y.; Ferrando-Soria, J.; Pardo, E.; Ruiz-Garcia, R.; Julve, M.; Lloret, F.; Cano, J.; Li, Y.; Lisnard, L.; Yu, P.; et al. Design of Magnetic Coordination Polymers

Built from Polyoxalamide Ligands: A Thirty Year Story. *Eur. J. Inorg. Chem.* **2018**, *2018* (3), 228–247.

(46) Li, B.; Wen, H.-M.; Cui, Y.; Qian, G.; Chen, B. Multifunctional Lanthanide Coordination Polymers. *Prog. Polym. Sci.* **2015**, *48*, 40–84.

(47) Gomez, G. E.; D'vries, R. F.; Lionello, D. F.; Aguirre-Díaz, L. M.; Spinosa, M.; Costa, C. S.; Fuertes, M. C.; Pizarro, R. A.; Kaczmarek, A. M.; Ellena, J.; et al. Exploring Physical and Chemical Properties in New Multifunctional Indium-, Bismuth-, and Zinc-Based 1D and 2D Coordination Polymers. *Dalt. Trans.* **2018**, *47* (6), 1808–1818.

(48) Nasalevich, M. A.; van der Veen, M.; Kapteijn, F.; Gascon, J. Metal–Organic Frameworks as Heterogeneous Photocatalysts: Advantages and Challenges. *CrystEngComm* **2014**, *16* (23), 4919–4926.

(49) Lim, D.-W.; Sadakiyo, M.; Kitagawa, H. Proton Transfer in Hydrogen-Bonded Degenerate Systems of Water and Ammonia in Metal–Organic Frameworks. *Chem. Sci.* **2019**, *10* (1), 16–33.

(50) Mileo, P. G. M.; Adil, K.; Davis, L.; Cadiau, A.; Belmabkhout, Y.; Aggarwal, H.; Maurin, G.; Eddaoudi, M.; Devautour-Vinot, S. Achieving Superprotonic Conduction with a 2D Fluorinated Metal–Organic Framework. *J. Am. Chem. Soc.* **2018**, *140* (41), 13156–13160.

(51) Ye, Y.; Guo, W.; Wang, L.; Li, Z.; Song, Z.; Chen, J.; Zhang, Z.; Xiang, S.; Chen, B. Straightforward Loading of Imidazole Molecules into Metal-Organic Framework for High Proton Conduction. *J. Am. Chem. Soc.* **2017**, *139* (44), 15604–15607.

(52) Yang, F.; Xu, G.; Dou, Y.; Wang, B.; Zhang, H.; Wu, H.; Zhou, W.; Li, J.-R.; Chen, B. A Flexible Metal–Organic Framework with a High Density of Sulfonic Acid Sites for Proton Conduction. *Nat. Energy* **2017**, *2* (11), 877–883.

(53) Ponomareva, V. G.; Kovalenko, K. A.; Chupakhin, A. P.; Dybtsev, D. N.; Shutova, E. S.; Fedin, V. P. Imparting High Proton Conductivity to a Metal–Organic Framework Material by Controlled Acid Impregnation. *J. Am. Chem. Soc.* **2012**, *134* (38), 15640–15643.

(54) Dong, X.-Y.; Li, J.-J.; Han, Z.; Duan, P.-G.; Li, L.-K.; Zang, S.-Q. Tuning the Functional Substituent Group and Guest of Metal–Organic Frameworks in Hybrid Membranes for Improved Interface Compatibility and Proton Conduction. *J. Mater. Chem. A* **2017**, *5* (7), 3464–3474.

(55) Shen, L.; Wu, H. Bin; Liu, F.; Brosmer, J. L.; Shen, G.; Wang, X.; Zink, J. I.; Xiao, Q.; Cai, M.; Wang, G.; et al. Creating Lithium-Ion Electrolytes with Biomimetic Ionic

Channels in Metal-Organic Frameworks. *Adv. Mater.* **2018**, *30* (23), 1707476.

(56) Higashi, S.; Miwa, K.; Aoki, M.; Takechi, K. A Novel Inorganic Solid State Ion Conductor for Rechargeable Mg Batteries. *Chem. Commun.* **2014**, *50* (11), 1320–1322.

(57) Park, S. S.; Tulchinsky, Y.; Dincă, M. Single-Ion Li + , Na + , and Mg 2+ Solid Electrolytes Supported by a Mesoporous Anionic Cu–Azolate Metal–Organic Framework. *J. Am. Chem. Soc.* **2017**, *139* (38), 13260–13263.

(58) Fujie, K.; Yamada, T.; Ikeda, R.; Kitagawa, H. Introduction of an Ionic Liquid into the Micropores of a Metal-Organic Framework and Its Anomalous Phase Behavior. *Angew. Chemie Int. Ed.* **2014**, *53* (42), 11302–11305.

(59) Fujie, K.; Otsubo, K.; Ikeda, R.; Yamada, T.; Kitagawa, H. Low Temperature Ionic Conductor: Ionic Liquid Incorporated within a Metal–Organic Framework. *Chem. Sci.* **2015**, *6* (7), 4306–4310.

(60) Interrante, L. V.; Browall, K. W.; Bundy, F. P. Intermolecular Interactions in Transition Metal Complexes. IV. High Pressure Study of Some Mixed-Valence Platinum and Palladium Complexes. *Inorg. Chem.* **1974**, *13* (5), 1158–1162.

(61) Yamashita, M.; Ishii, T.; Matsuzaka, H.; Manabe, T.; Kawashima, T.; Okamoto, H.; Kitagawa, H.; Mitani, T.; Marumoto, K.; Kuroda, S. Tuning of Charge Density Wave Strengths by Competition between Electron−Phonon Interaction of Pd II −Pd IV Mixed-Valence States and Electron Correlation of Ni III States in Quasi-One-Dimensional Bromo-Bridged Ni–Pd Mixed-Metal MX Chain Compounds Ni 1 - X . *Inorg. Chem.* **1999**, *38* (22), 5124–5130.

(62) Takaishi, S.; Yamashita, M.; Matsuzaki, H.; Okamoto, H.; Tanaka, H.; Kuroda, S.; Goto, A.; Shimizu, T.; Takenobu, T.; Iwasa, Y. One-Dimensional Bromo-Bridged NiIII Complexes [Ni(S,S-Bn)2Br]Br2 (S,S-Bn=2S,3S-Diaminobutane): Synthesis, Physical Properties, and Electrostatic Carrier Doping. *Chem. - A Eur. J.* **2008**, *14* (2), 472–477.

(63) Conesa-Egea, J.; Redondo, C. D.; Martínez, J. I.; Gómez-García, C. J.; Castillo, Ó.; Zamora, F.; Amo-Ochoa, P. Supramolecular Interactions Modulating Electrical Conductivity and Nanoprocessing of Copper–Iodine Double-Chain Coordination Polymers. *Inorg. Chem.* **2018**, *57* (13), 7568–7577.

(64) Ogihara, N.; Ohba, N.; Kishida, Y. On/off Switchable Electronic Conduction in Intercalated Metal-Organic Frameworks. *Sci. Adv.* **2017**, *3* (8), 1603103.

(65) Dutta, B.; Dey, A.; Sinha, C.; Ray, P. P.; Mir, M. H. Photochemical Structural Transformation of a Linear 1D Coordination Polymer Impacts the Electrical

Conductivity. *Inorg. Chem.* **2018**, *57* (14), 8029–8032.

(66) Huang, X.; Li, H.; Tu, Z.; Liu, L.; Wu, X.; Chen, J.; Liang, Y.; Zou, Y.; Yi, Y.; Sun, J.; et al. Highly Conducting Neutral Coordination Polymer with Infinite Two-Dimensional Silver–Sulfur Networks. *J. Am. Chem. Soc.* **2018**, *140* (45), 15153–15156.

(67) Huang, X.; Sheng, P.; Tu, Z.; Zhang, F.; Wang, J.; Geng, H.; Zou, Y.; Di, C.; Yi, Y.; Sun, Y.; et al. A Two-Dimensional π–d Conjugated Coordination Polymer with Extremely High Electrical Conductivity and Ambipolar Transport Behaviour. *Nat. Commun.* **2015**, *6* (1), 7408.

(68) Dhara, B.; Nagarkar, S. S.; Kumar, J.; Kumar, V.; Jha, P. K.; Ghosh, S. K.; Nair, S.; Ballav, N. Increase in Electrical Conductivity of MOF to Billion-Fold upon Filling the Nanochannels with Conducting Polymer. *J. Phys. Chem. Lett.* **2016**, *7* (15), 2945–2950.

(69) Thürmer, K.; Schneider, C.; Stavila, V.; Friddle, R. W.; Léonard, F.; Fischer, R. A.; Allendorf, M. D.; Talin, A. A. Surface Morphology and Electrical Properties of Cu 3 BTC 2 Thin Films Before and After Reaction with TCNQ. *ACS Appl. Mater. Interfaces* **2018**, *10* (45), 39400–39410.

(70) Kahn, O. Dinuclear Complexes with Predictable Magnetic Properties. *Angew. Chemie Int. Ed. English* **1985**, *24* (10), 834–850.

(71) Wang, J.; Zakrzewski, J. J.; Zychowicz, M.; Vieru, V.; Chibotaru, L. F.; Nakabayashi, K.; Chorazy, S.; Ohkoshi, S. Holmium(<scp>iii</Scp>) Molecular Nanomagnets for Optical Thermometry Exploring the Luminescence Re-Absorption Effect. *Chem. Sci.* **2021**, *12* (2), 730–741.

(72) Miyasaka, H.; Julve, M.; Yamashita, M.; Clérac, R. Slow Dynamics of the Magnetization in One-Dimensional Coordination Polymers: Single-Chain Magnets. *Inorg. Chem.* **2009**, *48* (8), 3420–3437.

(73) Caneschi, A.; Gatteschi, D.; Lalioti, N.; Sangregorio, C.; Sessoli, R.; Venturi, G.; Vindigni, A.; Rettori, A.; Pini, M. G.; Novak, M. A. Cobalt(II)-Nitronyl Nitroxide Chains as Molecular Magnetic Nanowires. *Angew. Chemie Int. Ed.* **2001**, *40* (9), 1760–1763.

(74) Ferbinteanu, M.; Miyasaka, H.; Wernsdorfer, W.; Nakata, K.; Sugiura, K.; Yamashita, M.; Coulon, C.; Clérac, R. Single-Chain Magnet (NEt 4)[Mn 2 (5-MeOsalen) 2 Fe(CN) 6] Made of Mn III −Fe III −Mn III Trinuclear Single-Molecule Magnet with an S T = 9 / 2 Spin Ground State. *J. Am. Chem. Soc.* **2005**, *127* (9), 3090–3099.

(75) Feng, X.; David Harris, T.; Long, J. R. Influence of Structure on Exchange Strength

and Relaxation Barrier in a Series of FeIIReIV(CN)2 Single-Chain Magnets. *Chem. Sci.* **2011**, *2* (9), 1688.

(76) Vaz, M. G. F.; Cassaro, R. A. A.; Akpinar, H.; Schlueter, J. A.; Lahti, P. M.; Novak, M. A. A Cobalt Pyrenylnitronylnitroxide Single-Chain Magnet with High Coercivity and Record Blocking Temperature. *Chem. - A Eur. J.* **2014**, *20* (18), 5460–5467.

(77) Li, H.; Xi, L.; Jing, P.; Tang, J.; Wang, Q.; Yang, H.; Zhai, L.; Niu, Y.; Ding, L.; Song, Z. Multifunctional Properties Existing in Ln–Nitronyl Nitroxide Single-Chain Magnets. *J. Mater. Chem. C* **2021**, *9* (1), 294–302.

(78) Liu, J.; Sun, Q. Enhanced Ferromagnetism in a Mn 3 C 12 N 12 H 12 Sheet. *ChemPhysChem* **2015**, *16* (3), 614–620.

(79) Mínguez Espallargas, G.; Coronado, E. Magnetic Functionalities in MOFs: From the Framework to the Pore. *Chem. Soc. Rev.* **2018**, *47* (2), 533–557.

(80) Wang, Z.; Hu, K.; Gao, S.; Kobayashi, H. Formate-Based Magnetic Metal-Organic Frameworks Templated by Protonated Amines. *Adv. Mater.* **2010**, *22* (13), 1526–1533.

(81) Beauvais, L. G.; Long, J. R. Co 3 [Co(CN) 5] 2 : A Microporous Magnet with an Ordering Temperature of 38 K. *J. Am. Chem. Soc.* **2002**, *124* (41), 12096–12097.

(82) Bloch, E. D.; Queen, W. L.; Krishna, R.; Zadrozny, J. M.; Brown, C. M.; Long, J. R. Hydrocarbon Separations in a Metal-Organic Framework with Open Iron(II) Coordination Sites. *Science (80-.).* **2012**, *335* (6076), 1606–1610.

(83) Jeon, I.-R.; Negru, B.; Van Duyne, R. P.; Harris, T. D. A 2D Semiquinone Radical-Containing Microporous Magnet with Solvent-Induced Switching from T c = 26 to 80 K. *J. Am. Chem. Soc.* **2015**, *137* (50), 15699–15702.

(84) Grancha, T.; Ferrando-Soria, J.; Castellano, M.; Julve, M.; Pasán, J.; Armentano, D.; Pardo, E. Oxamato-Based Coordination Polymers: Recent Advances in Multifunctional Magnetic Materials. *Chem. Commun.* **2014**, *50* (57), 7569–7585.

(85) Calvo Galve, N.; Giménez-Marqués, M.; Palomino, M.; Valencia, S.; Rey, F.; Mínguez Espallargas, G.; Coronado, E. Isostructural Compartmentalized Spin-Crossover Coordination Polymers for Gas Confinement. *Inorg. Chem. Front.* **2016**, *3* (6), 808–813.

(86) Muñoz, M. C.; Real, J. A. Thermo-, Piezo-, Photo- and Chemo-Switchable Spin Crossover Iron(II)-Metallocyanate Based Coordination Polymers. *Coord. Chem. Rev.* **2011**, *255* (17–18), 2068–2093.

(87) Arcís-Castillo, Z.; Muñoz-Lara, F. J.; Muñoz, M. C.; Aravena, D.; Gaspar, A. B.;

Sánchez-Royo, J. F.; Ruiz, E.; Ohba, M.; Matsuda, R.; Kitagawa, S.; et al. Reversible Chemisorption of Sulfur Dioxide in a Spin Crossover Porous Coordination Polymer. *Inorg. Chem.* **2013**, *52* (21), 12777–12783.

(88) Clemente-León, M.; Coronado, E.; López-Jordà, M.; Waerenborgh, J. C.; Desplanches, C.; Wang, H.; Létard, J.-F.; Hauser, A.; Tissot, A. Stimuli Responsive Hybrid Magnets: Tuning the Photoinduced Spin-Crossover in Fe(III) Complexes Inserted into Layered Magnets. *J. Am. Chem. Soc.* **2013**, *135* (23), 8655–8667.

(89) Zhao, T.; Boldog, I.; Spasojevic, V.; Rotaru, A.; Garcia, Y.; Janiak, C. Solvent-Triggered Relaxative Spin State Switching of [Fe(HB(Pz) 3) 2] in a Closed Nano-Confinement of NH 2 -MIL-101(Al). *J. Mater. Chem. C* **2016**, *4* (27), 6588–6601.

(90) Clemente-León, M.; Coronado, E.; Gómez-García, C. J.; López-Jordà, M.; Camón, A.; Repollés, A.; Luis, F. Insertion of a Single-Molecule Magnet inside a Ferromagnetic Lattice Based on a 3D Bimetallic Oxalate Network: Towards Molecular Analogues of Permanent Magnets. *Chem. - A Eur. J.* **2014**, *20* (6), 1669–1676.

(91) Salomon, W.; Lan, Y.; Rivière, E.; Yang, S.; Roch-Marchal, C.; Dolbecq, A.; Simonnet-Jégat, C.; Steunou, N.; Leclerc-Laronze, N.; Ruhlmann, L.; et al. Single-Molecule Magnet Behavior of Individual Polyoxometalate Molecules Incorporated within Biopolymer or Metal-Organic Framework Matrices. *Chem. - A Eur. J.* **2016**, *22* (19), 6564–6574.

(92) Gai, Y.-L.; Jiang, F.-L.; Chen, L.; Bu, Y.; Su, K.-Z.; Al-Thabaiti, S. A.; Hong, M.-C. Photophysical Studies of Europium Coordination Polymers Based on a Tetracarboxylate Ligand. *Inorg. Chem.* **2013**, *52* (13), 7658–7665.

(93) Gai, Y.; Jiang, F.; Chen, L.; Wu, M.; Su, K.; Pan, J.; Wan, X.; Hong, M. Europium and Terbium Coordination Polymers Assembled from Hexacarboxylate Ligands: Structures and Luminescent Properties. *Cryst. Growth Des.* **2014**, *14* (3), 1010–1017.

(94) de Oliveira Maciel, J. W.; Lemes, M. A.; Valdo, A. K.; Rabelo, R.; Martins, F. T.; Queiroz Maia, L. J.; de Santana, R. C.; Lloret, F.; Julve, M.; Cangussu, D. Europium(III), Terbium(III), and Gadolinium(III) Oxamato-Based Coordination Polymers: Visible Luminescence and Slow Magnetic Relaxation. *Inorg. Chem.* **2021**.

(95) Feng, S.; Yang, H.; Jiang, X.; Wang, Y.; Zhu, M. A New 3D Silver(I) Coordination Polymer with Croconate Ligand Displaying Green Luminescent. *J. Mol. Struct.* **2015**, *1081*, 1–5.

(96) Yang, Y.; Wang, K.-Z.; Yan, D. Ultralong Persistent Room Temperature Phosphorescence of Metal Coordination Polymers Exhibiting Reversible PH-

Responsive Emission. *ACS Appl. Mater. Interfaces* **2016**, *8* (24), 15489–15496.

(97) Tsai, M.-J.; Li, C.-Y.; Wu, J.-Y. Luminescent Zn(<scp>ii</Scp>) Coordination Polymers as Efficient Fluorescent Sensors for Highly Sensitive Detection of Explosive Nitroaromatics. *CrystEngComm* **2018**, *20* (42), 6762–6774.

(98) Conesa-Egea, J.; González-Platas, J.; Rodríguez-Mendoza, U. R.; Martínez, J. I.; Pilar, O.; Fernández-Moreira, V.; Costa, R. D.; Fernández-Cestau, J.; Zamora, F.; Amo-Ochoa, P. Cunning Defects: Emission Control by Structural Point Defects on Cu(<scp>i</Scp>)I Double Chain Coordination Polymers. *J. Mater. Chem. C* **2020**, *8* (4), 1448–1458.

(99) Zhan, C.; Ou, S.; Zou, C.; Zhao, M.; Wu, C.-D. A Luminescent Mixed-Lanthanide-Organic Framework Sensor for Decoding Different Volatile Organic Molecules. *Anal. Chem.* **2014**, *86* (13), 6648–6653.

(100) Aguirre-Díaz, L. M.; Echeverri, M.; Paredes-Gil, K.; Snejko, N.; Gómez-Lor, B.; Gutiérrez-Puebla, E.; Monge, M. Á. The Effect of Auxiliary Nitrogenated Linkers on the Design of New Cadmium-Based Coordination Polymers as Sensors for the Detection of Explosive Materials. *Chem. – A Eur. J.* **2021**, *27* (16), 5298–5306.

(101) Luo, Y.; Zhang, L.; Zhang, L.; Yu, B.; Wang, Y.; Zhang, W. Multiporous Terbium Phosphonate Coordination Polymer Microspheres as Fluorescent Probes for Trace Anthrax Biomarker Detection. *ACS Appl. Mater. Interfaces* **2019**, *11* (17), 15998–16005.

(102) Molnár, G.; Cobo, S.; Real, J. A.; Carcenac, F.; Daran, E.; Vieu, C.; Bousseksou, A. A Combined Top-Down/Bottom-Up Approach for the Nanoscale Patterning of Spin-Crossover Coordination Polymers. *Adv. Mater.* **2007**, *19* (16), 2163–2167.

(103) Lv, R.; Terrones, H.; Elías, A. L.; Perea-López, N.; Gutiérrez, H. R.; Cruz-Silva, E.; Rajukumar, L. P.; Dresselhaus, M. S.; Terrones, M. Two-Dimensional Transition Metal Dichalcogenides: Clusters, Ribbons, Sheets and More. *Nano Today* **2015**, *10* (5), 559–592.

(104) Portoles-Gil, N.; Parra-Aliana, R.; Álvarez-Larena, Á.; Domingo, C.; Ayllón, J. A.; López-Periago, A. Bottom-up Approach for the Preparation of Hybrid Nanosheets Based on Coordination Polymers Made of Metal–Diethyloxaloacetate Complexes Linked by 4,4′-Bipyridine. *CrystEngComm* **2017**, *19* (34), 4972–4982.

(105) Foster, J. A.; Henke, S.; Schneemann, A.; Fischer, R. A.; Cheetham, A. K. Liquid Exfoliation of Alkyl-Ether Functionalised Layered Metal–Organic Frameworks to Nanosheets. *Chem. Commun.* **2016**, *52* (69), 10474–10477.

(106) Suchomel, P.; Kvitek, L.; Prucek, R.; Panacek, A.; Halder, A.; Vajda, S.; Zboril, R.

Simple Size-Controlled Synthesis of Au Nanoparticles and Their Size-Dependent Catalytic Activity. *Sci. Rep.* **2018**, *8* (1), 4589.

(107) Grassian, V. H. When Size Really Matters: Size-Dependent Properties and Surface Chemistry of Metal and Metal Oxide Nanoparticles in Gas and Liquid Phase Environments. *J. Phys. Chem. C* **2008**, *112* (47), 18303–18313.

(108) Zhao, J.; Yang, Y.; Han, X.; Liang, C.; Liu, J.; Song, X.; Ge, Z.; Liu, Z. Redox-Sensitive Nanoscale Coordination Polymers for Drug Delivery and Cancer Theranostics. *ACS Appl. Mater. Interfaces* **2017**, *9* (28), 23555–23563.

(109) Wang, C.; Han, Q.; Mo, F.; Chen, M.; Xiong, Z.; Fu, Y. Novel Luminescent Nanostructured Coordination Polymer: Facile Fabrication and Application in Electrochemiluminescence Biosensor for MicroRNA-141 Detection. *Anal. Chem.* **2020**, *92* (18), 12145–12151.

(110) Wang, Y.-M.; Liu, W.; Yin, X.-B. Self-Limiting Growth Nanoscale Coordination Polymers for Fluorescence and Magnetic Resonance Dual-Modality Imaging. *Adv. Funct. Mater.* **2016**, *26* (46), 8463–8470.

(111) Karim, S.; Mukherjee, S.; Mahapatra, S.; Parveen, R.; Das, D. Green Facile Synthesis to Develop Nanoscale Coordination Polymers as Lysosome-Targetable Luminescent Bioprobes. *Biomater. Sci.* **2021**, *9* (1), 124–132.

(112) Hermosa, C.; Vicente Álvarez, J.; Azani, M.-R.; Gómez-García, C. J.; Fritz, M.; Soler, J. M.; Gómez-Herrero, J.; Gómez-Navarro, C.; Zamora, F. Intrinsic Electrical Conductivity of Nanostructured Metal-Organic Polymer Chains. *Nat. Commun.* **2013**, *4* (1), 1709.

(113) Ares, P.; Amo-Ochoa, P.; Soler, J. M.; Palacios, J. J.; Gómez-Herrero, J.; Zamora, F. High Electrical Conductivity of Single Metal-Organic Chains. *Adv. Mater.* **2018**, *30* (21), 1705645.

(114) Cui, Y.; Yan, J.; Chen, Z.; Zhang, J.; Zou, Y.; Sun, Y.; Xu, W.; Zhu, D. [Cu 3 (C 6 Se 6)] N : The First Highly Conductive 2D π–d Conjugated Coordination Polymer Based on Benzenehexaselenolate. *Adv. Sci.* **2019**, *6* (9), 1802235.

(115) López, J.; Platas, J. G.; Rodríguez-Mendoza, U. R.; Martínez, J. I.; Delgado, S.; Lifante-Pedrola, G.; Cantelar, E.; Guerrero-Lemus, R.; Hernández-Rodríguez, C.; Amo-Ochoa, P. Cu(I)–I-2,4-Diaminopyrimidine Coordination Polymers with Optoelectronic Properties as a Proof of Concept for Solar Cells. *Inorg. Chem.* **2021**, *60* (2), 1208–1219.

(116) Urtizberea, A.; Natividad, E.; Alonso, P. J.; Andrés, M. A.; Gascón, I.; Goldmann, M.; Roubeau, O. A Porphyrin Spin Qubit and Its 2D Framework Nanosheets. *Adv. Funct.*

Mater. **2018**, *28* (31), 1801695.

CHAPTER 2. NANOSCALE COORDINATION POLYMER BASED ON Cu(II) AND MODIFIED THYMINE AS OLIGONUCLEOTIDE CARRIER

2.1. Introduction

Coordination polymers are materials that can be easily adjusted to different conditions, because of the wide variety of building blocks, the different morphologies, the various chemical and physical properties, and the possibility of changing their size from the micro to the nanoscale. Those are the reasons that turn them into the perfect candidates for a field in continuous development such as biomedical applications. A specific area like biomedicine requires to build a biocompatible coordination polymer starting from the right selection of building blocks. The metal centers that constitute this type of coordination polymers are usually trace elements like iron, zinc, copper, or manganese[1]. Trace metals ions are those present in small amounts in living tissues and are known to be part of essential functions[2]. In addition to their biocompatibility, these metals ions are chosen according to other interesting properties that they can add to

the coordination polymers, for example conductivity, magnetism, or luminescence; transforming these compounds in multifunctional materials. In the case of the organic ligands, it should be pointed out the use of biomolecules[3]. Biomolecules provide several advantages by themselves, such as multiple metal-binding sites, structural flexibility, chirality, target recognition, or self-assembly properties. There is a wide range of possibilities, but it is common to use small molecules like amino acids, nucleobases, peptides, or saccharides[4–7]. Obtaining a biologically compatible coordination polymer requires it also to be stable in physiological environments over time and adjust the size of the material to the new targets present in a living system being like tissues, cells, or proteins.

One of the most common application of biocompatible coordination polymers is as carriers. Usually, porous coordination polymers or MOFs are loaded with anticancer drugs and used as drug delivery systems[8,9]. However, there are other promising therapies to treat a variety of diseases based on the transport of therapeutic nucleic acids[10]. It is a highly specific method (antisense oligonucleotides[11] or RNA therapies[12]) for particular targets with a limited number of side effects. The current virus SARS-CoV-2 or COVID-19 has placed these therapies at the forefront with the vaccines based in *m*RNA[13]. The ability to design a biocompatible structure and the stability of coordination polymers turns them into good candidates as carriers for gene delivery.

In this chapter, a new 1D coordination polymer was designed with a modified nucleobase as ligand. The synthesis of this biocompatible material opens the door to use it as carrier of oligonucleotides.

2.2. Results and Discussion

A new coordination polymer has been prepared using copper(II) as the metal center because, apart from their biocompatibility, this metal can provide conductive and magnetic properties[1415]. Copper(II) with their d^9 configuration has a characteristic coordination behavior, a tetragonal environment that can influence the final structure of the coordination polymer. Using a nucleobase as the main ligand contributes with all the advantages mentioned before, such as the multiple donor positions available for metal coordination[16]. However, with the intention of setting the nucleobase moiety free, a modified nucleobase with a carboxylic acid is selected, more specifically, *thymine-1-acetic acid* (TAcOH). Carboxylic acid as a functional group is chosen by its ability to attract divalent metal ions when it is negatively charged and the multiple coordination modes (Figure 2.1). Finally, to generate polymeric structures, 4,4'-bipyridine (4,4'-bipy) has been selected as neutral N-donor ligand to contribute as a rigid connector between metal centers and add aromaticity which can encourage electrical conductivity pathways[17] .

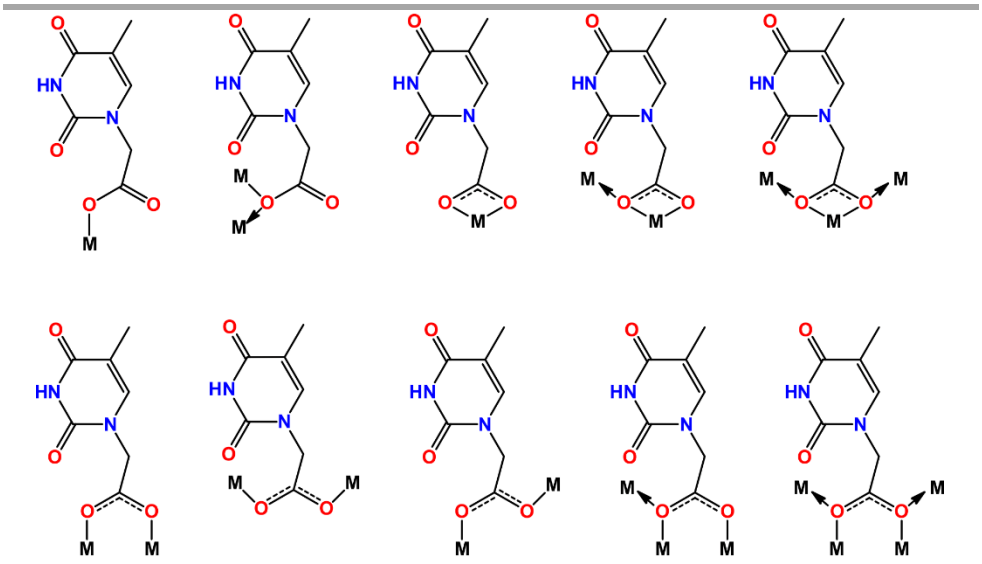

Figure 2.1. General coordination modes of the carboxyl group oxygen to a transition metal center. Adapted from Reference 8.

The hydrothermal reaction between a copper(II) salt, 4,4'-bipyridine and thymine-1-acetic acid produces crystals of **CP1** (Figure 2.2). The single crystals of **CP1** obtained by hydrothermal reaction allowed us to determine their structure by single-crystal X-ray diffraction (SCXRD).

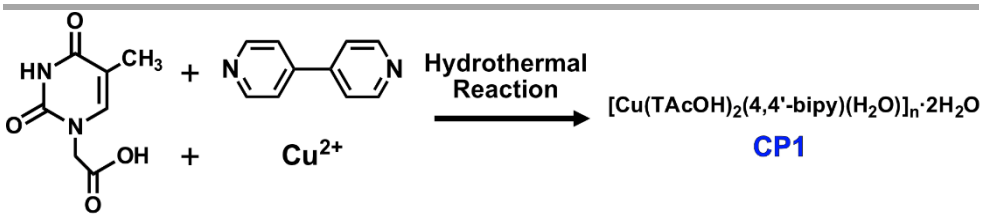

Figure 2.2. Scheme of the synthesis of crystals of **CP1**.

The crystal structure of **CP1** with formula **$[Cu(TAcO)_2(4,4'\text{-bipy})(H_2O)]_n \cdot 2H_2O$** consists of 1D chains in which 4,4´-bipyridine ligands bridge the metal centers (Figure 2.3a and Tables A2.1, A2.2 and A2.3 page 179). The coordination sphere of the copper(II) metal center adopts an axially elongated square pyramid geometry. The basal plane is occupied by two carboxylate oxygen atoms from two thymine-1-acetate ligands in *trans* arrangement and by two nitrogen atoms from two 4,4'-bipyridine ligands. The apical position is occupied by a water molecule (Figure 2.3b). The shape of the coordination polymer in the solid state is best described as a linear ribbon of dimensions 1.9 x 0.8 nm (Figure 2.3c). A supramolecular 3D structure is also formed by a complex network of hydrogen bonds, where are remarkable the stronger hydrogen bonds stablished between the water molecules as a donor to the carboxylate oxygen atoms and as acceptor from the thymine N3-H position. There are also C-H···O hydrogen bonds involving the aromatic C-H positions of the 4,4´-bipyridine bridging ligand and thymine residue as donors and the thymine ketone groups as acceptors. It is worth noting that there are no base-pairing interactions between the thymine residues, probably due to the presence of water molecules that disrupt these interactions (Figure 2.2c). Moreover, there is no evidence of π-π stacking interactions.

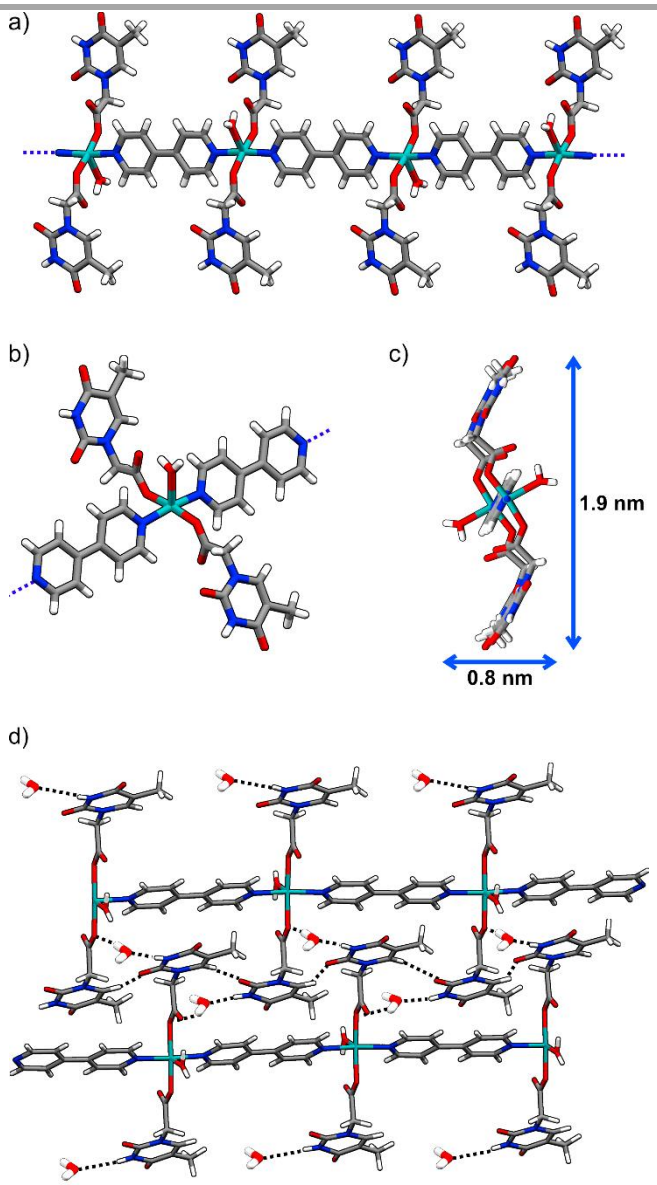

Figure 2.3. Frontal (a) and lateral (b) views of a fragment of the infinite coordination polymer **CP1**. (c) Fragment of the crystal structure showing lateral the dimension for a single chain. (d) Fragment of the supramolecular 3D structure showing some of the most relevant hydrogen bonding interactions (green). Colour code: Cu (light blue), N (blue), O (red), C (grey) and H (white).

Once the structure is known, a more sustainable reaction is carried out with milder conditions. Each building block is first dissolved in water, secondly, they are mixed at room temperature, and as a result, a stable colloid of the coordination polymer is immediately formed. These conditions allow us to obtain a polycrystalline blue powder of **CP1**. However, coordination polymers are generally insoluble once they are formed[18], so the use of usual characterization techniques like nuclear magnetic resonance (NMR), which needs the compounds to be in solution, is precluded in this case. This restricts the characterization techniques to solid state techniques like powder X-ray diffraction (PXRD), an essential technique to compare the powder compounds obtained with the original coordination polymer structure. PXRD pattern obtained from **CP1** (Figure 2.4a) enabled the comparison with the calculated diffraction patterns of the crystals and confirmed that the polycrystalline powders obtained are the previously described coordination polymers. In addition, an attenuated total reflectance Fourier transform infrared (ATR-FT-IR) spectroscopy and elemental analysis were performed. The IR spectrum of **CP1** shows the appearance of two revealing bands between 3500 and 3400 cm^{-1} indicating the presence of O-H bonds that can be attributed to the water molecule in apical position. The other zone of interest in the spectrum are the bands between 1700 and 1500 cm^{-1} that confirm the presence of C=O bonds from the carboxylate of the thymine ligand and C=N bonds from the

4,4'-bipyridine ligands (Figure 2.4b). The result of elemental analysis of **CP1** (see section A2.2.2, page 177) confirm the composition of the material.

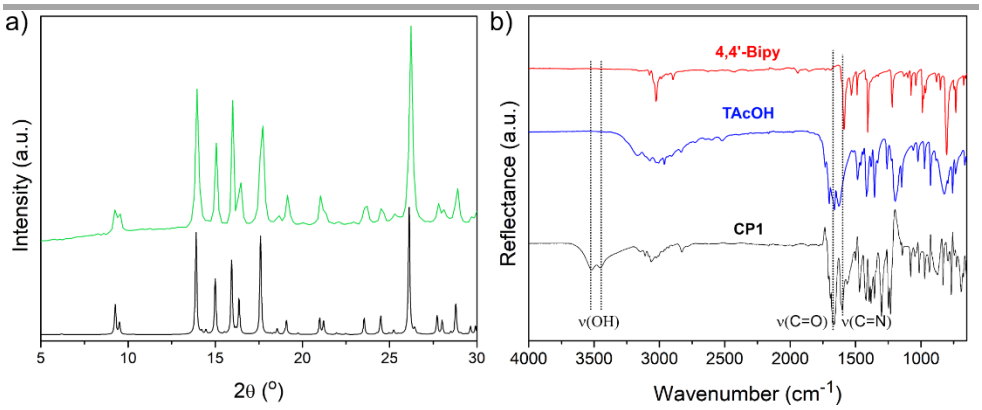

Figure 2.4. a) PXRD pattern of **CP1** (green) and simulated PXRD pattern (black). b) ATR-FT-IR spectra of 4,4'-bipy (red), TAcOH (blue) and CP1 (black).

Once that it has been corroborated that the blue powder obtained in mild conditions is **CP1**, the characterization continues. It is crucial to know the morphology and size of the coordination polymer obtained, so scanning electron microscopy (SEM) is used. The SEM images of **CP1** show a morphology of ribbons with homogeneous widths and thickness of approximately 2 µm and 650 nm respectively and different lengths from 3 to 10 µm (Figure 2.5). The great variety in the length of the ribbons is normal if those of the smallest size are considered as fragments of the longer ones.

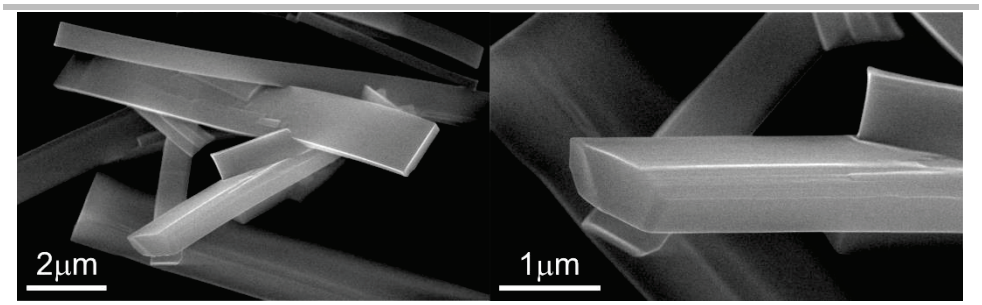

Figure 2.5. FESEM images of **CP1**.

However, one of the aims of this work is to look for potential biological applications, which require to work with materials with smaller sizes. Between the different ways to obtain nanostructured coordination polymers, a direct synthesis was chosen to change the dimensions of **CP1**. Nanostructured CP1 (**CP1n**) was obtained at room temperature, using water as solvent in the same way that in CP1 at room temperature, but with an increased concentration of reactants, causing a fast precipitation of the compound. The coordination polymer **CP1n** is obtained again in a colloidal form.

The new nano coordination polymer **CP1n** was characterized by PXRD, ATR-FT-IR and elemental analysis to confirm that the obtained compound is the coordination polymer we were looking for (Figure 2.6 and section A2.2.3, page 178)

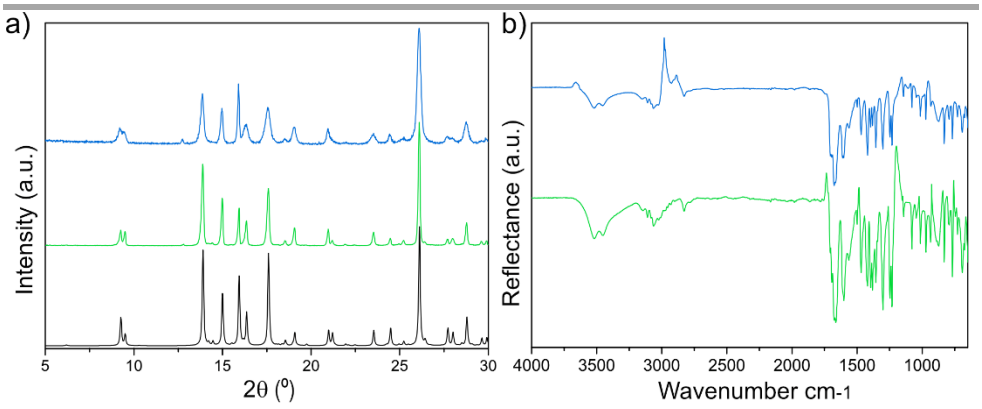

Figure 2.6. a) PXRD patterns of **CP1** (green), **CP1n** (blue) and simulated PXRD pattern (black). b) ATR-FT-IR spectra of **CP1** (green) and **CP1n** (blue).

Once it has been confirmed that **CP1n** is the coordination polymer, microscopy techniques are used to know if the size has changed. SEM images of **CP1n** determined that the compound has the same morphology of ribbons of micrometric lengths, widths between 100-150 nm and lengths from 3 to 7 µm. The widths show a clear decrease of size and a high homogeneity compared with the lengths (Figure 2.7a-b). To complete the characterization, the compound was studied by atomic force microscope (AFM). The AFM images obtained upon deposition by drop casting of a diluted suspension of the initial colloid on SiO_2 (see section A2.2.6, page 181) confirmed the width of the nanoribbons observed by SEM (Figure 2.7c-d). Moreover, the observed typical height within a range from *ca*. 15 to 60 nm is consistent with the isolation of ribbons comprising *ca*. 12-50 molecules by comparison with the structure obtained by X-ray diffraction (Figure 2.2c).

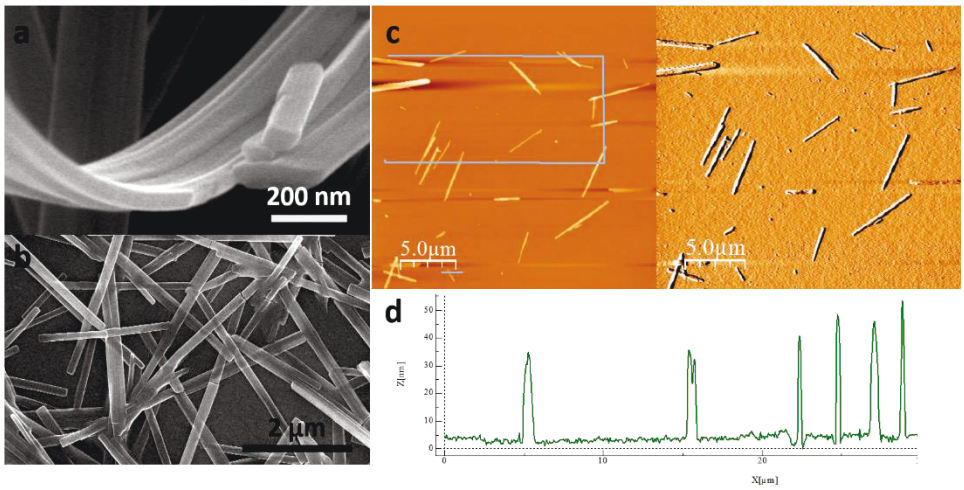

Figure 2.7. (a,b) SEM images of **CP1n**. (c) AFM image of nanoribbons from compound **CP1n**. (d) Height profile along the blue line in (c).

It has been previously mentioned that coordination polymers are multifunctional materials that can show properties from the metal centers or ligands. **CP1** has Cu(II) as a metal center, which can provide magnetic and conductive properties[19,20]. The coordination polymer has also the Cu(II) centers bridged by the 4,4'-bipyridine ligands. This ligand has an aromatic character; therefore, its charge is delocalized between the rings and can contribute to forming electrical conduction pathways. The electrical conductivity of **CP1** has been measured employing the two contacts method (Figure 2.8a). A single crystal is connected between two wolfram tips, and a voltage sweep is applied between -10V and +10V at room temperature. Simultaneously, the electrical current that flows through the crystal

because of the voltage is measured. An I/V curve (Figure 2.9b) is obtained, and the resistance can be derived using Ohm's law:

$$\boldsymbol{V = I \cdot R}$$

Where V is the voltage, I the current and R the resistance.

However, resistance depends on the geometric parameters of the sample, and the quantity that is exclusively related to the material is the resistivity (ρ), whose expression is:

$$\boldsymbol{\rho = R \cdot \frac{w}{l}}$$

Where w is the cross-section of the crystal, and l is the distance between the two contact points.

Finally, conductivity (σ) is the inverse of resistivity. The measurements have been carried out with different crystals at 300 K and the mean value of conductivity is $6.6 \cdot 10^{-6}$ S/cm in **CP1.** This electrical conductivity value is consistent with 1D coordination polymers where copper is bridged by aromatic nitrogen donor ligands[21].

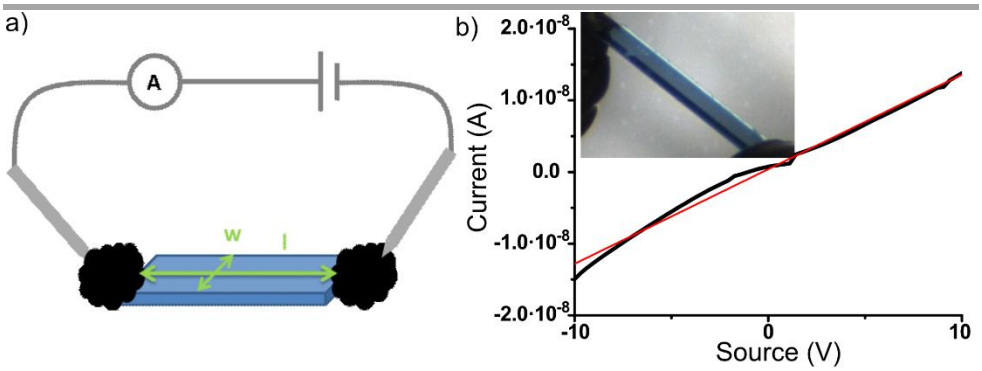

Figure 2.8. (a) General scheme of two-contact method. (b) I/V curve of a crystal of **CP1** with inset of the crystal with graphite ink.

The Cu(II) metal center can also provide magnetic properties to coordination polymers, so magnetic studies were performed in **CP1**. To evaluate if there can be an effect of size in the magnetic properties, **CP1n** was also studied and compared. On the one hand, **CP1** displays a paramagnetic behavior with a very weak antiferromagnetic Cu-Cu coupling expected in Cu(II) complexes with long bipyridine bridges (Figure 2.9). However, magnetic properties of **CP1n** do not fit with a straightforward chain model even with inter-chain interactions, suggesting that although the nanoscale coordination polymer presents the same crystal structure as the bulk, the magnetic structure is different. Other possibilities cannot be discarded, but this different behavior can be attributed to the large shape-anisotropy of the nanoribbons, which gives rise to a preferential orientation with the chain axis always located perpendicular to the magnetic field[22] (Figure 2.9).

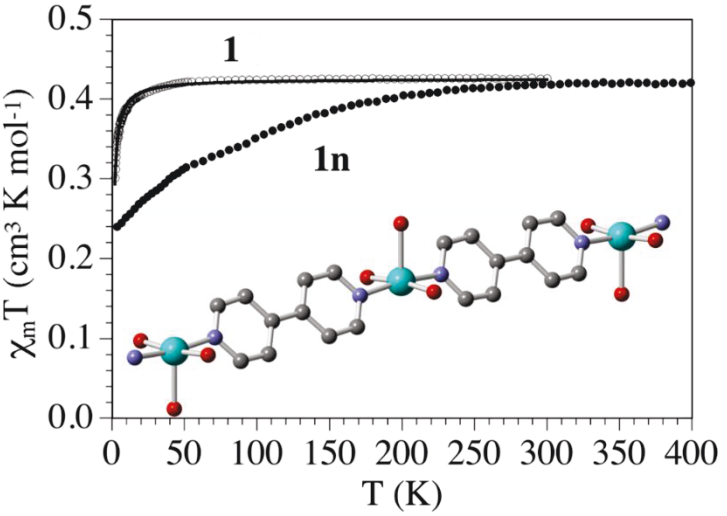

Figure 2.9. Thermal variation of χmT per Cu(II) ion for a crystalline sample of bulk polymer (**CP1**) and of the same compound prepared as nanoribbons (**CP1n**).

Once **CP1** and **CP1n** have been fully characterized, it should be noted the biological potential of the free thymine residue along the chain. However, before beginning any biological study, it is essential to check the stability of **CP1n** under different conditions such as time, pH, or concentration. First, the differences between one sample of **CP1n** freshly prepared and the same sample after their storage as a colloid for one month at room temperature were compared. Both samples were characterized by SEM, PXRD and IR to compare the changes in the morphology or the structure (Figure 2.10). The SEM images show that there are not significant modifications in the size of the ribbons, but the average width shows a slight increase from 185 to 290 nm (inset histograms in 2.10a-b).

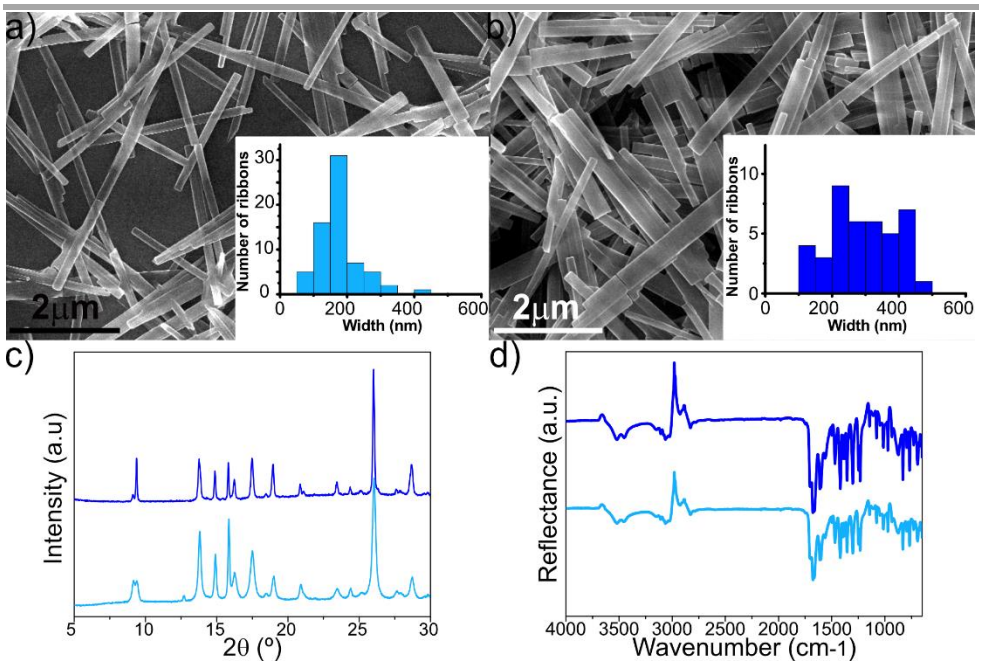

Figure 2.10. FESEM images and inset of corresponding histograms of a freshly prepared **CP1n** sample (a) and the same sample after one month (b). c) PXRD patterns and d) ATR-FT-IR spectrum of **CP1n** freshly prepared (light blue) and one month stored (deep blue).

A change in the pH of the media can be usual when biological studies are carried out. Therefore, the initial pH obtained when **CP1n** is prepared in water (6.1) is modified until 7 by addition of NaOH solution (0.01M). Any change in morphology or structure is monitored again by SEM, PXRD and IR, respectively. SEM images and corresponding histograms once more do not show significant changes, only a slight increase in the width from 185 to 235 nm (Figure 2.11a-b). Although the PXRD pattern and the IR spectra of **CP1n** at pH = 7 exhibit only a few different peaks, this means a change in the structure.

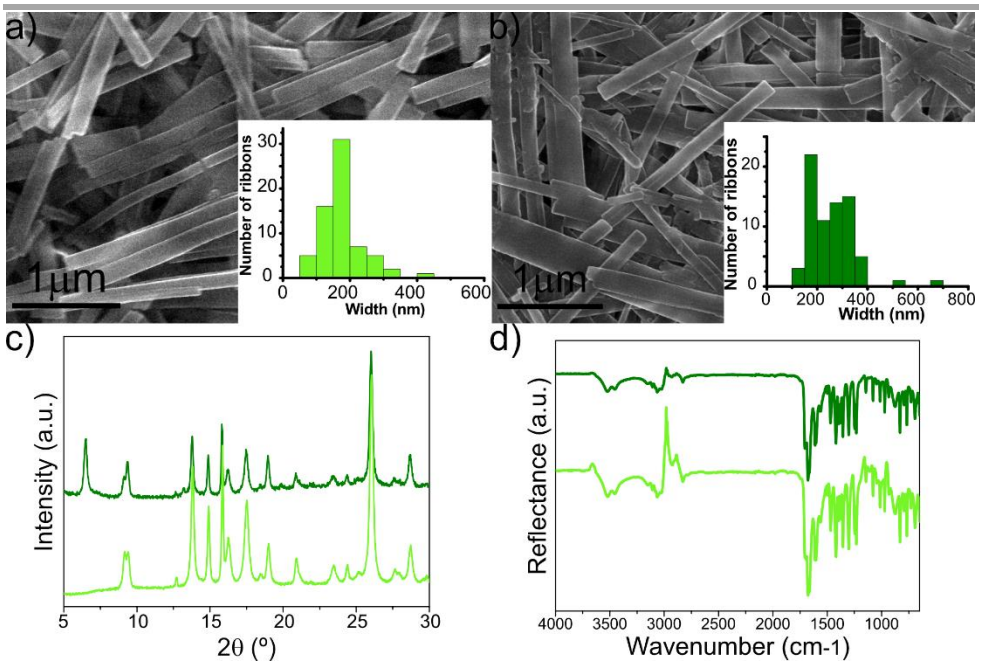

Figure 2.11. FSEM images and inset of corresponding histograms of a **CP1n** sample prepared following the synthetic procedure (pH = 6.1) (a) and the same sample at pH = 7.4 (b). c) PXRD patterns and d) ATR-FT-IR spectrum of **CP1n** at pH = 6.1 (light green) and after modified at pH = 7 (deep green).

Finally, other conditions to have into account are concentration changes. In this case, **CP1n** prepared following the standard synthetic procedure where the initial concentration of the reactants is 0.1 M is compared to the one with an increased concentration of 0.2 M. Once again, the results of this experiment are checked by SEM, PXRD and IR. The PXRD patterns and the IR spectrum show that an increase in the concentration does not involve structural changes (Figure 2.12c-d). However, SEM images show that a higher concentration in the reactants homogenize the length of the nanoribbons to 1-2 μm

(Figure 2.12a-b). It is remarkable that **CP1n** is very stable under different conditions, and no significant variations in neither shape nor structure were detected.

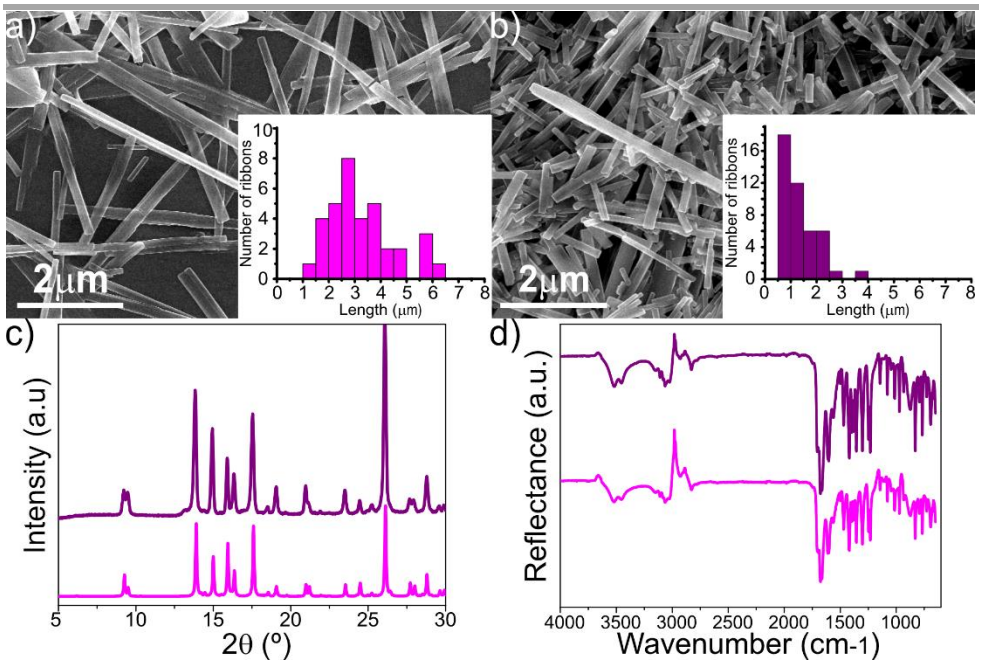

Figure 2.12. FESEM images and inset of corresponding histograms of a) **CP1n** sample prepared following the standard synthetic procedure (0.1 M) and b) a sample prepared with a concentration of 0.2 M. c) PXRD patterns and d) ATR-FT-IR spectrum of **CP1n** initial concentration of 0.1 M (pink) and 0.2 M (purple).

The free thymine residue in the coordination polymer leads us to study the molecular recognition capacity of **CP1n** towards adenine to form the base pairing T-A like in DNA. To evaluate this interaction, the nanoribbons were incubated with oligonucleotides containing different base sequences, particularly those detailed in Table 2.1.

Name	Sequence
Poly A	5'-dAdAdAdAdAdAdAdAdA-3'
Poly C	5'-dCdCdCdCdCdCdCdCdC-3'
Poly G	5'-dGdGdGdGdGdGdGdGdG-3'
Poly T	5'-dTdTdTdTdTdTdTdTdT-3'
SCR	5'-dTdAdAdAdGdTdGdCdTdTdAdTdAdGdTdGdCdAdGdGdTdAdG-3'

Table 2.1. Oligonucleotides containing different base sequences.

The results were collected in Figure 2.13, where the percentage of oligo bound to **CP1n** is represented. As expected, there is an efficient interaction between thymine and adenine. **CP1n** shows a significant selectivity for the binding to the PolyA sequence (35 %) in comparison to PolyT (9 %), PolyC (23 %), PolyG (21 %) and a scramble oligonucleotide sequence SCR (5 %). It is noticeable that the interaction of CP1n with PolyC and PolyG is significantly higher than that with PolyT. This might be due to the high affinity of cytosine residues for copper(II)[23] and the observed formation of stable wobble base pairs between guanines and thymines[2425]. The results obtained confirm the ability of **CP1n** to stablish interactions with oligonucleotides by conventional Watson-Crick base pairs and/or more complex interactions such as non-canonical base pairs and metal–nucleobase interactions.

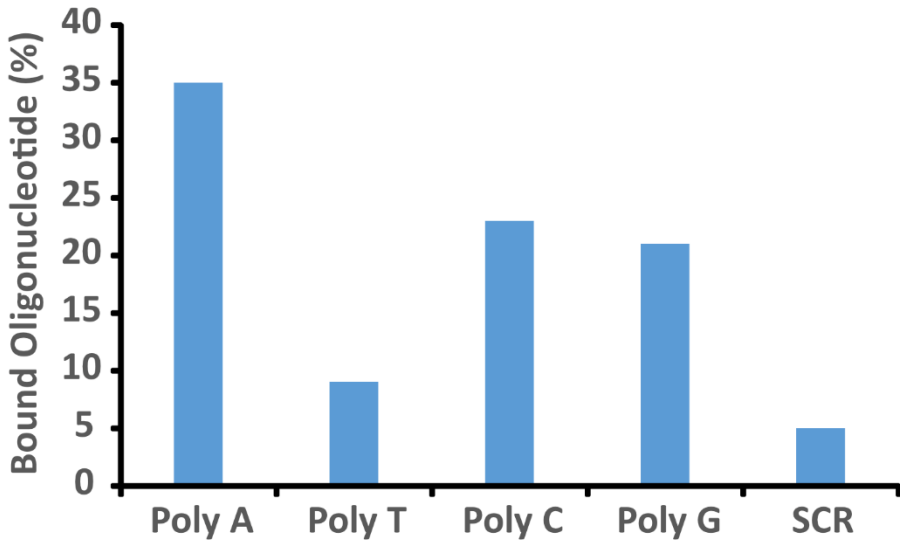

Figure 2.13. Affinity of different oligonucleotide sequences represented as % of the bound material.

The presence of copper in the coordination polymer might limit its use due to its potential toxicity. For this reason, the toxicity of **CP1n** was evaluated in different cell lines to test the biocompatibility. The effect was studied in uveal melanoma (C918), pancreatic cancer (Panc-1) and nontumoral (HaCaT) cell lines. Interestingly, some toxicity was only observed when the concentration of the polymer was high (>100 μM) and concentrations below this threshold did not significantly affect the viability of the cells (Figure 2.14).

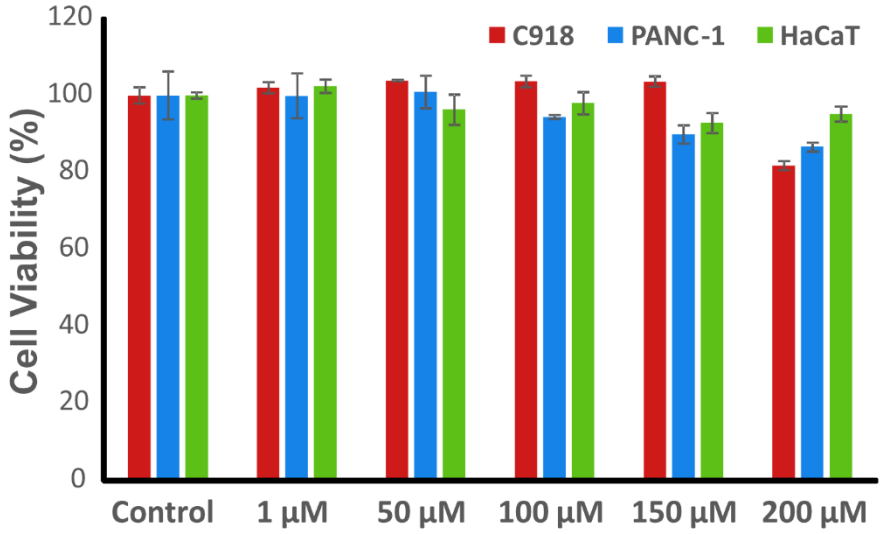

Figure 2.14. Cell viability study using different concentrations of **CP1n**.

Knowing that the nanoscale coordination polymer shows a preferential interaction with PolyA over other single strand oligonucleotide sequences and that it is non-toxic, its behavior in cells was studied, specifically as a nanocarrier. A suspension of **CP1n** containing adenine oligonucleotide sequences labelled with fluorescein was incubated with cells of the C918 line for 3 h. Afterwards, the cells were washed and analyzed in a fluorescence microscope (Figure 2.15). As can be observed in the images, after 3 h the PolyA with **CP1n** has been able to penetrate in the majority of cells; in contrast, in the blank experiment with only PolyA no fluorescence could be detected inside the cells. This fact confirms that **CP1n** can be employed as a nanocarrier.

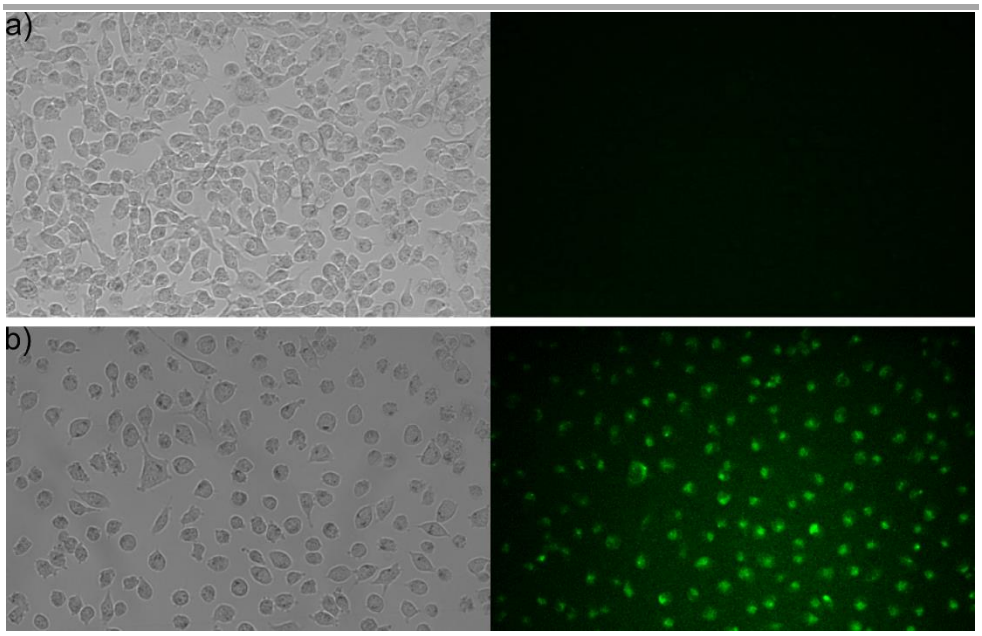

Figure 2.15. a) C918 cells incubated with PolyA labelled with fluorescein. b) C918 cells incubated with **CP1n** treated with PolyA labelled with fluorescein.

2.3. Conclusions

In this chapter, a new coordination polymer was synthesized using a modified nucleobase as ligand (**CP1**) and it was demonstrated that it is possible to decrease their size to the nanoscale (**CP1n**) through a simple method of fast precipitation. The advantage of the structure with a free thymine moiety enabled their study with oligonucleotides with different sequences, showing some selectivity towards the oligonucleotide bearing adenine. Finally, **CP1n** was tested with success as nanocarrier of an adenine oligonucleotide in cells.

2.4. References

(1) Ali Altaf, A. Medicinal Importance of Some Metal Cluster Compounds. *J. Drug Des. Med. Chem.* **2016**, *2* (1), 1.

(2) Al-fartusie, F. S.; Mohssan, S. N. Indian Journal of Advances in Chemical Science Essential Trace Elements and Their Vital Roles in Human Body. *Indian J. Adv. Chem. Sci.* **2017**, *5*, 127–136.

(3) Zhuang, J.; Young, A. P.; Tsung, C.-K. Integration of Biomolecules with Metal-Organic Frameworks. *Small* **2017**, *13* (32), 1700880.

(4) Smokrović, K.; Muratović, S.; Karadeniz, B.; Užarević, K.; Žilić, D.; Dilović, I. Synthon Robustness and Structural Modularity of Copper(II) Two-Dimensional Coordination Polymers with Isomeric Amino Acids and 4,4'-Bipyridine. *ACS Appl. Mater. Interfaces* **2020**.

(5) García-Terán, J. P.; Castillo, O.; Luque, A.; García-Couceiro, U.; Román, P.; Lezama, L. An Unusual 3D Coordination Polymer Based on Bridging Interactions of the Nucleobase Adenine. *Inorg. Chem.* **2004**, *43* (15), 4549–4551.

(6) Martí-Gastaldo, C.; Antypov, D.; Warren, J. E.; Briggs, M. E.; Chater, P. A.; Wiper, P. V.; Miller, G. J.; Khimyak, Y. Z.; Darling, G. R.; Berry, N. G.; et al. Side-Chain Control of Porosity Closure in Single-and Multiple-Peptide-Based Porous Materials by Cooperative Folding. *Nat. Chem.* **2014**, *6* (4), 343–351.

(7) Smaldone, R. A.; Forgan, R. S.; Furukawa, H.; Gassensmith, J. J.; Slawin, A. M. Z.; Yaghi, O. M.; Stoddart, J. F. Metalorganic Frameworks from Edible Natural Products. *Angew. Chemie - Int. Ed.* **2010**, *49* (46), 8630–8634.

(8) Lian, H.-Y.; Hu, M.; Liu, C.-H.; Yamauchi, Y.; Wu, K. C. W. Highly Biocompatible, Hollow Coordination Polymer Nanoparticles as Cisplatin Carriers for Efficient Intracellular Drug Delivery. *Chem. Commun.* **2012**, *48* (42), 5151.

(9) Taherzade, S. D.; Rojas, S.; Soleimannejad, J.; Horcajada, P. Combined Cutaneous Therapy Using Biocompatible Metal-Organic Frameworks. *Nanomaterials* **2020**, *10* (12), 2296.

(10) Sridharan, K.; Gogtay, N. J. Therapeutic Nucleic Acids: Current Clinical Status. *Br. J. Clin. Pharmacol.* **2016**, *82* (3), 659–672.

(11) Bennett, C. F.; Kordasiewicz, H. B.; Cleveland, D. W. Antisense Drugs Make Sense for Neurological Diseases. *Annu. Rev. Pharmacol. Toxicol.* **2021**, *61* (1), 831–852.

(12) Adams, D.; Gonzalez-Duarte, A.; O'Riordan, W. D.; Yang, C.-C.; Ueda, M.; Kristen, A. V.; Tournev, I.; Schmidt, H. H.; Coelho, T.; Berk, J. L.; et al. Patisiran, an RNAi Therapeutic, for Hereditary Transthyretin Amyloidosis. *N. Engl. J. Med.* **2018**, *379* (1), 11–21.

(13) Teijaro, J. R.; Farber, D. L. COVID-19 Vaccines: Modes of Immune Activation and Future Challenges. *Nat. Rev. Immunol.* **2021**, *0123456789*.

(14) Vegas, V. G.; Maldonado, N.; Castillo, O.; Gómez-García, C. J.; Amo-Ochoa, P. Multifunctional Coordination Polymers Based on Copper with Modified Nucleobases, Easily Modulated in Size and Conductivity. *J. Inorg. Biochem.* **2019**, *200* (August), 110805.

(15) Massoud, S. S.; Junk, T.; Louka, F. R.; Herchel, R.; Trávníček, Z.; Fischer, R. C.; Mautner, F. A. Synthesis, Structure and Magnetic Characterization of Dinuclear Copper(II) Complexes Bridged by Bicompartmental Phenolate. *RSC Adv.* **2015**, *5* (106), 87139–87150.

(16) Amo-Ochoa, P.; Zamora, F. Coordination Polymers with Nucleobases: From Structural Aspects to Potential Applications. *Coord. Chem. Rev.* **2014**, *276*, 34–58.

(17) Talin, A. A.; Centrone, A.; Ford, A. C.; Foster, M. E.; Stavila, V.; Haney, P.; Kinney, R. A.; Szalai, V.; El Gabaly, F.; Yoon, H. P.; et al. Tunable Electrical Conductivity in Metal-Organic Framework Thin-Film Devices. *Science (80-.).* **2014**, *343* (6166), 66–69.

(18) Janiak, C. Engineering Coordination Polymers towards Applications. *Dalt. Trans.* **2003**, No. 14, 2781.

(19) Liu, Q.; Liu, X.; Shi, C.; Zhang, Y.; Feng, X.; Cheng, M.; Su, S.; Gu, J. A Copper-Based Layered Coordination Polymer: Synthesis, Magnetic Properties and Electrochemical Performance in Supercapacitors. *Dalt. Trans.* **2015**, *44* (44), 19175–19184.

(20) Prasad, R. L.; Kushwaha, A. Synthesis, Characterization, and Solid State Electrical Conductivity of Coordination Polymers with Copper and Zinc. *J. Coord. Chem.* **2012**, *65* (23), 4230–4244.

(21) Givaja, G.; Amo-Ochoa, P.; Gómez-García, C. J.; Zamora, F. Electrical Conductive Coordination Polymers. *Chem. Soc. Rev.* **2012**, *41* (1), 115–147.

(22) Liu, K.; Shen, Z.-R.; Li, Y.; Han, S.-D.; Hu, T.-L.; Zhang, D.-S.; Bu, X.-H.; Ruan, W.-J. Solvent Induced Rapid Modulation of Micro/Nano Structures of Metal

Carboxylates Coordination Polymers: Mechanism and Morphology Dependent Magnetism. *Sci. Rep.* **2014**, *4*, 1–7.

(23) Zimmer, C.; Luck, G.; Fritzsche, H.; Triebel, H. DNA-Copper(II) Complex and the DNA Conformation. *Biopolymers* **1971**, *10* (3), 441–463.

(24) Ananth, P.; Goldsmith, G.; Yathindra, N. An Innate Twist between Crick's Wobble and Watson-Crick Base Pairs. *RNA* **2013**, *19* (8), 1038–1053.

(25) Westhof, E. Isostericity and Tautomerism of Base Pairs in Nucleic Acids. *FEBS Lett.* **2014**, *588* (15), 2464–2469.

CHAPTER 3. BIOCOMPATIBLE COORDINATION POLYMER AS 3D PRINTABLE INK

3.1. Introduction

In recent years, a new fabrication technique that shines over the rest is 3D printing. The quick development of this process has turned into a great chance in different areas such as industry, food or medicine[1–3]. Initially, 3D printers were an expensive technology only available at industrial scale, but their quick development has enabled to approach this technique to everybody from laboratories to homes. However, the materials that are needed to use 3D printers continue to be expensive, not environmentally friendly, or too specific[4]. Therefore, searching for new materials able to act as inks suitable for printing is a challenge nowadays[5]. Coordination polymers, which have a wide range of physical and chemical properties, are a great option for this process. However, the quantities needed to print are huge and there are only a few cases in which these materials can be obtained at a large enough scale, which it does not guarantee that can be printed. Once a material is optimized for 3D printing, the multiple shapes that can adopt allow them to develop different functions, being a good example all the medical devices or personal protective equipment like ventilator valves, filters or face shields that have been printed since the beginning of the COVID-19 pandemic[6].

In this chapter, the necessary process to 3D print a biocompatible coordination polymer and its use as a humidity sensor is described.

3.2. Results and Discussion

The previous chapter shows a simple way to obtain a nanoscale coordination polymer in water at room temperature (**CP1n**). These favorable conditions, which can be considered within the principles of *green chemistry,* enable to think about an industrial use of **CP1n**.

One leading technique whose use is every time more often is 3D printing. The wide range of printable objects that can be obtained goes from electronic materials[7] to human bones or tissues[8,9]. This variety in the printed objects require of specific materials, which will depend on the function of the device. Therefore, our non-toxic colloid of **CP1n** can be a good candidate as a printable ink. First, it is essential to be able to scale **CP1n** to bigger quantities that allow the compound to be printed.

Sometimes scaling-up a process from laboratory to industrial scale does not provide the expected results. The principal problems are the equipment used in the reaction, which needs to be of bigger size or the reactions conditions, which can be possibly hard to implement. Thus, trying to scale-up the one-pot synthesis of **CP1n** in mild conditions seems a feasible fact. Moreover, the necessary quantities to be able of 3D printing **CP1n** only required to scale from 4 mL to 4 L, which still enables to use the equipment and installations of a research laboratory. Therefore, the same procedure to obtain **CP1n** was employed to achieve the coordination polymer at a large scale (Figure 3.1a). Each one of the reagents was dissolved in 1 L of water and mixed in a big bottle, giving as a result 4 L of blue colloidal **CP1n** (Figure 3.1b).

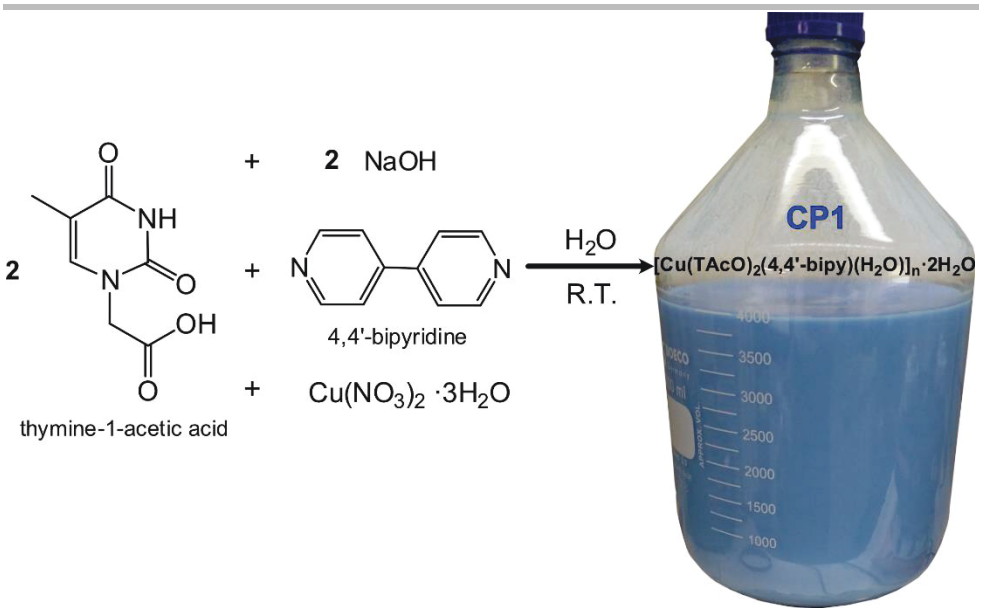

Figure 3.1. Scheme of the synthesis of **CP1n** and photograph of the blue colloid of **CP1n** resultant from the scale-up synthesis in 4 L.

To confirm that the blue colloid obtained corresponds to the structure, size and morphology of **CP1n**, the solid was analyzed by PXRD and SEM (Figure 3.2). The PXRD pattern corroborates that the crystalline compound obtained at large scale is **CP1n** and the SEM images show the previously mentioned ribbon shape morphology around 150-200 nm in width and between 3-7 µm in length.

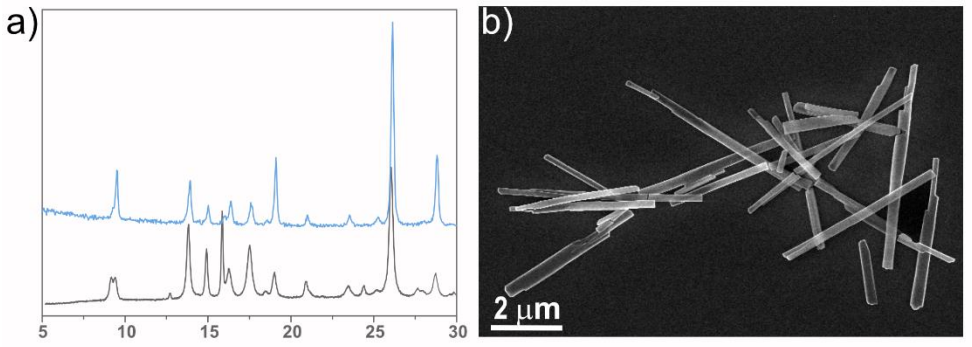

Figure 3.2. a) PXRD pattern of **CP1n** at large scale (blue) and **CP1n** (black). b) FE-SEM images of **CP1n** at large scale.

Once **CP1n** is achieved by scaling-up the synthesis, the compound is processed as an ink for 3D printing. To create a printable ink of **CP1n**, it is necessary to disperse the coordination polymer within a photo-crosslinkable monomer. In this case, the previous biological studies of **CP1n** have led to choose dipropylene glycol diacrylate, a biodegradable monomer. It is also required to add another monomer (ethoxylated trimethylolpropane triacrylate), a solvent (diethylene glycol methyl ether) and photoinitiators (Irgacure 819 and 184) to create the stable polymerizable ink. Embedding **CP1n** withing the matrix (**CP1@3D**) enables to easily handle the material and includes in the printed objects the more advantageous mechanical properties of the chosen monomers. In order to select the best option to obtain different architectures from **CP1@3D**, two different printers were used to 3D print, a Digital Light Processing (DLP) printer and an extrusion printer (Figure 3.3).

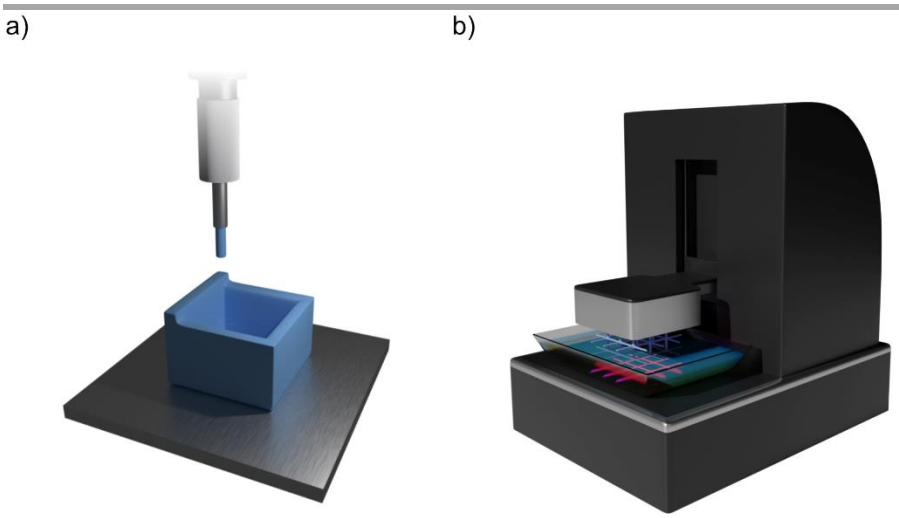

Figure 3.3. Operating scheme of a DLP printer. a) Extruder 3D-printer. b) Digital light processing (DLP) 3D-printer.

However, the high viscosity of the ink only allows the DLP printer to load 10 wt% of **CP1n**, whereas the extruder printer is able to use the 40 wt% formulation. Different constructions of **CP1@3D** (Figure 3.4a-c) were printed with a resolution of 200 µm, which corresponds to the maximum achieved by the DLP printers used in this experiment. The printed architectures of **CP1@3D** were characterized by PXRD and SEM and both techniques confirmed that the 3D composites have successfully embedded the coordination polymer **CP1** and their nano- and submicrometric ribbons are homogeneously distributed in the matrix (Figure 3.4d-e and Figure A3.1, page 189).

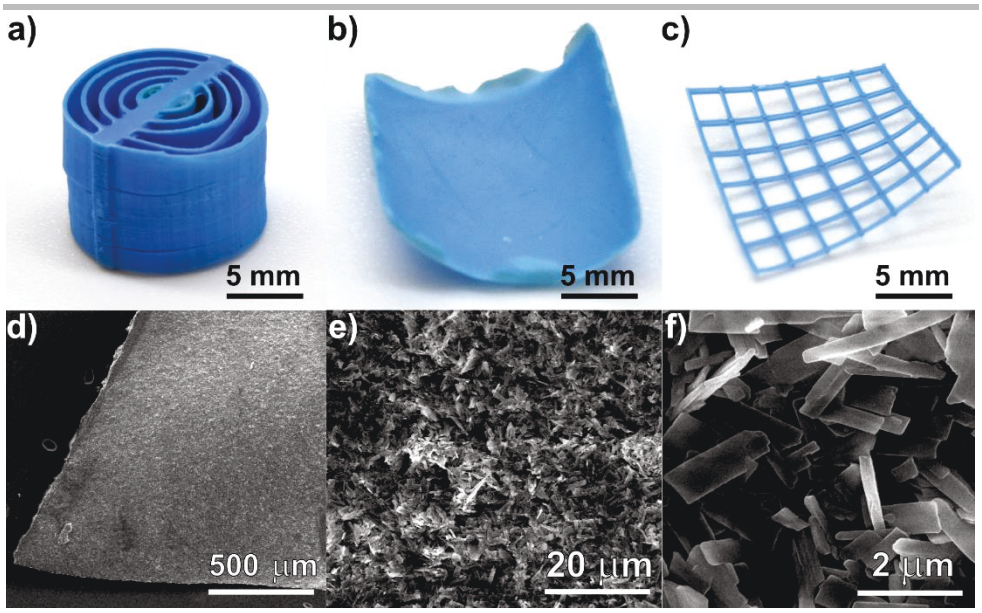

Figure 3.4. a-c) Different 3D printed **CP1@3D** architectures. d-f) SEM images of the 3D printed material by extruding printer at 40 wt% **CP1** sample.

Therefore, a new composite material **CP1@3D** is obtained, in which the coordination polymer **CP1** can be manipulated and tuned in different shapes. Thus, a new range of applications is opened, such as sensors. This application turns into an option after we observed that the material changes their blue color to light purple during the washing process that follows the printing, which uses an alcohol to remove the unreacted materials, suggesting a solvent exchange between **CP1**, with water molecules in its structure, and the alcohol.

Now the focus returns to the structure again. If the crystal structure of **CP1** is remembered, it is formed by a 1D linear chain, in which the copper(II) metal center adopts an axially elongated square pyramid geometry. It is considered elongated geometry because the copper(II)

is displaced 0.140 Å from the basal plane towards the apical position. The apical position of this geometry is occupied by a water molecule, whose coordination bond length is significantly longer than those placed in the basal plane (2.31 vs. 1.97-2.01 Å) (Figure 3.5a). **CP1**, with formula **$[Cu(TAcO)_2(4,4'\text{-bipy})(H_2O)]_n \cdot 2H_2O$**, has also two solvation water molecules, which are involved in the 3D supramolecular structure forming strong hydrogen bonds with the carboxylate oxygen atoms as a donor and with the hydrogen of the thymine (N3-H position) as acceptor (Figure 3.5b). Therefore, there are three water molecules, whose loss or exchange can cause structural changes and as a consequence the color change previously mentioned.

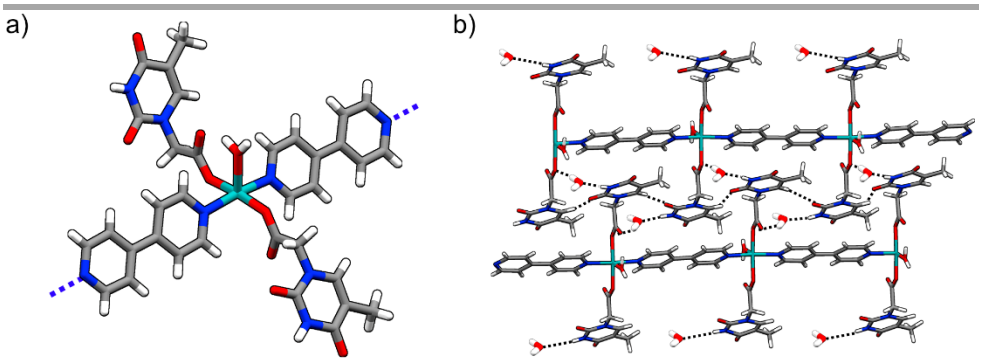

Figure 3.5. a) Coordination sphere of **CP1**. b) Supramolecular 3D structure of **CP1** showing the hydrogen bonding interactions between the coordination polymer and the solvation water. Colour code: Cu (light blue), N (blue), O (red), C (grey) and H (white).

To understand the structural changes of **CP1**, first the thermal stability was studied. A differential scanning calorimetry (DSC) and a thermogravimetric analysis coupled to mass spectroscopy (TGA-MS) were carried out under N_2 atmosphere and air flow respectively

(Figure 3.6). The thermogram (Figure 3.6a) shows a first stage at 60 °C corresponding to the loss of one water molecule ($\Delta m_{experimental}$ = 2.58 % and $\Delta m_{theoretical}$ = 2.75 %), and a second stage at 135 °C corresponding to the loss of two water molecules ($\Delta m_{experimental}$ = 5.47 % and $\Delta m_{theoretical}$ = 5.62 %). Although the experimental values are slightly different than those calculated, it is usual in several differential thermal analysis (DTA-TG) experiments and can be related to the preparation of the material[10]. The MS measurements corroborate these stages as the ionic current indicates that only water is emitted in this step (m/z = 18). The next stages observed from 140 to 500 °C correspond to the loss of organic ligands TAcO and 4,4'-bipy as CO_2 and H_2O gas. On the other hand, two DSC measurements were collected at different heating rates (5 and 10 °C/min) from room temperature to 200 °C. This assay was performed trying to clarify the order in which the water molecules leave the coordination polymer by a significant difference in the bond breaking energies of the dehydration process and also to elucidate what happens at 135 °C. The DSC curves (Figure 3.6b) show in both cases a first thermal event, which coincides with the TGA first step and a second thermal event, which enthalpy is bigger than that of the first thermal event and also coincides with the TGA second step. These events take place at different temperatures depending on the heating rate, suggesting a labile coordination bond for the water molecule. However, distinguishing which of the two lattice water molecules leaves first is not possible because the shape of the second peak and the recovery of the base line at the end are indicative of an overlap between the energy corresponding to the loss of two water molecules and the reaction energy of a new structure emerging,

which occurs when the solvation water molecules are lost and depends on it kinetically and thermodynamically.

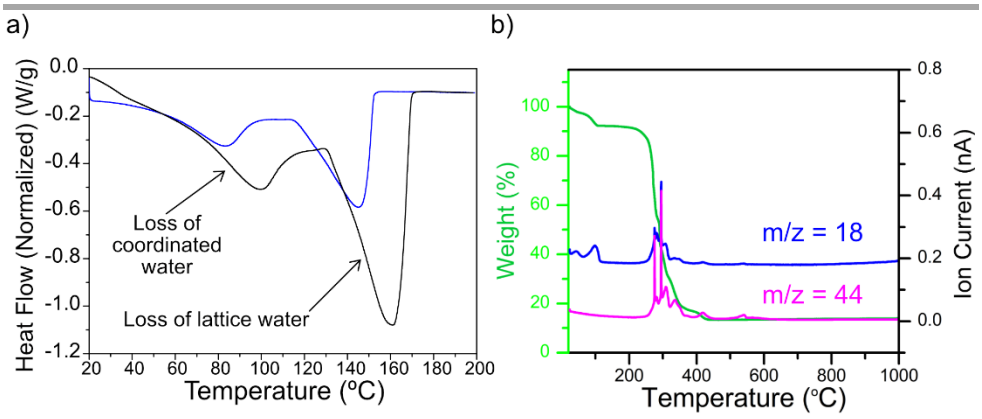

Figure 3.6. a) DSC curves of **CP1** at 5 °C/min (blue) and 10 °C/min (black) heating rates. b) Thermal stability study of **CP1**. The green curve represents the stages of the losses produced. The blue and the pink curves represent the ion currents corresponding to the masses 18 (blue) and 44 (pink) associated with each loss of the previous curves. Only those two are represented from a range of 0 to 200 u.m.a. because there are no more significant signals.

Therefore, **CP1** is capable of losing the three water molecules present in the crystal structure **$[Cu(TAcO)_2(4,4'\text{-bipy})(H_2O)]_n \cdot 2H_2O$** at two different temperatures, 60 °C and 135 °C. If a powder sample of **CP1** is heated at 60 °C around 30 min, a significant color change from blue to violet is observed (Figure 3.7a). This thermochromic behavior at 60 °C is reversible and it is probably caused by the dissociation of the weakly bonded water from the coordination sphere, whose bond is longer than usual as was previously seen. This loss facilitates a simple structural reorganization and when the sample is cooling in air the color changes from violet to blue, so the structure of **CP1** is regenerated upon exposure of the sample to atmospheric moisture.

Although this color change suggests that the cooled sample is again **CP1**, the stability of the process was checked by PXRD (Figure A3.1, page 190). The reproducibility of this process was proven performing more than 20 cycles of heating at 60 °C and cooling in air while following the procedure by PXRD (Figure A3.3, page 190). Thus, an intermediate compound of **CP1** is obtained at 60 °C, which formula is probably $[Cu(TAcO)_2(4,4'\text{-bipy})]_n \cdot 2H_2O$ (named **CP1-H_2O** for simplicity).

However, if the temperature continues increasing from 60 to 135 °C, **CP1-H_2O** changes their color from violet to grayish blue (Figure 3.7a), but this compound does not experiment any color change when is cooled in air. Thus, the loss of the two solvation water molecules at 135 °C results in an irreversible transformation of **CP1** in another compound, which can be formulated as $[Cu(TAcO)_2(4,4'\text{-bipy})]_n$ (named **CP1-$3H_2O$** for simplicity). All these changes experimented by **CP1** with temperature have been corroborated by PXRD, so **CP1** was gradually heated from room temperature to 135 °C and was cooled again to room temperature to check the reversibility of the process (Figure 3.7b-c).

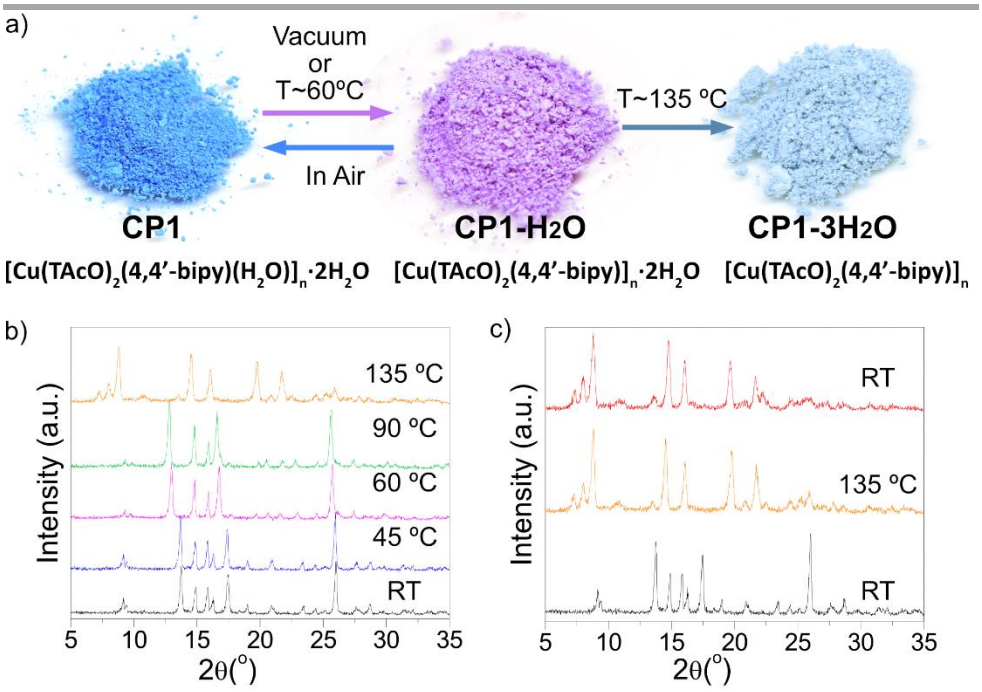

Figure 3.7. a) Photographs of the corresponding powders in the transformation process mediated by either temperature or vacuum from **CP1** to **CP1-H₂O** and from **CP1-H₂O** to **CP1-3H₂O.** b) PXRD patterns of **CP1** at different temperatures. c) PXRD patterns of **CP1** after cooling from 135 °C to room temperature and compare with the initial **CP1** at room temperature.

The PXRD studies with temperature show a clear change in the crystal structure of **CP1** but considering the impossibility of obtaining a crystal suitable for analysis by SXRD, it is necessary to understand and corroborate the structural change observed in the experimental data with additional studies such as pair distribution function (PDF) studies and computational studies.

Computational studies contribute to explain these experimental data from a theoretical point of view. In this case using a density functional

theory (DFT)-based calculation to compute the transition-state energy barrier for the release of the coordinated water molecule from the starting structure of **CP1** (with all water molecules). To carry out these calculations a climbing-image nudged elastic band (CI-NEB) approach was used to get a converged minimum energy path (MEP)[11], considering as the first step the optimized all-water-molecules **CP1** geometry and as the final step the optimized structure with the coordination water molecule removed (**CP1-H_2O**) and a total number of intermediate image states of 20, which were free to relax along the procedure. As a result of this calculation, a transition-state barrier of ΔE = 0.63 eV was obtained (Figure 3.8). Moreover, the rate for this process has been computed by looking at normal modes possessing amplitudes that make the coordinated water molecule detach from the structure. Then the rate is obtained by multiplying the Boltzmann factor (providing the probability to pick up a thermal fluctuation at temperature T to overcome the barrier after "fluctuation", ΔE) and the number of attempts to pass the barrier given by the frequency of the relevant mode: in this case of around 450 cm^{-1}

$$\Gamma = e^{-\left[\frac{\Delta E}{K_B T}\right]}$$

According to the Boltzmann statistics, the values obtained are compatible with the loss of the coordination water molecule at 60 °C within minutes, as noticed experimentally. In line with the previous data, the energy which each solvation water is bounded within the system is calculated by a difference of total energies between the system with solvation waters, the system without solvation waters, and n times the energy of the water molecules, present in the unit

cell. The energy value obtained is 1.16 eV, so to remove the solvation water molecules is necessary a thermal energy that exceeds this cohesion enthalpy of 1.16 eV per molecule. This can also help to justify that in the case of **CP1**, losing the solvation water is more difficult than losing the coordination water.

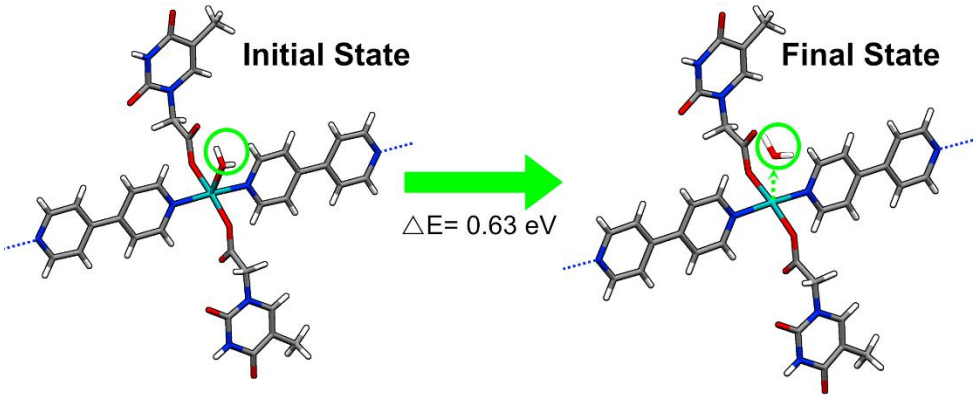

Figure 3.8. Optimized initial and final states for the computation of the transition-state energy barrier for the release of the coordinated water molecule from the **CP1** structure within the CI-NEB approach. Lattice waters have been omitted by clarity.

Other theoretical calculations based on first-principles were carried out to investigate the structural and electronic evolution of **CP1** induced by the sequential loss of the coordinated and solvation water molecules. As a starting point, the geometry and lattice of **CP1** was obtained from the powder X-ray diffraction at room temperature, in which the polymer has a water molecule coordinated to the Cu atom and two solvation water molecules forming hydrogen bonds as donors with the carboxylate oxygen atoms and as acceptors with the hydrogen (N3-H position) of two different thymine ligands (Figure 3.1). This starting structure of **CP1** with all the water molecules is

relaxed, but no significant change is appreciated in the resulting structure (Figures A3.4, page 191). In a next threefold step, i) the coordination water molecule, ii) the two solvation water molecules and iii) the coordination and solvation water molecules simultaneously were removed from the resulting structure. The three new geometries (i, ii and iii) were again fully relaxed (Figures A3.4, page 191) to compare changes with the all-water-molecules case. According with the experimental results, the changes observed in the structure are not very noticeable for optimized cases (i) and (ii), being the most pronounced changes those observed in the Cu-N and Cu-O distances for structure (i) which are decreased (< 4 %) and a slight torsion (< 4 °) of the terminating methyl groups in the TAcO ligands. However, in structure iii, in which all the water molecules have been removed, the Cu-N and Cu-O distances decrease around 6 % and a rotation around 8 ° of the 4,4'-bipy ligands is observed. The experimental PXRD pattern of **CP1** was compared with the simulated PXRD from the DFT-optimized structures with all water molecules, no coordination water molecule, no solvation water molecules, and no water molecules (Figures A3.5, page 192). Despite of the slight geometrical changes previously mentioned, there are not any significant alterations in the simulated PXRD diffractograms corresponding to the optimized structures (Figures A3.5, page 192). These results are consistent with those observed experimentally by PXRD (Figure 3.7b), in which it is observed that the crystal structure remains almost locally unaltered at short-range, but major structural changes are observed at a long-range scale, where, unfortunately, these theoretical studies cannot provide information. This behavior

is in agreement with other similar systems reported previously in literature[12].

To probe the atomic structure of **CP1** a pair distribution function (PDF) analysis was applied. PDF is an analytical technique based on synchrotron X-ray total scattering data that can provide structural information and a quantitative description of the short-range order, which is present in the broad and less clearly-defined features in the diffractogram, as the local atomic structure. Therefore, PDF experiments were carried out in **CP1**, **CP1-H_2O** and **CP1-$3H_2O$** samples to explore the local structural implications linked to dehydration. In the case of **CP1** systems, the PDFs are dominated by atom-atom correlations involving the strongly scattering Cu atoms (Figure 3.9a). The main PDF contribution is noticed at ≈ 2.0 Å, which contains correlations from the overlapping Cu-N and Cu-O distances associated respectively with the binding 4,4'-bipy and TAcO ligands. If this peak at ≈ 2.0 Å is compared with the PDF data collected on **CP1-H_2O**, no significant changes were observed, demonstrating that during the heating process at 60 °C the coordination mode of the ligands to copper remains unaltered. However, if the peak at ≈ 2.3 Å from the **CP1-H_2O** sample heated at 60 °C is compared to the pristine system, a subtle decrease can be appreciated. It is essential to highlight this fact because this bond distance corresponds to the water molecule bound to the copper as well as carbon-carbon correlations within the ligands. A quantitative analysis of this PDF peak suggests the loss of the Cu-O bonds associated with the dehydration of the copper centers, which is in agreement with the data obtained by TGA and theoretical calculation. This result would

indicate that after the heat treatment the coordination number changes from 5 to 4, explaining the color change observed experimentally[13]. Although these structural transitions do not mean a significant change in powder diffraction (Figure 3.7a, pink line). The PDF data collected on the **CP1-3H$_2$O** sample after heating at 135 °C show that the local structure of **CP1** remains unaltered (Figure 3.9b), whereas major changes are observed at the long-range scale. This result is also in agreement with the structural transition determined by PXRD (Figure 3.7a, orange line).

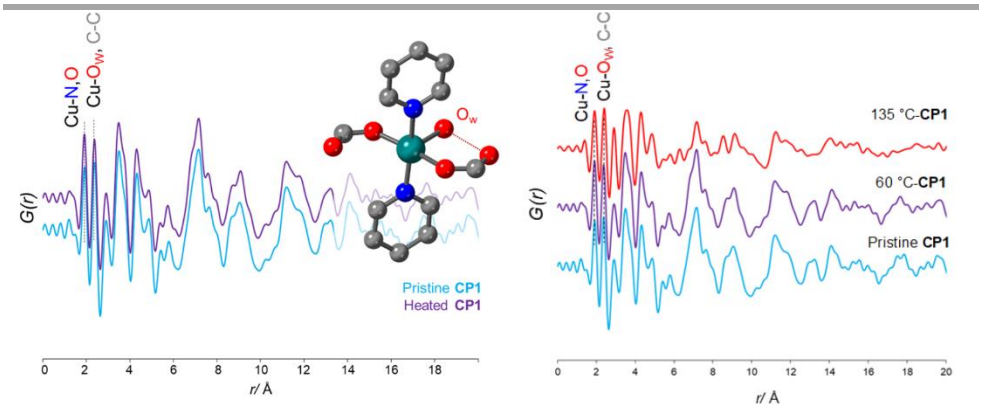

Figure 3.9. Experimental PDFs for **CP1** (pristine), **CP1-H$_2$O** and **CP1-3H$_2$O** (heated) samples before and after heating at 60 °C (a) and 135 °C (b), indicating the two peaks linked to the binding of the 4,4'-bipy and TAcO ligands (≈ 2.0 Å) and the water molecule (≈ 2.3 Å). The dash line in the structure indicates hydrogen bonding between the water molecules and one oxygen atom of the TAcO ligands.

After the exhaustive structural study of **CP1**, the crucial role of water molecules (coordination and solvation) has been determined, making the coordination polymer a promising candidate as a humidity sensor. To evaluate the behavior of the compound for the detection of low quantities of water an study with dry solvents was carried out.

First of all, it is essential to evaluate the behavior of **CP1** with the organic solvents that will be used later. Then, **CP1** was soaked in diverse dry organic solvents: EtOH (99.5 %), MeOH (99.9 %), CH_3CN (99.8 %), and THF (99.9 %) (Figure 3.10). In all cases, the coordination polymer changes from blue to violet in a time range from 1 to 15 min, being the fastest change of color (about 1 min) when **CP1** is soaked in dry EtOH or MeOH. This change was followed in the case of MeOH by PXRD and diffuse reflectance spectroscopy (Figure A3.6, A3.7 and Table 3.1 page 193-194), which confirm a structural change again. In this case, no crystal structure suitable to be solved by SXRD was obtained but it is not far-fetched to assume that a ligand exchange is produced between the copper-coordinated water molecule and the MeOH. This process is reversible when the organic solvent is evaporated in air and the presence of ambient water molecules turns the compound back into **CP1** in less than 2 min. The reversibility was tested successfully in all dry organic solvents.

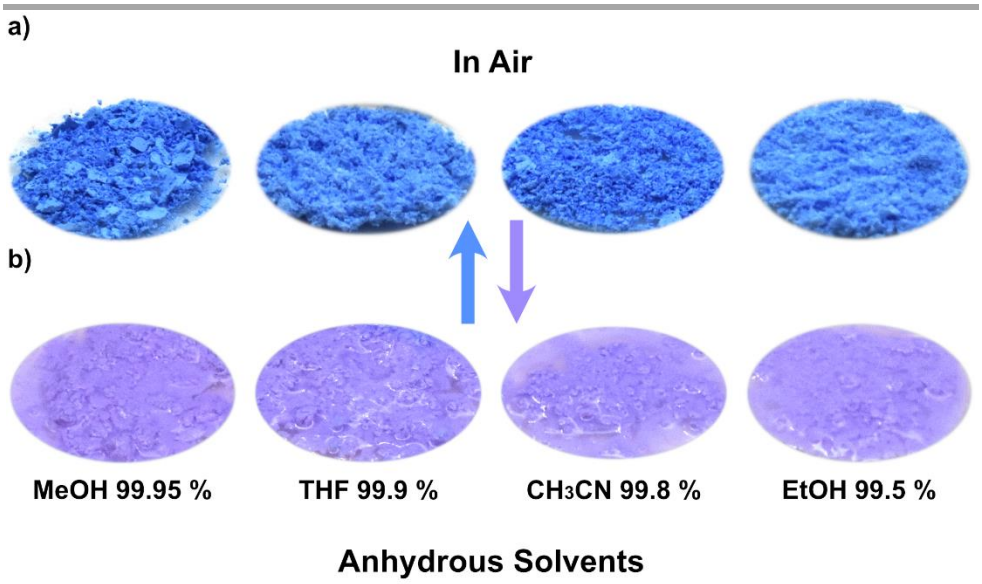

Figure 3.10. Photographs of a) **CP1** in air and b) **CP1** after soaking for 1-5 min in different dry organic solvents.

Therefore, **CP1** shows a solvatochromic behavior, likely due to the water molecule weakly bonded to the metal center, which favors the approach of the solvent molecules to the coordination sphere. This fact enables to evaluate the detection capacity of the coordination polymer in two different ways. On the one hand, a well-known volume of each one of the organic almost dry solvents (ethanol 99.5 %, methanol 99.95 %, tetrahydrofuran 99.9 %, and acetonitrile 99.8 %) was added over an also known amount of **CP1** and when the coordination polymer changed its color to violet, small volumes (≈ 5 µL) of water were added over the sample until the compound changed its color to blue again. On the other hand, a similar procedure was used but starting from **CP1-H_2O**, the violet material previously treated to lose the coordination water molecule. In this

case, an excess volume of the organic solvents was added over **CP1-H_2O** to assure that the solvent coordinates to the metal center. Obviously, in this step no color change was observed after adding the solvents, but when the small volumes of water were added over the compound, the change of color to blue (**CP1**) was observed. In both cases, the limit of detection (LOD) was calculated in percentage and the results (Table 3.1) show that **CP1** is more sensitive to water than **CP1-H_2O.**

Table 3.1. Data obtained from the water detection limits of **CP1**, **CP1-H_2O** and **CP1@3D** in the presence of different dry solvents.

Solvent	**MeOH 99.95 %**	**EtOH 99.5%**	**THF 99.9 %**	**CH_3CN 99.8 %**
Solvent aliquot [mL]	2	2	5	5
CP1 weight [g]	0.0040	0.0036	0.0097	0.0043
Water volume added [mL]	0.085	0.02	0.01	0.01
CP1 LOD [%]	4.7	1.7	0.3	0.4
CP1-H_2O weight [g]	0.0086	0.0084	0.0082	0.0085
Water volume added [mL]	0.11	0.05	0.02	0.02
CP1-H_2O LOD [%]	6.0	3.2	0.5	0.7
CP1@3D weight [g]	0.0098	0.0084	0.0084	0.0118
Water volume added [mL]	0.085	0.01	0.015	0.01
CP1@3D LOD [%]	4.8	1.0	0.4	0.4

In order to compare the results obtained for the bulk material with the 3D composite material, the same experiments in dry solvents were carried out with **CP1@3D**. The behavior of **CP1@3D** is similar in

all solvents to that of the bulk material, showing a change of color from blue to violet when it is soaked (Figure 3.11) and the LOD data obtained exhibit an equal detection capacity, but with the advantage of using a tailorable material that may be incorporate in a device.

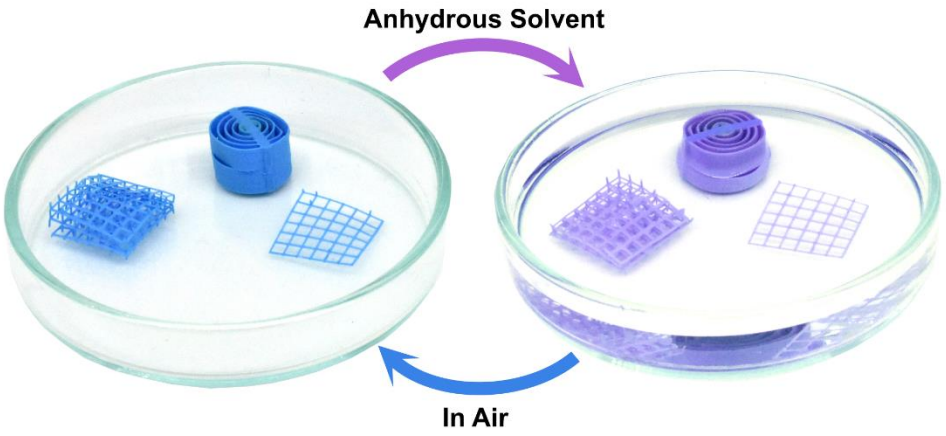

Figure 3.11. Different architectures of the 3D printed material **CP1@3D** in air at RT showing blue color (left). **CP1@3D** introduced in dry solvents such as ethanol, methanol, tetrahydrofuran, or acetonitrile showing the characteristic violet color (right).

3.3. Conclusions

This work tries to highlight the importance of combining and adapting the use of new technologies to well-known materials. In this case, a previously studied coordination polymer (**CP1**), which is easily obtained as a colloid in water at room temperature and can be prepared at a large scale in the lab. Therefore, **CP1** was turned into a good candidate as ink for 3D printing and although was not able to be printed pure, a new composite material with 40 wt% of **CP1** embedded in its matrix was obtained.

Despite of the fact that the structure of **CP1** had been studied before, this time it is the water molecules that play the main role. A detailed study of the crystal structure has showed that their loss with temperature or vacuum or their exchange with organic solvents results in a thermochromic or solvatochromic behavior of **CP1**, respectively. Therefore, **CP1** is a versatile material that can be tailored and manufacture in different constructions by 3D printing and used as a humidity sensor.

3.4. References

1. Bos, F., Wolfs, R., Ahmed, Z. & Salet, T. Additive manufacturing of concrete in construction: potentials and challenges of 3D concrete printing. *Virtual Phys. Prototyp.* **11**, 209–225 (2016).

2. Sun, J., Zhou, W., Huang, D., Fuh, J. Y. H. & Hong, G. S. An Overview of 3D Printing Technologies for Food Fabrication. *Food Bioprocess Technol.* **8**, 1605–1615 (2015).

3. Murphy, S. V. & Atala, A. 3D bioprinting of tissues and organs. *Nat. Biotechnol.* **32**, 773–785 (2014).

4. Mahadevan, M., Francis, A. & Thomas, A. A simulation-based investigation of sustainability aspects of 3D printed structures. *J. Build. Eng.* **32**, 101735 (2020).

5. Layani, M., Wang, X. & Magdassi, S. Novel Materials for 3D Printing by Photopolymerization. *Adv. Mater.* **1706344**, 1706344 (2018).

6. Choong, Y. Y. C. *et al.* The global rise of 3D printing during the COVID-19 pandemic. *Nat. Rev. Mater.* **5**, 637–639 (2020).

7. Valentine, A. D. *et al.* Hybrid 3D Printing of Soft Electronics. *Adv. Mater.* **29**, 1–8 (2017).

8. Noor, N. *et al.* 3D Printing of Personalized Thick and Perfusable Cardiac Patches and Hearts. *Adv. Sci.* **6**, 1900344 (2019).

9. Wan, M. *et al.* Biocompatible heterogeneous bone incorporated with polymeric biocomposites for human bone repair by <scp>3D</scp> printing technology. *J. Appl. Polym. Sci.* **138**, 50114 (2021).

10. Näther, C., Greve, J. & Jeβ, I. New Coordination Polymer

Changing Its Color upon Reversible Deintercalation and Reintercalation of Water: Synthesis, Structure, and Properties of Poly[Diaqua-(μ 2 -Squarato- O , O ‘)-(μ 2 -4,4‘-Bipyridine- N , N ‘)- Manganese(II)] Trihydrate. *Chem. Mater.* **14**, 4536–4542 (2002).

11. Henkelman, G., Uberuaga, B. P. & Jónsson, H. A climbing image nudged elastic band method for finding saddle points and minimum energy paths. *J. Chem. Phys.* **113**, 9901–9904 (2000).

12. Platero-Prats, A. E. *et al.* Structural Transitions of the Metal-Oxide Nodes within Metal–Organic Frameworks: On the Local Structures of NU-1000 and UiO-66. *J. Am. Chem. Soc.* **138**, 4178–4185 (2016).

13. Amiri, M. G. & Golchoubian, H. Solvatochromism, thermochromism and density functional theory studies of Copper(II) complexes containing hemilabile tetradentate ligand. *J. Mol. Struct.* **1165**, 196–205 (2018).

CHAPTER 4. RATIONAL DESIGN OF NANOSCALE COORDINATION POLYMER BASED ON Cu(II) AND URACIL DERIVATIVES TO IMPROVE THEIR CYTOTOXIC ACTIVITY

4.1. Introduction

The synthesis of nanostructured coordination polymers is a recent development that opens the door to introduce these multifunctional materials in a whole new world of potential applications. Being capable of controlling the size of coordination polymers is a powerful tool which makes possible to tune the compound size to the application needs. Among the different uses of coordination polymers, biological applications are one of the preferred choices. Especially, porous coordination polymers or MOFs are used as carriers for drug delivery[1]. The well-defined pores of these materials and the presence of functional groups enable to load diverse treatments ranging from anti-inflammatory drugs[2] to chemotherapeutic agents[3]. However the use of 2D or 1D coordination polymers for drug delivery is not so extended, although there are a

few examples[4] in which the use of interactions such as hydrogen bonds are employed to load the drug in the supramolecular structure. A coordination polymer is always thought as a vehicle or platform to load the therapy agent of interest, however thanks to the wide variety of biocompatible molecules that can be chosen as ligands, coordination polymers can be part of the therapy[5].

One of the most studied anticancer agents is 5-fluorouracil (5-FU), which has showed effectiveness in several cancers such as breast, colon, pancreas or neck over the years[6,7]. 5-FU act as antimetabolite, impeding nucleoside metabolism, and thanks to its analogue structure of uracil, can be combined with DNA and RNA, leading to cell death[8]. However, like other chemotherapies, 5-FU needs to improve its short biological half-life, the negative side effects or the poor oral absorption[9,10]. To find a solution to these problems, there are two different strategies. On the one hand, designing new materials where 5-FU can be encapsulated and released in the target, avoiding the use of higher doses of drug[11]. Another strategy considers employing derivatives of 5-FU, which maintain the properties, but are less toxic, such 5-fluorouracil-1-acetic acid[12].

This chapter presents a new coordination polymer using 5-fluorouracil-1-acetic acid (5-FUAcOH) a derivate of 5-FU as ligand and compares its antitumor effect with an analogue coordination

polymer, whose ligand is only the uracil derivative uracil-1-acetic acid (UAcOH).

4.2. Results and Discussion

In order to compare the effect of using a drug as ligand, two new coordination polymers have been synthesized. One polymer using uracil-1-acetic acid (UAcOH) as ligand, again a nucleobase functionalized with a carboxylic acid to make the coordination to the metal ion easier and set the nucleobase moiety free. The other one has been prepared with the anticancer agent 5-fluorouracil (5-FU)[13,14], but to obtain analogous coordination polymers, the derivative functionalized with a carboxylic acid was used, 5-fluorouracil-1-acetic acid (5-FUAcOH). To complete the coordination polymers, copper(II) is selected as metallic ion because of its biocompatibility and the possibility to provide magnetic and conductive properties[15]. Finally, to act as bridge between metal centers and to contribute with its aromaticity to the conductivity, the neutral ligand 4,4'-bipyridine is chosen[16].

Obtaining single crystals of the coordination polymers is the first step in elucidating the structure, so two identical hydrothermal reactions between a copper(II) salt, 4,4'-bipyridine and a biocompatible ligand were prepared. UAcOH leads to **CP2** and changing the modified nucleobase by 5-FUAcOH leads to **CP3** (Figure 4.1).

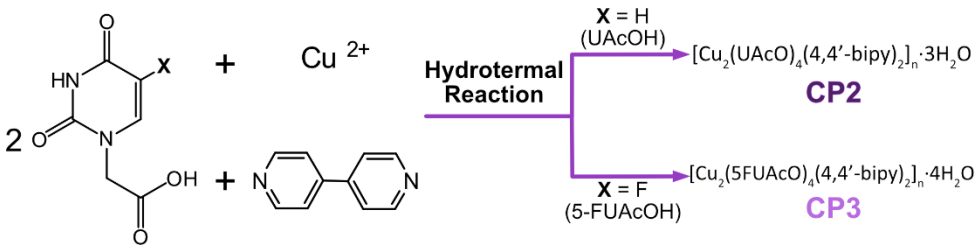

Figure 4.1. Scheme of the synthesis of crystals of **CP2** and **CP3**.

The structure of **CP2** and **CP3** was determined from the single crystals by SCRXD (section A4.2.5, pages 198-202). The crystal structure of **CP2,** with formula **$[Cu_2(UAcO)_4(4,4'\text{-bipy})_2]_n \cdot 3H_2O$**, consists of a 1D ladder-like structure. In one direction, the copper(II) metal centers are bridged by two 4,4'-bipyridine ligands forming the polymeric chain. In the other direction, the two chains are bridged at the metal centers by two carboxylate oxygen atoms from two uracil-1-acetate ligands (Figure 4.2a). The coordination sphere of the copper(II) metal center adopts a square pyramid geometry. The basal plane is occupied by two nitrogen atoms from two 4,4'-bipyridine ligands in trans arrangement and by two oxygen atoms, one from a bridging carboxylate and one from a terminal uracil-1-acetate. The apical position is occupied by an oxygen atom from the other bridging carboxylate (Figure 4.2b). The supramolecular 3D structure is sustained in one direction by π-π stacking between terminal uracil-1-acetate ligands and in the other direction by hydrogen bonds between bridging uracil-1-acetate ligands (Figure 4.2c-e).

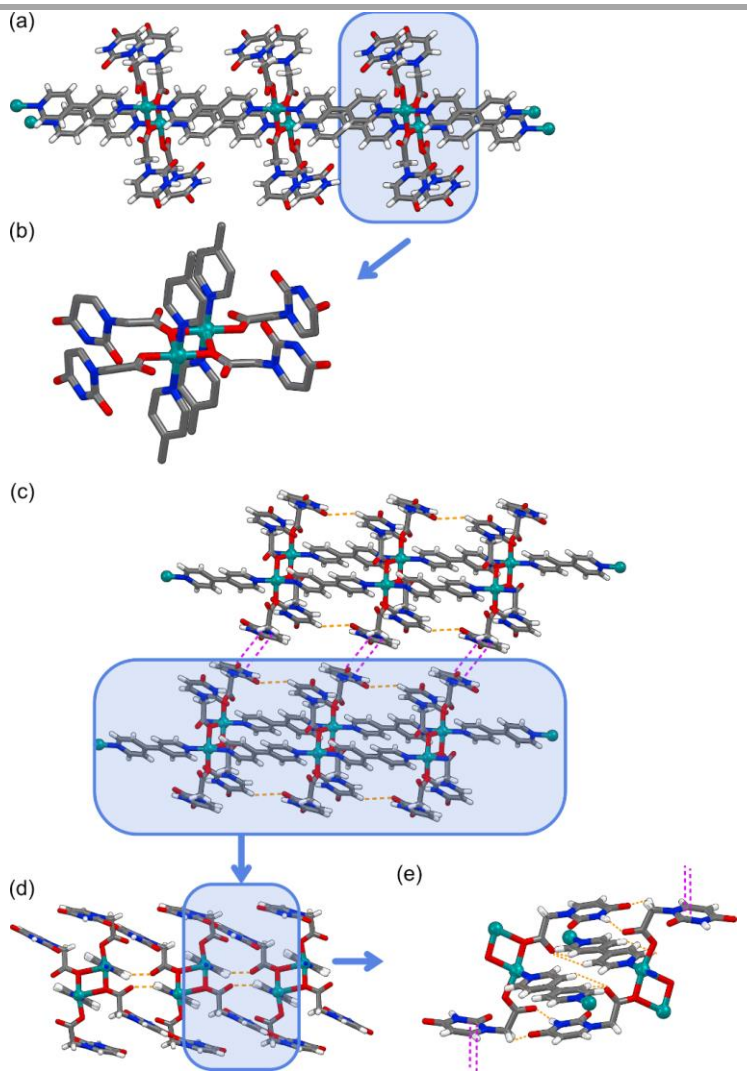

Figure 4.2. (a and b) Ladder like coordination polymer **CP2** and magnification of the metal coordination surrounding. c) Projection of the crystal packing of **CP2** along the crystallographic b axis emphasizing the presence of supramolecular sheets held together by π-π stacking interactions. (d-e) Assembly of the polymeric 1D chains through hydrogen bonding interactions. Orange single dashed lines indicate hydrogen-bonding interactions, and purple double dashed lines π-π stacking interactions. The disorder of the uracil residue has been omitted for clarity.

CP3 presents a very similar 1D ladder-like metal-organic molecular structure with formula **$[Cu_2(FUAcO)_4(4,4'\text{-bipy})_2]_n \cdot 4H_2O$** . Again, the metal centre is bridged by two 4,4'-bipyridine ligands and two carboxylate oxygen atoms from two fluorouracil-1-acetate ligands, which define the side rail and the rung of the ladder chain (Figure 4.3a). The coordination sphere includes a terminally coordinated 5-fluorouracil-1-acetate ligand to provide an elongated square pyramidal geometry around the metal centre. The apical position is occupied by the oxygen atom of the bridging 5-fluorouracil-1-acetate ligand (Figure 4.3b). As it can be seen, the molecular features of **CP2** and **CP3** are almost identical. Still, the monodentate 5-fluorouracil-acetate ligands establish supramolecular interactions slightly different than the uracil residues. In fact, the 5-fluorouracil residues establish the complementary hydrogen-bonds expected between nucleobases more efficiently with the 5-fluorouracil-acetate terminal ligands from the adjacent chains. Simultaneously, the bridging 5-fluorouracil-acetate ligands establish π-π interactions with the bridging 5-fluorouracil-acetate ligands from adjacent chains, which reinforce the supramolecular interactions. The presence of both supramolecular interactions simultaneously (H-bonding and π-π interactions; Figure 4.3c-e) provides a strong synthon connecting the ladder-like chains and resembles a modest analogue of the nucleobases structural role in DNA.

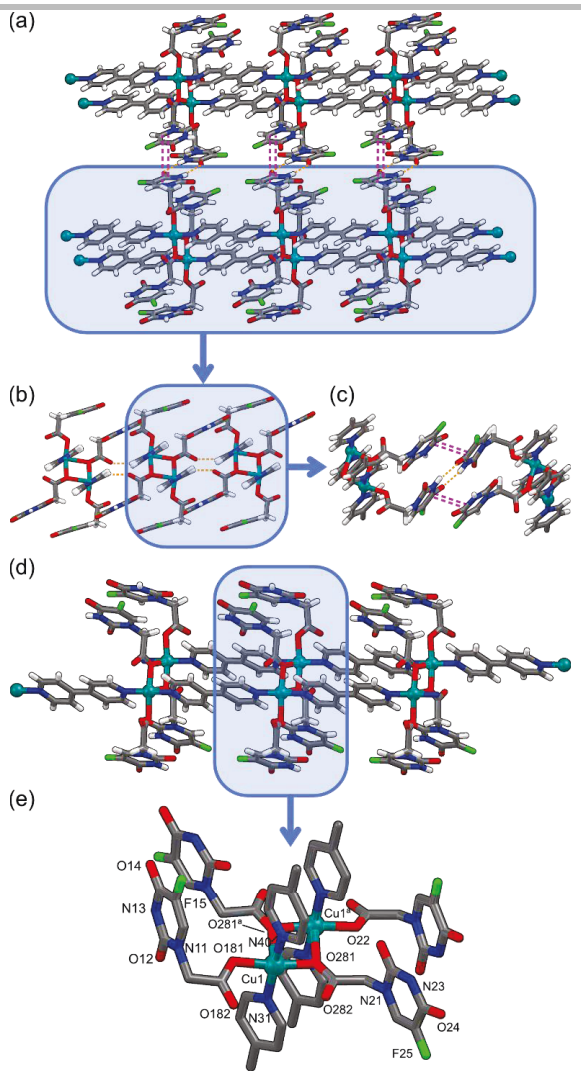

Figure 4.3. (a) Projection of the crystal packing of **CP3** along the crystallographic [110] direction emphasizing the most relevant supramolecular interactions taking place. (b and c) Assembly of the polymeric 1D chains through hydrogen bonding interactions. (d and e) Ladder like coordination polymer and magnification of the metal coordination surrounding with the labelling scheme. Orange single dashed lines indicate hydrogen bonding interactions and purple double dashed lines π-π stacking interactions. The disorder of the 4,4'-bipy ligand has been omitted for clarity.

As shown in Chapter2, coordination polymers can be obtained at the nanoscale in a simple reaction in mild conditions. Nanoscale CP2 (**CP2n**) and CP3 (**CP3n**) were prepared by decreasing the temperature to 5 °C in a direct reaction between the building blocks, whose result is a purple colloid (Figure 4.4).

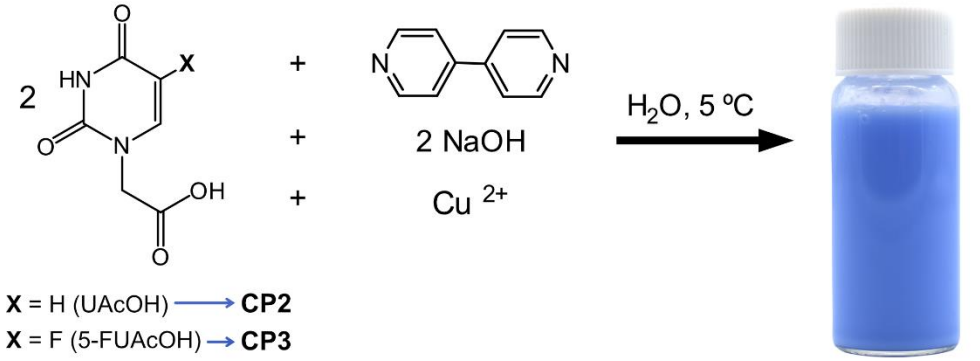

Figure 4.4. Representation of the synthesis of $[Cu_2(UAcO)_4(4,4'\text{-bipy})_2]_n \cdot 3H_2O$ (**CP2n**) and $[Cu_2(5\text{-FUAcO})_4(4,4'\text{-bipy})_2]_n \cdot 4H_2O$ (**CP3n**) as a water colloid.

Both nanoscale coordination polymers are characterized by PXRD, which confirmed that the obtained compounds match with the crystal structure (Figure 4.5a-c). Also, an ATR-FT-IR and an elemental analysis were performed, which corroborate the presence of C=O bonds from the carboxylate of the uracil derivative ligands and C=N bonds from the 4,4'-bipyridine ligands (Figure 4.5b-d) and the composition of the materials (section A42.2.2, page 196 and section A4.2.4, page 198), respectively.

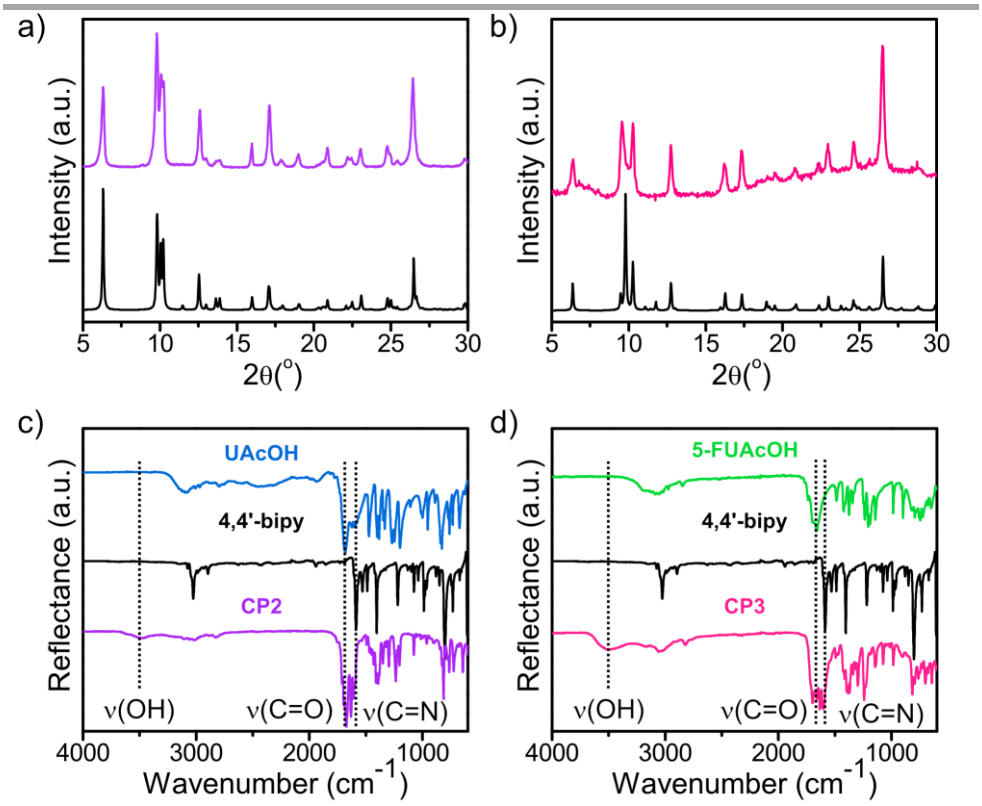

Figure 4.5. a-b) PXRD pattern and ATR-FT-IR spectra of **CP2n** (purple) and simulated (black). c-d) PXRD pattern and ATR-FT-IR spectra of **CP3n** (pink) and simulated (black).

Once it has been confirmed that **CP2n** and **CP3n** are the expected coordination polymers, the characterization is completed with microscopy techniques to know the size and the morphology. SEM and AFM images of **CP2n** show a well-defined nanoplate morphology with an average size around 150 nm wide, 320 nm long and thickness between 20 to 40 nm (Figure 4.6a-b). On the other hand, SEM and AFM images of **CP3n** show an irregular nanoplate structure about 284

nm wide, 345 nm long and thickness between 40 to 60 nm (Figure 4.6cd).

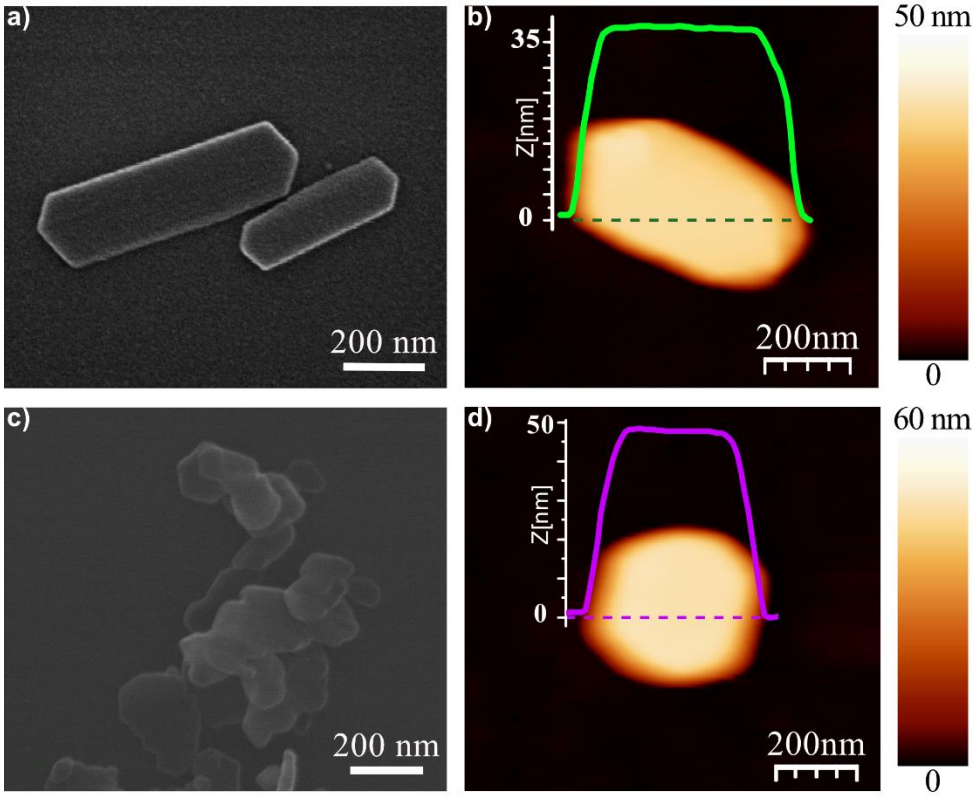

Figure 4.6. (a) FESEM image and (b) AFM topographic image with height profile along the blue dashed line of nanoplate from **CP2n** sample and (c) FESEM image and (d) AFM topographic image with height profile along the green dashed line of nanoplate from **CP3n** sample.

With the aim of using **CP2n** and **CP3n** in biological applications, the stability of both coordination polymers was studied at different times and pH values and also in DMEM and RPMI, the cell culture media that would be needed for the next step, studies in cells. First, it was

checked that both materials are stables for long times, so the colloid samples of **CP2n** and **CP3n** freshly prepared were stored for one month at room temperature. To confirm that after this time they continued to be the same compound, the structure and morphology were characterized by SEM, PXRD and IR (Figure 4.7 and 4.8). In both cases, PXRD and IR verified that the crystalline structure is maintained, and the SEM images do not show any modification in the morphology.

CP2n and **CP3n** colloids have a pH around 5.7, so it was modified in the range of biological pH[17]. The pH of both coordination polymers was adjusted to pH = 4 by addition of aqueous solution of HCl (0.01 M) and to pH = 7 by addition of aqueous solution of NaOH (0.01 M). The characterization of the samples by PXRD, IR and SEM shows that at pH < 6 **CP2n** and **CP3n** are stable, but at pH > 6 the polymers start to change slightly their structure and their morphology (Figure 4.9 and 4.10).

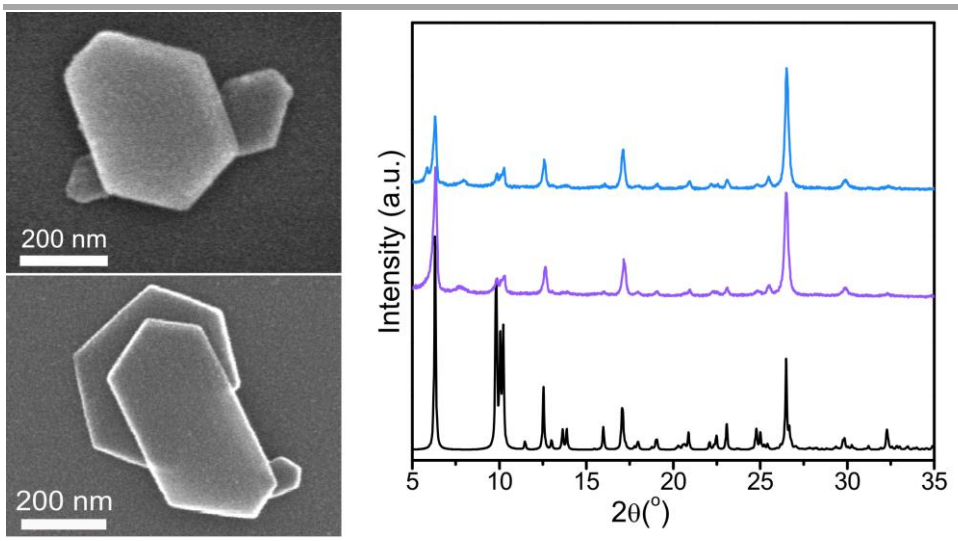

Figure 4.7. FESEM images and PXRD patterns of **CP2n** sample (5°C, H_2O, pH= 5.7) freshly prepared (down, purple), the same sample after one month (up, blue) and simulated data (black line).

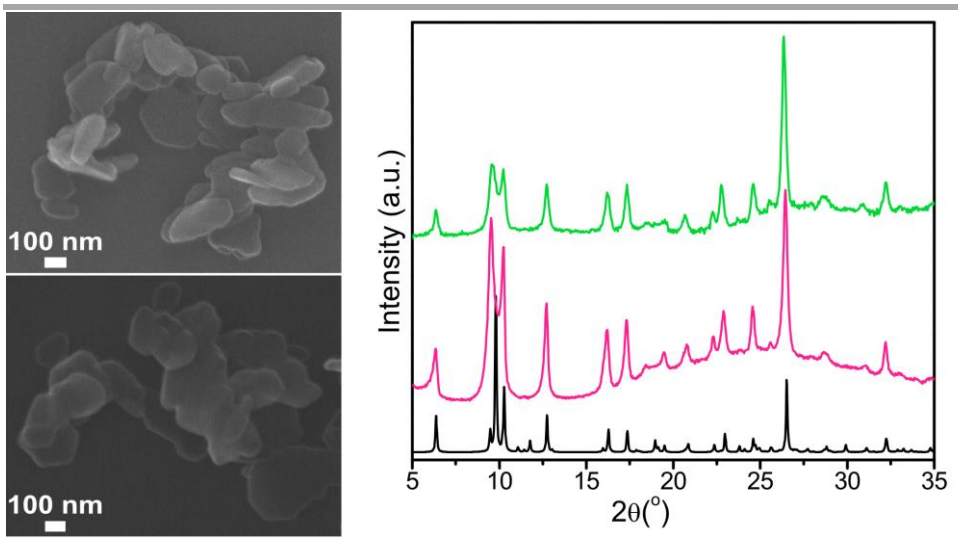

Figure 4.8. FESEM images and PXRD patterns of **CP3n** sample (5°C, H_2O, pH= 5.65) freshly prepared (down, pink), the same sample after one month (up,green) and simulated data (black line).

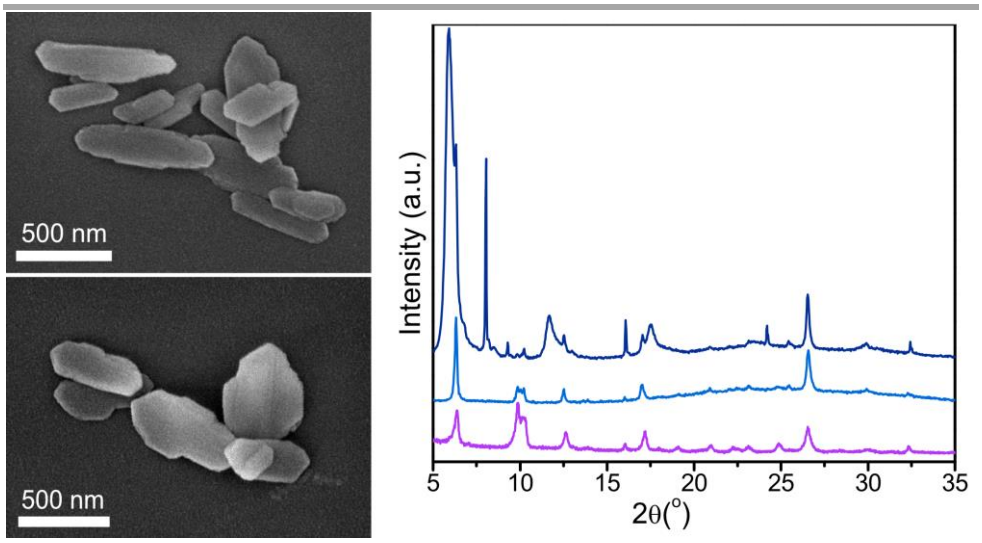

Figure 4.9. FESEM images of **CP2n** sample prepared at pH= 4 (up) and pH=7 (down). PXRD patterns of **CP2n** (pH ~ 5.7 purple line) and **CP2n** after modified the pH at pH = 4 (light blue line) and pH = 7 (deep blue line).

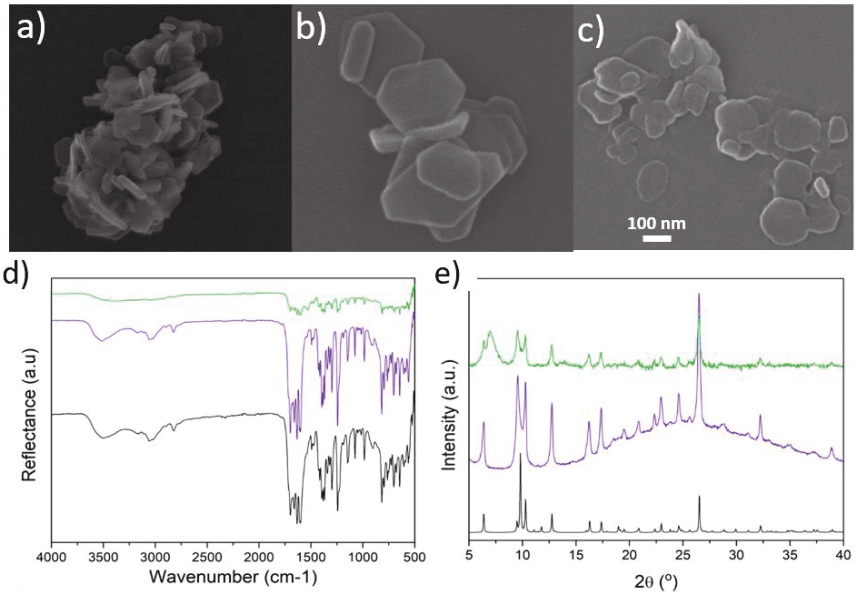

Figure 4.10. FESEM images of a) **CP3n** sample prepared following the synthetic procedure (5ºC, H_2O, pH= 5.7) and the same sample at b) pH= 4 and c) pH=7. d) ATR-FT-IR spectra and e) PXRD patterns of **CP3n** (pH ~ 5.7 black line) and **CP3n** after modified the pH at pH = 4 (red line) and pH = 7 (blue line). pH adjusted upon addition of HCl 0.01 M and NaOH 0.01 M respectively.

Once the stability of **CP2n** and **CP3n** at different conditions is known, it is time to study their behaviour in the cell culture media: DMEM and RPMI. The cell culture media are supplemented with 10 % (v/v) foetal bovine serum (FBS), 2 mM L-Glutamine, and 1 % Penicillin/Streptomycin (named *serum-supplemented medium* from this point onwards) like the media that will be used in the cell studies. First, it was observed what happened when **CP2n** and **CP3n** were mixed with the serum-supplemented medium (100 µL of nanoscale coordination polymer in 900 µL of culture media) at room

temperature. A blank sample using just water instead of the serum-supplemented medium was also studied. In a few seconds, the initial polymers are dissolved in the media, but not in water. The three samples were studied at different times, so at times between 1 minute to 1 hour they were centrifuged without the appearance of any solid, but 48 h later a light green solid appears in the **CP2n** sample. The solid was characterized by PXRD as the complex $[Cu(UAcO)_2(H_2O)_4]\cdot 2H_2O$ (**Cu(II)-Complex**) (Figure A4.1, page 205). To study this behaviour of **CP2n** and **CP3n** in the serum-supplemented media, the amount of copper ions was measured in serum-supplemented media and in water at different reaction times (5 min, 15 min, 1 h, 24 h, and 48 h) by ICP-MS using same ratio polymer:medium mentioned above (Table 4.1). This experiment shows that both coordination polymers have a similar behaviour in water and in supplemented media. In all cases, the amount of copper(II) released is maintained without significant variations between 5 min to 48 h. However, there is less amount of copper(II) released in the media than in water, which suggests the interaction of Cu(II) with some of the components of the media (amino acids, vitamins or salts) forming new species.

Table 4.1. ICP-MS measurements of **CP2n** and **CP3n** in water and culture media with the time at room temperature.

Coordination Polymer	Time	Concentration of Copper (mg/L)		
		H_2O	DMEM	RPMI
CP2n	5 min	29.20	20.09	21.29
	15 min	28.43	20.94	20.78
	1 h	28.62	22.36	28.49
	24 h	31.77	21.99	21.26
	48 h	31.24	20.65	22.25
CP3n	5 min	44.89	31.43	34.59
	15 min	42.66	31.68	31.64
	1 h	41.70	34.37	33.58
	24 h	37.05	31.62	31.59
	48 h	37.47	32.10	32.49

The culture media used in these studies are supplemented, so trying to discard the interaction of supplements with the coordination polymers, the media and the supplements were studied separately. The behaviour of **CP2n** and **CP3n** was evaluated in the serum-free DMEM and RPMI and in each one of the supplements (10 % (v/v) foetal bovine serum (FBS), 2 mM L-Glutamine, and 1 % Penicillin/Streptomycin). The results show that **CP2n** and **CP3n** are dissolved in the serum-free media, but there are no interactions with any supplement.

Studying what happens in the culture media is difficult because they are complex matrices with many components. Even though a

complete characterization of the species formed in the media is not possible, a cyclic voltammetry can be carried out to determine any change in the oxidation state of copper. The cyclic voltammetry study of **CP2n** and **CP3n** in DMEM and in RPMI shows the reduction of Cu(II) (Figure 4.12). This reduction takes place in two steps, the first one is quasi-reversible, at -1.25 V *vs*. Ag/AgCl, and the second one is completely irreversible, at *ca*. -1.42 V *vs*. Ag/AgCl. When the potential sweep covers the second component, the reoxidation of the first peak is lost, and a sharp, small, oxidation peak appears at *ca*. -1.2 V which can be due to a species adsorbed on the electrode. This peak is slightly bigger for **CP2n** than **CP3n**. Further oxidation of reduction products is observed at a much more positive potential (*ca.* -0.2 V).

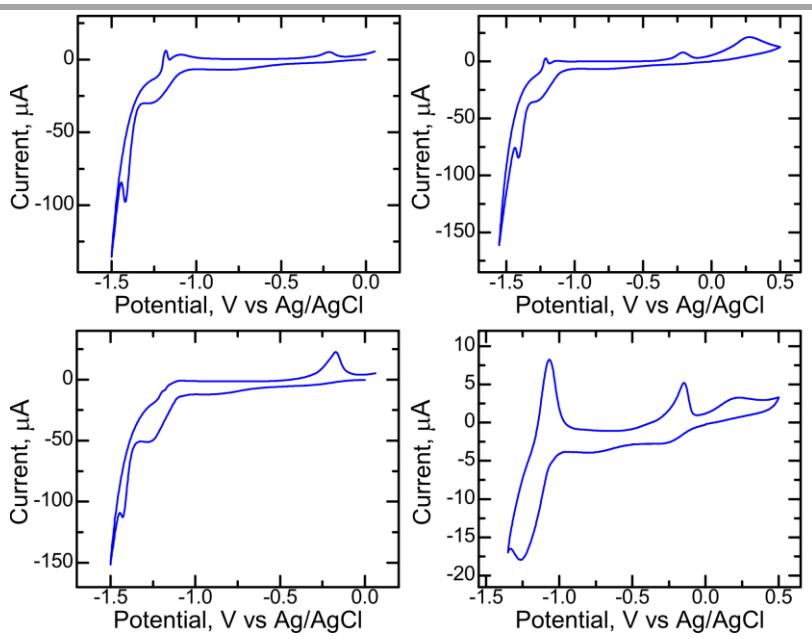

Figure 4.12. Cyclic voltammetry at 0.1 V/s of a **CP2n** (up) and **CP3n** (down) in DMEM and RPMI, respectively.

Knowing the stability and the behaviour of **CP2n** and **CP3n** in the cell culture media DMEM and RPMI, an exhaustive study of cell viability was carried out.(section A4.2.9 and A4.2.10, pages 203-205) The viability of two cancer cell lines, human uveal melanoma (Mel202) and human pancreatic adenocarcinoma (Panc-1), was studied with **CP2n**, **CP3n**, the building blocks of each polymer (uracil-1-acetic acid, 5-fluorouracil-1-acetic acid, $Cu(ACO)_2$ and 4,4'- bipyridine) and the **Cu(II)-Complex.** First, the cells were exposed to Cu(II) salt ($Cu(CH_3COO)_2 \cdot H_2O$), 4,4'-bipyridine and UAcOH, and it was confirmed that each component of the polymer have no toxicity separately (Figure 4.13).

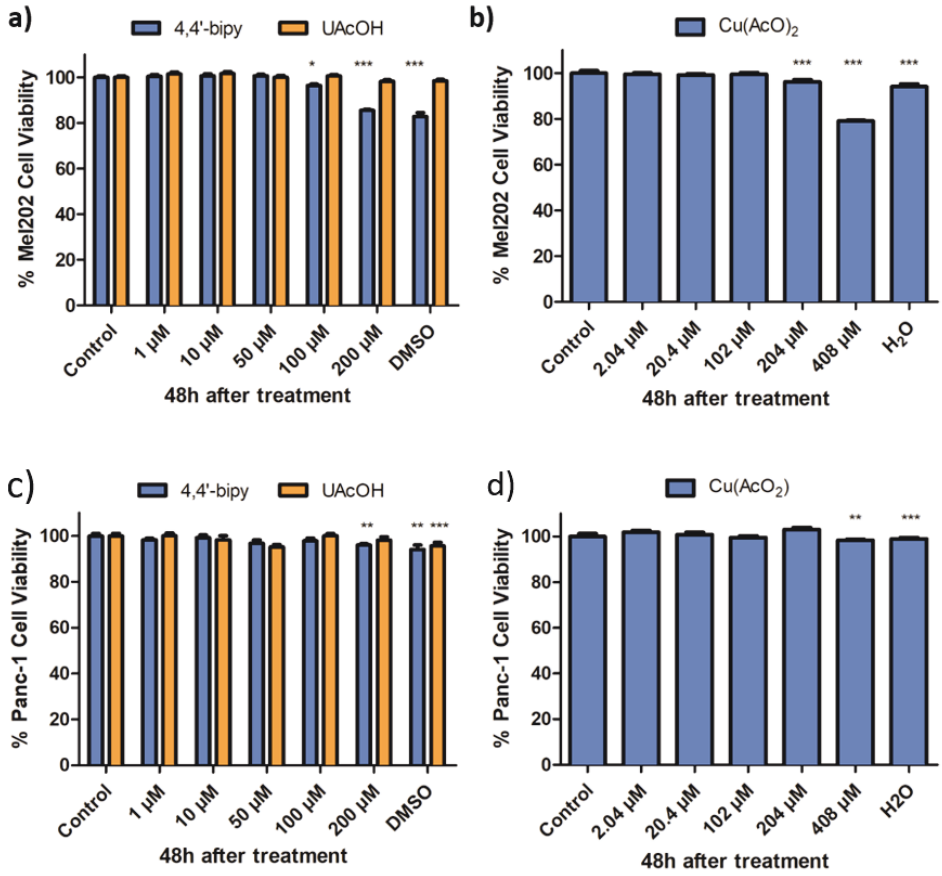

Figure 4.13. Surviving fraction of a-b) Uveal Melanoma (Mel202) and c-d) Pancreatic Cancer (Panc-1) cells 48 hours after the treatment with a) 4,4' bipyridine and uracil acetate at concentration from 1 to 200 µM b) copper salt acetate at concentration from 2.04 to 408 µM. Data correspond to mean ± SD. Statistical analysis was performed using one-way ANOVA Tukey's test (each group vs Control). *P<0.01, **P<0.001, and ***P<0.0001.

Then, the cell viability of the ligand 5-FUAcOH and the anticancer agent 5-FU was compared. The results revealed that 5-FU is twice as toxic as 5-FUAcOH (40% and 80% of viability respectively) (Figure 4.14).

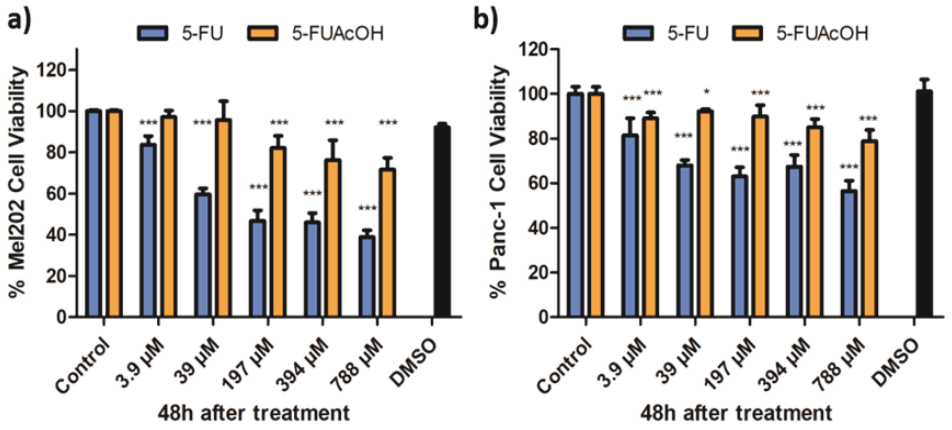

Figure 4.14. Surviving fraction of **a)** Uveal Melanoma (Mel202) and **b)** Pancreatic Cancer (Panc-1) cells 48 hours after the treatment with 5-FU and 5-FUAcOH at the equivalent concentrations present in CP2n and CP3n. Data correspond to mean ± SD. Statistical analysis was performed using one-way ANOVA Tukey's test (each group vs Control). *P<0.01, **P<0.001, and ***P<0.0001.

Although the ligand 5-FUAcOH is not very toxic, when **CP2n** and **CP3n** were incubated in cells, **CP3n** was found to be almost three times as toxic as **CP2n** (around 35 % and 83 % of viability respectively). In this study the **Cu(II)-Complex** was also evaluated and the results show that it is not toxic (Figure 4.15a-b). Considering these results, an additional study of reactive oxygen species (ROS) was done for **CP2n**, **CP3n** and **Cu(II)-Complex** (Figure 4.15c-d).

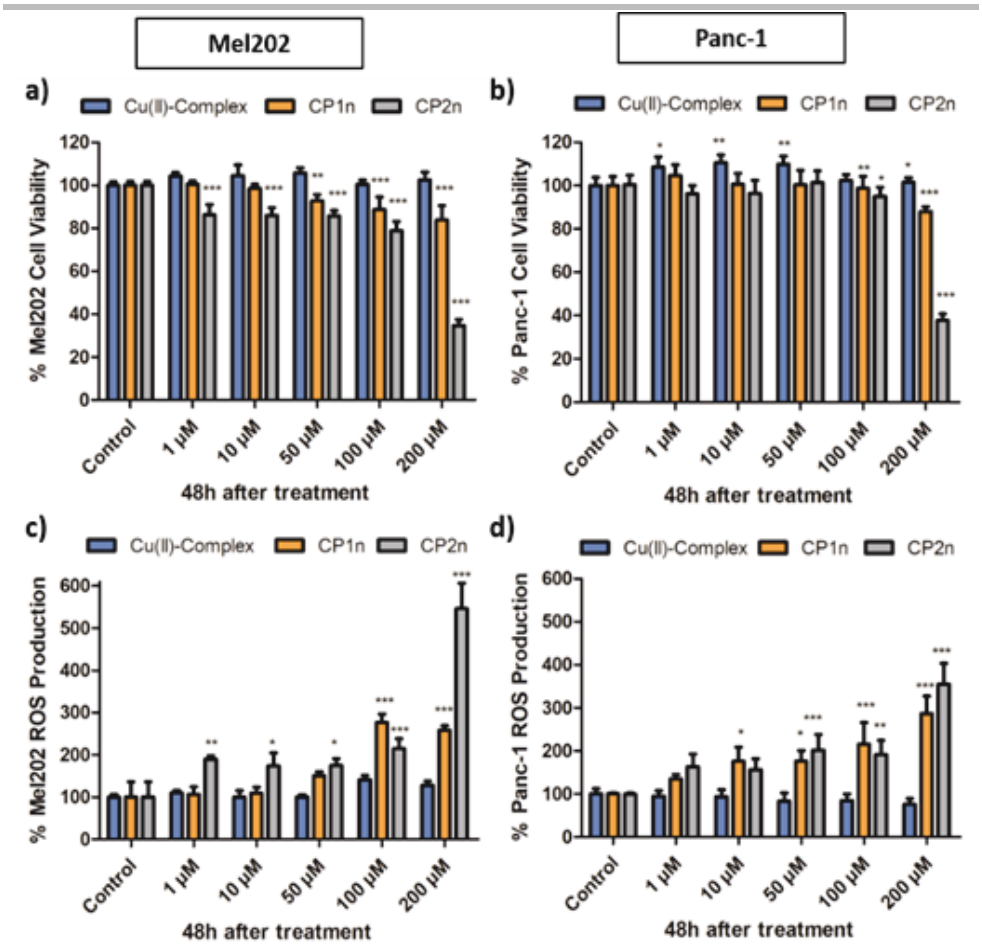

Figure 4.15. Cell viability and ROS production studies on (a, c) Mel202 and (b, d) Panc-1 cells at 48 hours after treatment with different concentrations (1-200 µM) of Cu(II)-complex (blue), CP2n (orange) and CP3n (grey). Statistical analysis was performed using one-way ANOVA Tukey's test (each group vs control). *P<0.01, **P<0.001, and ***P<0.0001.

This study corroborates that **Cu(II)-Complex** has similar toxicity values to the control, so it does not participate in the generation of ROS. However, the behaviour of **CP2n** and **CP3n** in the cell culture

media and the cyclic voltammetry results coincide with the gradual increase of ROS with concentration, being bigger for **CP3n** because of the presence of the ligand 5-FUAcOH. To check that the results obtained with **CP3n** were due to the coordination of the ligand 5-FUAcO to the cooper ion and not only to the ligand, **CP2n** with 5-FU and **CP2n** with 5-FUAcOH were incubated in cells. In this case, toxicity only corresponds to ligands individually (Figure 4.16).

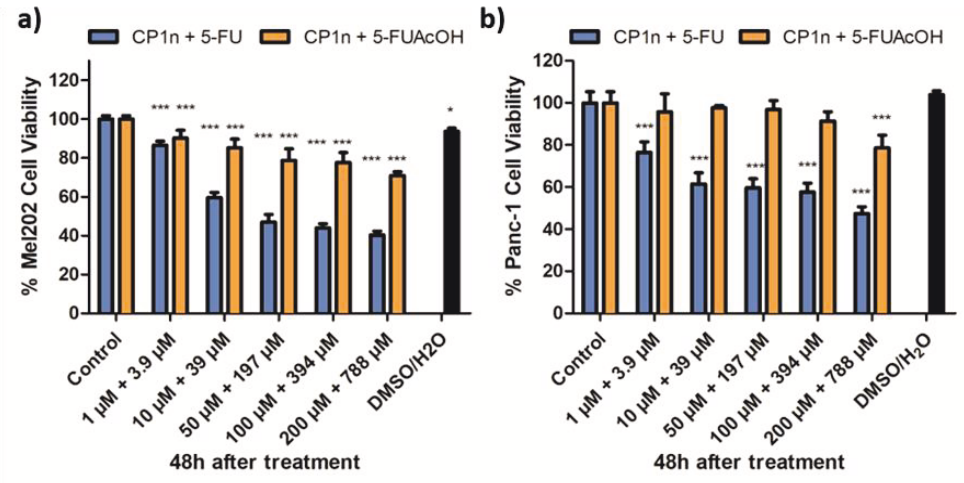

Figure 4.16. Surviving fraction of **a)** Uveal Melanoma (Mel202) and **b)** Pancreatic Cancer (Panc-1) cells 48 hours after the treatment with a combination of **CP2n** + 5-FU and **CP2n** + 5-FUAcOH. Data correspond to mean ± SD. Statistical analysis was performed using one-way ANOVA Tukey's test (each group vs Control). *P<0.01, **P<0.001, and ***P<0.0001.

The differences observed between cytotoxic studies of 5-FUAcOH, the anticancer drug 5-FU and **CP3n** are attributed to the different solubility. 5-FU is more toxic than 5-FUAcOH because in physiological conditions the terminal carboxyl group renders the molecule

charged, so it has a higher polarity and is more hydrophilic than 5-FU. Thus, 5-FUAcOH hardly diffuses through the lipid core of the cell membranes. However, **CP3n**, whose carboxylic group is coordinated to the metal centre, does not have this obstacle and is able to expose the 5-FUAcOH residue to the interior of the cells.

4.3. Conclusions

The work included in this chapter proved that coordination polymers are not only able to carry drugs inside their pores, but that they can also be the treatment. A new 1D structure using copper(II), 4,4'-bipyiridne and a derivative of the anti-cancer agent 5-FU, 5-FUAcOH, was prepared. To compare the effectivity of 5-FUAcOH, an analogous structure with the nucleobase derivative (UAcOH) was prepared. The stability of both coordination polymers was studied at different conditions and in cell culture media. Although coordination polymers are robust materials when they are formed, the lability of the coordination bonds is demonstrated in physiological media. This process enables to obtain a good result of cytotoxic essays for the coordination polymer with 5-FUAcOH.

4.4. References

(1) Sun, Y.; Zheng, L.; Yang, Y.; Qian, X.; Fu, T.; Li, X.; Yang, Z.; Yan, H.; Cui, C.; Tan, W. Metal–Organic Framework Nanocarriers for Drug Delivery in Biomedical Applications. *Nano-Micro Lett.* **2020**, *12* (1), 103.

(2) Horcajada, P.; Serre, C.; Maurin, G.; Ramsahye, N. A.; Balas, F.; Vallet-Regí, M.; Sebban, M.; Taulelle, F.; Férey, G. Flexible Porous Metal-Organic Frameworks for a Controlled Drug Delivery. *J. Am. Chem. Soc.* **2008**, *130* (21), 6774–6780.

(3) He, C.; Lu, K.; Liu, D.; Lin, W. Nanoscale Metal–Organic Frameworks for the Co-Delivery of Cisplatin and Pooled SiRNAs to Enhance Therapeutic Efficacy in Drug-Resistant Ovarian Cancer Cells. *J. Am. Chem. Soc.* **2014**, *136* (14), 5181–5184.

(4) Rezaei, M.; Abbasi, A.; Dinarvand, R.; Jeddi-Tehrani, M.; Janczak, J. Design and Synthesis of a Biocompatible 1D Coordination Polymer as Anti-Breast Cancer Drug Carrier, 5-Fu: In Vitro and in Vivo Studies. *ACS Appl. Mater. Interfaces* **2018**, *10* (21), 17594–17604.

(5) Miller, S. R.; Heurtaux, D.; Baati, T.; Horcajada, P.; Grenèche, J.-M.; Serre, C. Biodegradable Therapeutic MOFs for the Delivery of Bioactive Molecules. *Chem. Commun.* **2010**, *46* (25), 4526.

(6) Gamelin, E. C.; Danquechin-Dorval, E. M.; Dumesnil, Y. F.; Maillart, P. J.; Goudier, M. J.; Burtin, P. C.; Delva, R. G.; Lortholary, A. H.; Gesta, P. H.; Larra, F. G. Relationship between 5-Fluorouracil (5-FU) Dose Intensity and Therapeutic Response in Patients with Advanced Colorectal Cancer Receiving Infusional Therapy Containing 5-FU. *Cancer* **1996**, *77* (3), 441–451.

(7) Taylor, S. G.; Murthy, A. K.; Griem, K. L.; Recine, D. C.; Kiel, K.; Blendowski, C.; Hurst, P. B.; Showel, J. T.; Hutchinson, J. C.; Campanella, R. S.; et al. Concomitant Cisplatin/5-FU Infusion and Radiotherapy in Advanced Head and Neck Cancer: 8-Year Analysis of Results. *Head Neck* **1997**, *19* (8), 684–691.

(8) Parker, W. B.; Cheng, Y. C. Metabolism and Mechanism of Action of 5-Fluorouracil. *Pharmacol. Ther.* **1990**, *48* (3), 381–395.

(9) Longley, D. B.; Harkin, D. P.; Johnston, P. G. 5-Fluorouracil: Mechanisms of Action and Clinical Strategies. *Nat. Rev. Cancer* **2003**, *3* (5), 330–338.

(10) Thomas, S. A.; Grami, Z.; Mehta, S.; Patel, K.; North, W.; Hospital, F. Adverse Effects of 5-Fluorouracil: Focus on Rare Side Effects. *Cancer Cell Microenviron.* **2016**, 3–6.

(11) Yan, Z.; Li, X.; Fan, Q.; Bai, H.; Wu, S.; Zhang, Z.; Pan, L. A Water-Stable and

Biofriendly Zn-MOF with Pyrazine Decorated Pores as 5-Fu Delivery System to Induce Human Ovarian Cancer Cells Apoptosis and Abrogate Their Growth. *J. Mol. Struct.* **2020**, *1204*, 127477

(12) Gan, B. K.; Rullah, K.; Yong, C. Y.; Ho, K. L.; Omar, A. R.; Alitheen, N. B.; Tan, W. S. Targeted Delivery of 5-Fluorouracil-1-Acetic Acid (5-FA) to Cancer Cells Overexpressing Epithelial Growth Factor Receptor (EGFR) Using Virus-like Nanoparticles. *Sci. Rep.* **2020**, *10* (1), 16867.

(13) Ekberg, H.; Tranberg, K.-G.; Persson, B.; Jeppsson, B.; Nilsson, L.-G.; Gustafson, T.; Andersson, K.-E.; Bengmark, S. Intraperitoneal Infusion of 5-FU in Liver Metastases from Colorectal Cancer. *J. Surg. Oncol.* **1988**, *37* (2), 94–99.

(14) Khosravi, N.; Shahgoli, V. K.; Amini, M.; Safaei, S.; Mokhtarzadeh, A.; Mansoori, B.; Derakhshani, A.; Baghbanzadeh, A.; Baradaran, B. Suppression of Nanog Inhibited Cell Migration and Increased the Sensitivity of Colorectal Cancer Cells to 5-Fluorouracil. *Eur. J. Pharmacol.* **2021**, *894* (January), 173871.

(15) Liu, Q.; Liu, X.; Shi, C.; Zhang, Y.; Feng, X.; Cheng, M.; Su, S.; Gu, J. A Copper-Based Layered Coordination Polymer: Synthesis, Magnetic Properties and Electrochemical Performance in Supercapacitors. *Dalt. Trans.* **2015**, *44* (44), 19175–19184.

(16) Talin, A. A.; Centrone, A.; Ford, A. C.; Foster, M. E.; Stavila, V.; Haney, P.; Kinney, R. A.; Szalai, V.; El Gabaly, F.; Yoon, H. P.; et al. Tunable Electrical Conductivity in Metal-Organic Framework Thin-Film Devices. *Science (80-.).* **2014**, *343* (6166), 66–69.

(17) Proksch, E. PH in Nature, Humans and Skin. *J. Dermatol.* **2018**, *45* (9), 1044–1052.

CHAPTER 5. FROM 1D NANOSCALE COORDINATION POLYMER TO HYDRO AND AEROGELS WITH SELECTIVE SEPARATION BY MOLECULAR RECOGNITION

5.1. Introduction

Searching new materials based on coordination polymers is the norm nowadays. The extensive and interesting properties arising from the multiple combinations between metals and ligands make them play an essential role on a wide range of applications. However, these applications can be improved if the coordination polymers are combined with other materials forming composites such as with PVDF to produce flexible and elastic thin-films[1], graphene to intensify the conductivity in electrode materials[2] or biomolecules to create an antibody capable of performing an immunoassay[3]. Sometimes, it is only necessary to introduce a slight change in the reaction conditions to obtain a new system like gels, exceptional soft materials with applications in varied fields such as cosmetics, medicine or sensors[4–7]. There are many forms of gels surrounding our daily life but it is still an unknown world to be explored.

Gels are 3D network structures formed by interconnected fibers in which the solvent is entrapped inside the formed cavities and

depending on the type of solvent they can be classified as organogels or hydrogels, if the trapped solvent is an organic solvent or water, respectively. Despite the numerous studies about gels, the obtention of these materials continues to be considered a serendipity process. There are many studies about gels formed by low-molecular-weight gelators (LMWG), small organic molecules (molecular weight below 3000) self-assembled by supramolecular interactions that are able to retain large amounts of solvent, or based in organic polymers[8]. However, the production of metal-organic gels (MOG) is quite recent and there is still a long way to cover. The most common MOG are those in which a metal complex acts as gelator[9,10] establishing non-covalent interactions to immobilize the solvent molecules. Recently, studies with MOFs and coordination polymers have generated interest, but it is usual that they are mixed with organogelators or a matrix to guarantee the gel obtention with the desired properties[11]. Only a few examples form a gel directly from the coordination polymer structure[12].

Releasing the solvent from the entangled fibers of a MOG can provide two new materials. The solvent can be extracted using a supercritical fluid, commonly carbon dioxide (CO_2). This method enables to remove the solvent and maintain the microstructure, so the pores do not collapse, and a new light porous material is obtained, a metal-organic aerogel (MOA). On the other hand, if the MOG is dried by evaporation, the pores collapse, and the microstructure suffers a drastic shrinkage generating a metal-organic xerogel MOX). Both materials have their qualities like tailorable shape, high surface area or porosity and are used in different applications, such as water

treatment by liquid adsorption[13], as electrode materials for supercapacitors[14] or as support for phase changes[15].

In this chapter, a new gel based on a 1D nanoscale coordination polymer is obtained from a simple one-pot reaction.

5.2. Results and Discussion

After the wide range of conditions tested trying to obtain the previous coordination compound **CP2** at the nanoscale, it was found that at room temperature, when the purple colloid is filtered, another coordination polymer was obtained in the mother liquor. The dark blue crystals, whose structure was solved by SCXRD, correspond to a new coordination polymer with formula $[Cu_2(UAcO)_2(CH_3COO)_2(4,4'\text{-bipy})_2]_n \cdot 3H_2O$ (**CP4**) (Figure 5.1 and section A5.2.4, page 208). The structure shows a 1D ladder-like coordination polymer in which the copper(II) metal centers are bridged by the 4,4'-bipyridine and double CH_3COO ligands defining the side rail and the rung of the ladder chain, respectively (Figure 5.1a). The geometry adopted around the metal center is an elongated square pyramidal geometry, which includes a terminal uracil-1-acetate ligand. The basal plane is occupied by two trans-nitrogen atoms from two bridging 4,4'-bipy ligands, an oxygen atom from the acetate bridging ligand and another oxygen atom from the carboxylate group of the terminal UAcO ligand. The apical position is occupied by a symmetry-related oxygen atom from the acetate bridging ligand with a significantly longer Cu-O distance. In fact, the acetate ligand adopts an asymmetric μ-oxo coordination mode in which the same oxygen atom occupies the basal plane of the metal center and the apical position of the second copper(II) ion (Figure 5.1b).

Although it is expected that the nucleobases establish direct complementary hydrogen bonding interactions or π-π stacking

interactions, there is only one C-H···O hydrogen bond involving direct nucleobase···nucleobase interactions. Thus, supramolecular sheets that spread along the *ac* plane are formed (Figure 5.1c). The three-dimensional cohesion of the crystal structure is provided by the hydrogen bond interactions between the crystallization water molecules and the ligands. One of the crystallization water molecules establishes a double hydrogen bond O···H-Ow-H···O with the non-coordinated oxygen atoms of the two carboxylates groups coordinated to the metal center, which reinforces their monodentate coordination mode. The other two crystallographically independent water molecules interact with the nucleobases (Figure 5.1d).

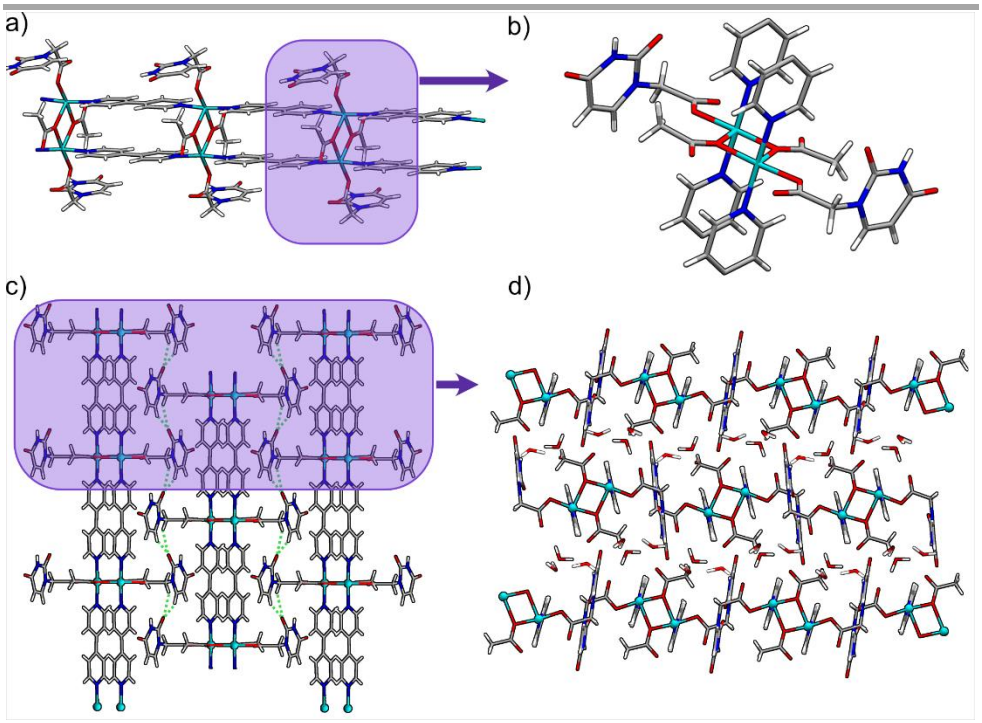

Figure 5.1. (a) Crystal packing of **CP4** showing the polymeric complex entities and the crystallization water molecules. (b) Assembly of the polymeric chains through direct C-H···O hydrogen bonds between the uracil residues generates supramolecular sheets parallel to the crystallographic *ac* plane. Ladder-like coordination polymeric chain (c) and magnification of the metal coordination environment (d). Dashed lines indicate hydrogen bonding interactions.

Once again, the uracil-1-acetate ligands are coordinated to the metal center by one of the oxygen atoms of the carboxylate leaving the uracil moiety free for further applications. Therefore, the conditions to obtain the nanoscale coordination polymer of **CP4** at room temperature are sought. As it is showed in Chapter 4, the mixture of Cu(II) salt, and the ligands 4,4'-bipy and UAcOH in mild conditions led to the compound **CP2n**. Thus, **CP4n** is obtained by the addition of

acetic acid in the reaction giving as a result a purple colloid (Figure 5.3a). **CP4n** is characterized by PXRD, ATR-FT-IR and elemental analysis (Figure 5.2 and section A5.2.1, page 206). The PXRD pattern confirms that **CP4n** has the same crystal structure as **CP4**, and the IR spectrum shows two intense bands between 1700 cm^{-1} and 1500 cm^{-1} corresponding to C=O bonds from the monodentate uracil-1-acetate ligand and the acetate coordinated as bridging ligand between two coppers, respectively.

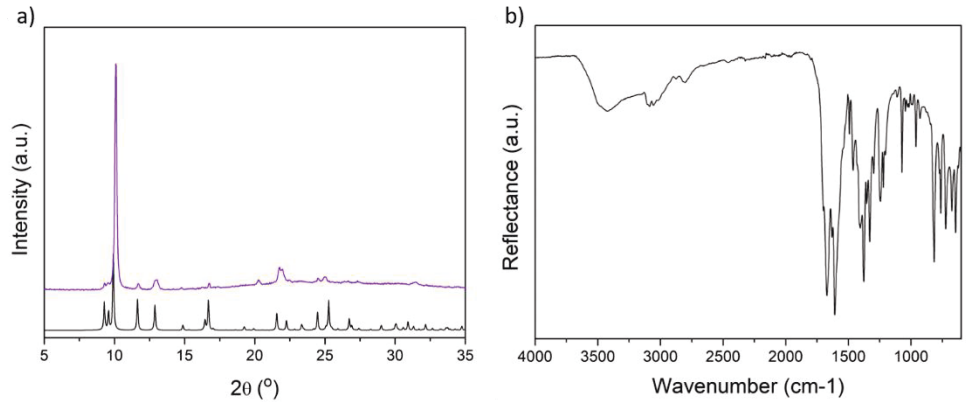

Figure 5.2. a) PXRD pattern of **CP4n** (purple) and simulated PXRD pattern (black). b) ATR-FT-IR spectra of CP4n (black).

The morphological study was carried out by SEM and AFM to corroborate the nanometric size of the compound. The SEM and AFM images show a clear ribbon morphology with an average size of 500 nm of width, 4 µm of length and 28 nm of thickness (Figure 5.4a).

The purple colloid of **CP4n** obtained at room temperature is transformed after 24 h in a hydrogel (confirmed by glass inversion test) (Figure 5.3b). However, the hydrogel or metal-organic hydrogel of CP4n (named **CP4-MOG** for simplicity) obtained in these conditions

does not have a good consistency. So knowing that a slight change in the synthetic conditions can be crucial to obtain a good quality MOG[12], different changes in the synthetic method were explored to achieve the best **CP4-MOG**. The most significant difference was observed when ultrasonication was used during the synthesis. This type of stimulus is usually employed in gel preparation[16]. In this case, the gel formation is not direct, so that ultrasonication should favor the fragmentation and dispersion of the starting crystallites, increased the population of nuclei, and resulted in a faster and disorganized growth of ribbons. This entanglement generates after 24 h the hydrogel of **CP4n**. Among all the conditions modified to obtain **CP4-MOG**, the role of the temperature, time, and the stoichiometry of acetic acid in the reaction also seem crucial factors in the gelation process (Table 5.1).

Table 5.1. Studies of favorable conditions to gel obtention.

HYDROGEL FORMATION	
STOICHIOMETRY (Cu(II) acetate:Acetic Acid)	
1:1	Unconsolidated Hydrogel
1:2	Unconsolidated Hydrogel
1:3	**Optimum Hydrogel**
1:4	Unconsolidated Hydrogel
TEMPERATURE	
< 15 °C	Colloidal Suspension
15 – 30 °C	**Optimum Hydrogel**
TIME	

< 24 h	Colloidal Suspension
24 h	**Optimum Hydrogel**

CP4-MOG retains around 50 mL of water for every gram of compound. However, this solvent entrapped in the hydrogel can be released providing two new materials. If there is a slow exchange under supercritical conditions, an aerogel is obtained (**CP4-MOA**). On the other hand, when the solvent is exchanged through an open-air drying procedure, the pores collapse yielding a low porosity material, a xerogel (**CP4-MOX**). Both materials are characterized by PXRD and ATR-FT-IR confirming that they have the crystalline structure of **CP4** (Figure A5.2, page 214).

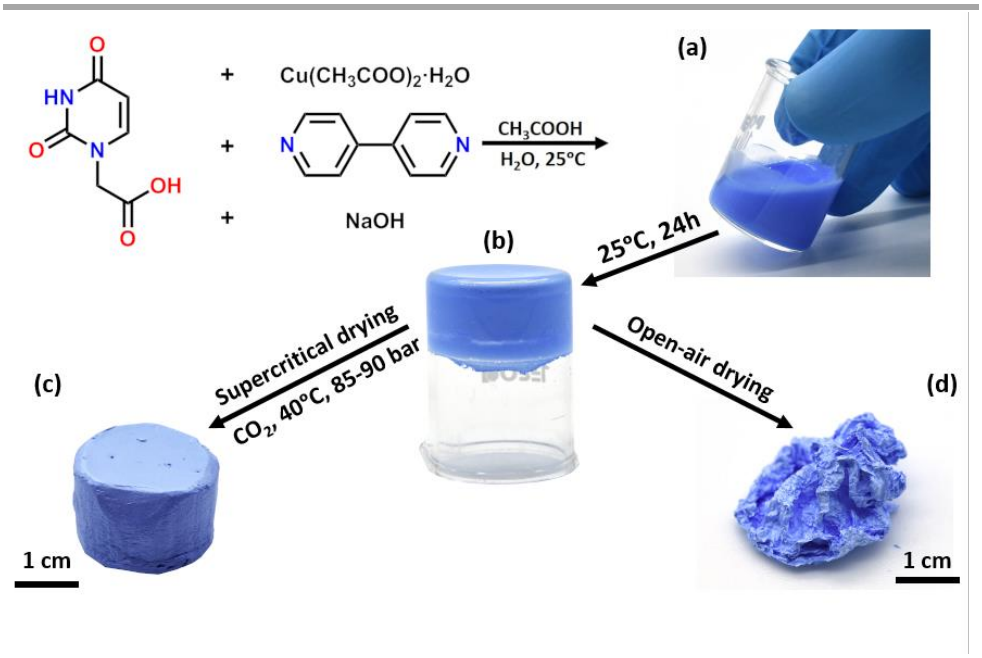

Figure 5.3. Images of a **CP4n**, colloidal suspension in water (a), in **CP4-MOG** (b), **CP4-MOA** (c) and **CP4-MOX** (d) forms.

CP4-MOA and **CP4-MOX** were also studied by SEM and AFM to examine any change in morphology or size. SEM images of **CP4-MOA** show an entanglement of ribbons like a complex spiderweb, in which macropores of hundreds of nanometers can be distinguished (Figure 5.4b). Although the SEM images of **CP4-MOX** also show an entanglement of ribbons, in this occasion they appear like a dense layer of ribbons without cavities (Figure 5.4c). The AFM images enable to measure the dimensions of both materials, but the degree of intertwinement between the ribbons was such in the xerogel, that the dispersion of the ribbons was poor, and the measurements may be overestimated. The aerogel and the xerogel ribbons have an

average thickness of 62 nm for **CP4-MOA** and 8 nm for **CP4-MOX** (Figure 5.4 b-c).

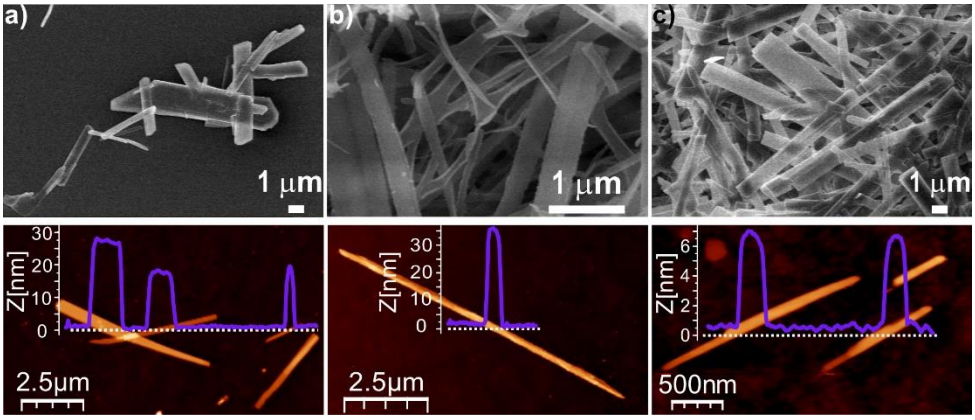

Fig. 5.4. SEM and AFM images of a) a colloidal suspension in water of **CP4n**, b) **CP4-MOA** and c) **CP4-MOX.**

The wide range of applications for these materials has been mentioned previously but it is essential to know their behavior when they are exposed to different conditions. The stability of **CP4n** and **CP4-MOG** was analyzed over time, over periods longer than one month to be precise. The aqueous colloid of **CP4n** was stored at room temperature and studied by PXRD and SEM after one month. The PXRD pattern and the SEM images show that the colloid is stable for long periods of time without changes in the structure nor the morphology (Figure 5.5).

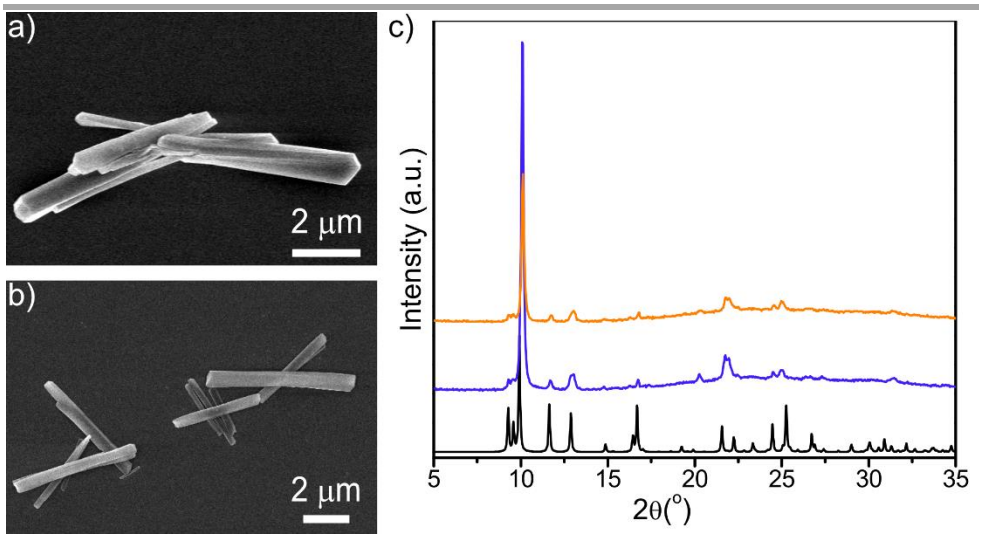

Figure 5.5. FESEM images of compound **CP4n** a) freshly prepared and b) after one month. c) PXRD patterns of simulated from single crystal structure (black line), **CP4n** freshly prepared (blue line) and **CP4n** (orange line) after one month.

The stability of **CP4-MOG** was evaluated in a monolith conserved at room temperature immersed in ethanol**.** The appearance of the monolith is preserved over time with a slight decrease in volume (Figure 5.6).

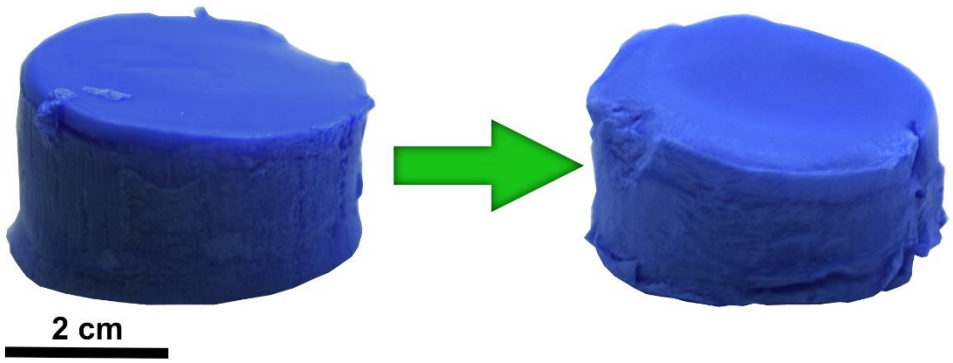

Figure 5.6. Monolith **CP4-MOG** freshly prepared (left) and one month later (right). The monolith preserves its morphology and its dimensions.

The behavior of **CP4n**, **CP4-MOG**, **CP4-MOA** and **CP4-MOX** were studied at different pH values (section A5.3.1, page 215-218). The initial pH of **CP4n** is around 5, so to change the pH range, each compound was immersed in two different buffer solutions at pH 4.5 and 6. The results of this stability test were analyzed after 24 h by PXRD and SEM. As it can be observed in section A5.3.1, all the compounds suffered structural transformations, probably due to the complex acid-base equilibrium between the nucleobase and the carboxylic groups. This transformation is obvious in the SEM images, in which the morphology has changed drastically.

The stability of **CP4-MOG**, **CP4-MOA** and **CP4-MOX** was studied in a broad range of organic solvents. In this case, all materials are stable after one week immersed in the solvents, as it was confirmed by the PXRD patterns and the photographs (section A5.3.1, page 219-221).

When the hydrogel of **CP4-MOG** exchanges the solvent by supercritical CO_2 a light monolith of **CP4-MOA** is obtained. This new

material maintains the structure including the cavities occupied by the solvent, so a porous material can be generated. To analyze the porosity of **CP4-MOA** the N_2 adsorption/desorption isotherms were measured at 77 K (Figure 5.9a). According to the IUPAC classification[17], the adsorption branch of the aerogel is similar to a type II isotherm, which means that the monoliths of **CP4-MOA** have a macroporous nature. Thus, the adsorption data were fitted to Brunauer-Emmett-Teller (BET) to obtain the specific surface area, whose value was 21 m^2g^{-1}. Such a low value for a porous material can be assigned to the ribbon-like shape of the crystals composing the aerogel. The thickness of the crystal was estimated to be 52 nm, which is comparable to the average size of 61 nm obtained by AFM (Table AZ, page Z).

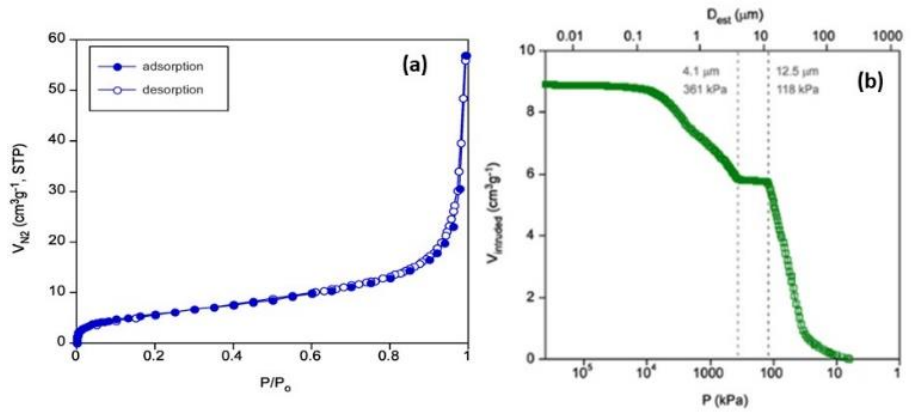

Figure 5.7. Porosity curves of **CP4-MOA** analyzed using the N_2 adsorption/desorption isotherms measured at 77 K (a) and using mercury porosimetry (b).

In view of the macroporous nature of **CP4-MOA**, mercury porosimetry was carried out to study the porosity of the material. The SEM images estimated the highest pore size below 10 µm, so based

on the arbitrary pore size distribution expected for an aerogel, the mercury intrusion should start at pressures close to 145 kPa and increase continuously up to the maximum intruded value (saturation). However, the experimental mercury intrusion curve shows two apparent intrusion segments separated by a plateau (Figure 5.7b). The first segment is from 10 to 86 kPa, which are much lower pressure values than expected. This initial "apparent intrusion" in **CP4-MOA** can be explained as a plastic deformation arising from the microstructural compression caused by the increasing mercury pressure. The gradual compression of the sample leads to progressive toughening and pore size reduction in such a way that a plateau is reached at 86 kPa. The sample stays unaltered until a pressure of 344 kPa, after which the intruded volume increases again. At the plateau, the mercury pressure is incapable of shrinking the monolith further, but it is still not high enough as to infiltrate into the remaining cavities of the monolith. For that reason, the second segment corresponds to the real infiltration into the remaining pores of the compressed sample, whose size is lower than 4.3 μm and which are not necessarily related to the voids present in the initial sample. However, the total measured mercury volume can be considered representative of the total pore volume of the unaltered aerogel. This is supported by assuming that at lower pressure values the incorporated mercury volume was previously occupied by the monolithic sample and the true intrusion phenomena is produced when the additional volume is incorporated at higher pressure values. Thus, **CP4-MOA** has a pore volume of 0.908 $cm^3 \cdot g^{-1}$ and a porosity of 93 %, which correspond to the values of previously reported MOAs (0.030–0.311 $cm^3 \cdot g^{-1}$; 0.44–4.25 $cm^3 \cdot g^{-1}$; 40-95%)[12].

The low apparent density of **CP4-MOA** (0.104 g·cm^{-3}) quantitatively highlights the lightness of the material. In comparison, the estimated density value of the framework from the helium pycnometric data (1.45 g·cm^{-3}) resembles **CP4** crystallographic density (1.56 g·cm^{-3}). This behavior showed in the mercury porosimetry has been previously described for other soft porous materials[18,19], but so far, this is the first case in which an intermediate steady state as wide that it separates clearly the mechanical deformation and real intrusion has been found.

Such phenomenon implies that the density and the porosity of **CP4-MOA** can be tailored by an applied force exerted on the monolith. Figure 5.10 shows the example of a monolith of **CP4-MOA** compressed upon 38 kPa of stress (strain: 63%) in which a significant amount of porosity (98% of porosity for pristine specimen compared to 94.5% for compressed specimen) is still retained.

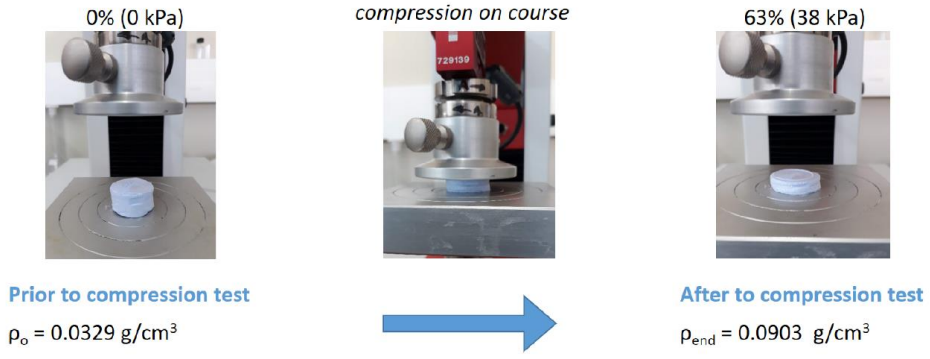

Figure 5.8. Images acquires during the compression test of **CP4-MOA**.

In order to evaluate the mechanical stiffness of **CP4-MOA** cylindrical monoliths (density of 0.0329 g·cm^{-3}) uniaxial compression tests were

performed (Figure 5.8 and section A5.2.7, page 211-212). The stress-strain curves (Figure A5.1, page 212) show a Hookean compression below 7-9 % of strain for all samples, after which they compress plastically without fracturing. The material increases its densification under additional stress.

Young's modulus values obtained by the tested **CP4-MOA** (E: 114-171 kPa) are extraordinarily high for such a light material (Table A5.3, page 212). Actually, these values are related to those obtained in silica aerogels with similar apparent densities (E: 30-140 kPa for density values of 0.04 to 0.1 g·cm^{-3})[20]. However, the few metal-organic aerogels mechanically characterized until now are feebler such as the aerogel of the benchmark HKUST-1, whose Young's modulus is 16-34 kPa (density range: 0.015-0.032 g·cm^{-3})[21] or the series of fibrillary MOAs based on 1D-[M(dithiooxamidate)]$_n$ (M(II): Ni, Pd, Cu) coordination polymers that exhibit a modulus ranging from 0.3 to 74.6 kPa (density values: 0.06-0.08 g·cm^{-3})[12].

It is also remarkable that the Young's modulus of **CP4-MOA** exhibits a linear dependance with the density, where the slope corresponds to the specific modulus ($E = E_{specific} \cdot \rho$; $E_{specific}$ = 5.03 kPa·m^3·kg^{-1} and R^2: 0.9997) (Figure A5.1b, page 212). Thus, the specific modulus is not affected by the apparent density changes, so it can be regarded as an intrinsic feature of **CP4-MOA**. This statement is correct within the explored range and the relationship between the Young's modulus and density is expected to follow a power-law type equation for higher density[22].

As shown by the results above, **CP4-MOA** is an aerogel with meso/microporous nature and formed by cross-linked ribbons of nanometric thickness of a 1D coordination polymer. Besides, this coordination polymer (**CP4**) has in its structure a free uracil moiety, which provides a highly selective supramolecular interaction scheme at the surface level (Figure 5.9). Therefore, taking advantage of this selectivity, **CP4-MOA** was used as a stationary phase in HPLC columns. In this sense, small fragments of **CP4-MOA** (*ca.* 0.5-1 mm) were used to fill a steel column with a length of 100 mm and a diameter of 4.6 mm. This system was tested on a HPLC-PDA chromatograph to separate a series of representative molecules of different nature (naphthalene, toluene, 1-naphthol and binol) using as eluent a mixture of hexane/isopropanol (90:10) at a flow of 1 $mL \cdot min^{-1}$. Unfortunately, the aerogel suffers a severe contraction by the pressure exerted by the eluent, which drastically increases the pressure needed to allow the eluent to flow through the column preventing the chromatograph to work under safe conditions. Thus, the very low flow and the less polar mixture of eluents required for the column to work are not a good combination for the effective separation of the compounds.

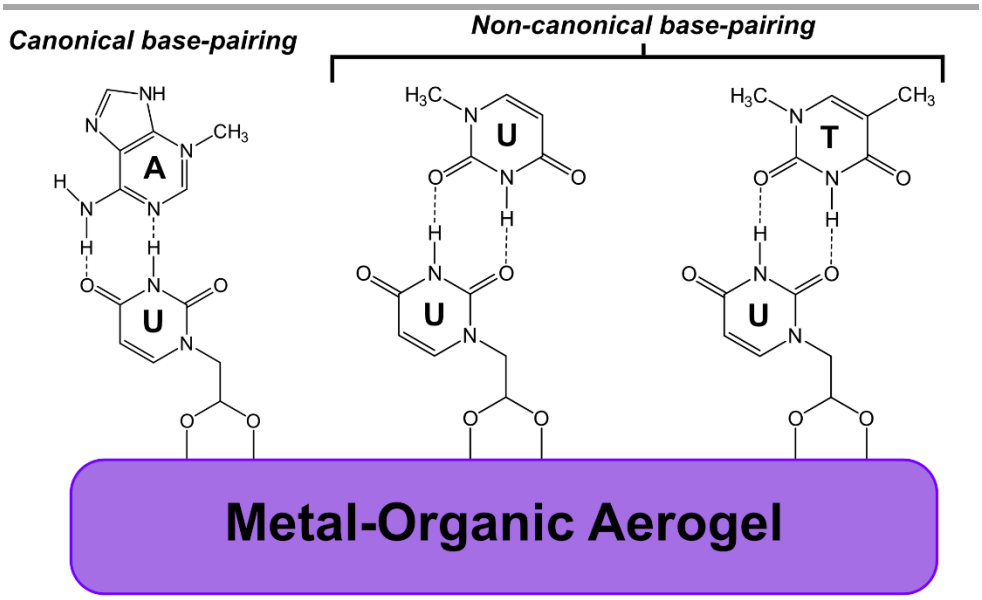

Figure 5.9. Plausible supramolecular interactions between the methylated nucleobase and the stationary phase.

As a result, we implemented an alternative in which **CP4-MOA** was ground with quartz microparticles (1-3 µm) to provide a composite filler (90:10 w/w quartz:aerogel proportion) and prevent the collapse of the aerogel nanofibers into a dense and almost impermeable barrier. The column prepared with the composite can work under moderate pressure with common HPLC conditions (flow 1.0 mL·min^{-1}; hexane/isopropanol 90:10). In fact, the composite can provide a successful separation of the above-mentioned representative molecules, but even more interestingly, it is able to separate N9-methyladenine from N1-methylthymine and N1-methyluracil. Besides, the retention times are the expected, following the elution order with a longer retention time for N9-methyladenine as it would be expected from a canonical A-U base-pairing interaction (Figure

5.10). To prove that the column performance is due to the presence of **CP4-MOA** in the stationary phase, a column based only on quartz microparticles was tested and it did not show any separation capabilities under the same conditions.

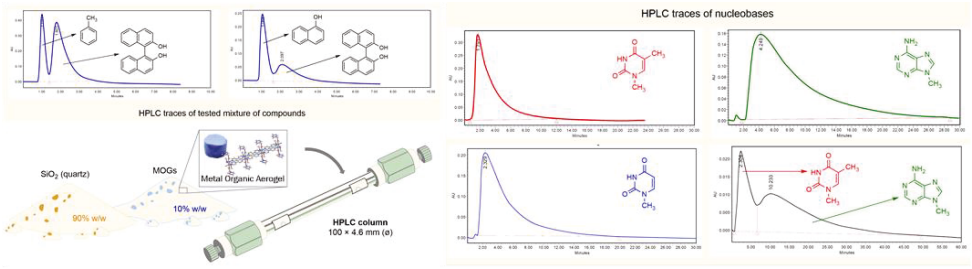

Figure 5.10. Separation performance of the quartz/MOA composite HPLC column.

5.3. Conclusions

This work shows how such a simple change in the reaction conditions enables the obtention under mild conditions of two different systems of the same compound (**CP4n**), a colloidal suspension and a gel. The gel (**CP4-MOG**) can be turned into an aerogel (**CP4-MOA**) or a xerogel (**CP4-MOX**). The chemical stability of each one of these materials has been tested at different times, pH and in organic solvents. They are robust materials, but sensitive to changes in pH. Furthermore, the physical properties of **CP4-MOA** were measured. This aerogel is a light material, characterized by a meso/microporous nature and the ability to be compress without fracturingThe high Young's modulus value is also extraordinary compared to other metal-organic aerogels. All these features added to the structure of the coordination polymer, whose uracil ligand is free to participate in supramolecular interactions, make **CP4-MOA** a good candidate as stationary phase for an HPLC column. Although the peaks obtained with this hand-made column are far from the symmetric shapes resulting from commercial columns, it can be highlighted that it is only necessary 10 % of **CP4-MOA** in the composition of the filler to succeed in the separation of adenine derivatives.

5.4. References

1. Conesa-Egea, J. *et al.* Smart composite films of nanometric thickness based on copper–iodine coordination polymers. Toward sensors. *Chem. Sci.* **9**, 8000–8010 (2018).

2. Kang, Y. *et al.* Bimetallic coordination polymer composites: A new choice of electrode materials for lithium ion batteries. *Solid State Ionics* **350**, 115310 (2020).

3. Wu, S., Tan, H., Wang, C., Wang, J. & Sheng, S. A Colorimetric Immunoassay Based on Coordination Polymer Composite for the Detection of Carcinoembryonic Antigen. *ACS Appl. Mater. Interfaces* **11**, 43031–43038 (2019).

4. Catoira, M. C., Fusaro, L., Di Francesco, D., Ramella, M. & Boccafoschi, F. Overview of natural hydrogels for regenerative medicine applications. *J. Mater. Sci. Mater. Med.* **30**, 115 (2019).

5. Mitura, S., Sionkowska, A. & Jaiswal, A. Biopolymers for hydrogels in cosmetics: review. *J. Mater. Sci. Mater. Med.* **31**, 50 (2020).

6. Cao, X., Gao, A., Hou, J. & Yi, T. Fluorescent supramolecular self-assembly gels and their application as sensors: A review. *Coord. Chem. Rev.* **434**, 213792 (2021).

7. Wei, P. *et al.* Conductive Self-Healing Nanocomposite Hydrogel Skin Sensors with Antifreezing and Thermoresponsive Properties. *ACS Appl. Mater. Interfaces* **12**, 3068–3079 (2020).

8. Hanabusa, K. & Suzuki, M. Development of low-molecular-weight gelators and polymer-based gelators. *Polym. J.* **46**, 776–782 (2014).

9. Shirakawa, M., Fujita, N., Tani, T., Kaneko, K. & Shinkai, S. Organogel of an 8-quinolinol platinum(ii) chelate derivative and its efficient phosphorescence emission effected by inhibition of dioxygen quenching. *Chem. Commun.* 4149 (2005). doi:10.1039/b506148b

10. Ghosh, D., Deepa & Damodaran, K. K. Metal complexation induced supramolecular gels for the detection of cyanide in water. *Supramol. Chem.* **32**, 276–286 (2020).

11. Zhu, L. *et al.* Shapeable Fibrous Aerogels of Metal–Organic-Frameworks Templated with Nanocellulose for Rapid and Large-Capacity Adsorption. *ACS Nano* **12**, 4462–4468 (2018).

12. Vallejo-Sánchez, D. *et al.* Chemically Resistant, Shapeable, and Conducting Metal-Organic Gels and Aerogels Built from Dithiooxamidato Ligand. *Adv. Funct. Mater.* **27**, 1605448 (2017).

13. Wang, C. *et al.* Large-Scale Synthesis of MOF-Derived Superporous Carbon Aerogels with Extraordinary Adsorption Capacity for Organic Solvents. *Angew. Chemie Int. Ed.* **59**, 2066–2070 (2020).

14. Mahmood, A. *et al.* Nanostructured Electrode Materials Derived from Metal–Organic Framework Xerogels for High-Energy-Density Asymmetric Supercapacitor. *ACS Appl. Mater. Interfaces* **8**, 2148–2157 (2016).

15. Andriamitantsoa, R. S., Dong, W., Gao, H. & Wang, G. Porous organic–inorganic hybrid xerogels for stearic acid shape-stabilized phase change materials. *New J. Chem.* **41**, 1790–1797 (2017).

16. Pandey, V. K., Dixit, M. K., Manneville, S., Bucher, C. & Dubey, M. A multi-stimuli responsive conductive sonometallogel: a

mechanistic insight into the role of ultrasound in gelation. *J. Mater. Chem. A* **5**, 6211–6218 (2017).

17. Thommes, M. *et al.* Physisorption of gases, with special reference to the evaluation of surface area and pore size distribution (IUPAC Technical Report). *Pure Appl. Chem.* **87**, 1051–1069 (2015).

18. Majling, J., Komarneni, S. & Fajnor, V. S. Mercury porosimeter as a means to measure mechanical properties of aerogels. *J. Porous Mater.* **1**, 91–95 (1995).

19. Pirard, R., Heinrichs, B., Van Cantfort, O. & Pirard, J. P. Mercury Porosimetry Applied to Low Density Xerogels; Relation between Structure and Mechanical Properties. *J. Sol-Gel Sci. Technol.* **13**, 335–339 (1998).

20. Venkateswara Rao, A., Bhagat, S. D., Hirashima, H. & Pajonk, G. M. Synthesis of flexible silica aerogels using methyltrimethoxysilane (MTMS) precursor. *J. Colloid Interface Sci.* **300**, 279–285 (2006).

21. Zhang, B. *et al.* High-internal-phase emulsions stabilized by metal-organic frameworks and derivation of ultralight metal-organic aerogels. *Sci. Rep.* **6**, 21401 (2016).

22. Lei, J., Liu, Z., Yeo, J. & Ng, T. Y. Determination of the Young's modulus of silica aerogels – an analytical–numerical approach. *Soft Matter* **9**, 11367 (2013).

CONCLUSIONS

Along these chapters, new applications for well-studied materials as coordination polymers were presented. This work is based on the different use that can have the coordination polymers depends on the building blocks, the size, or the synthesis conditions.

The main characters of this work are the components used to obtain the coordination polymers. In all cases the coordination polymers had a metal center of Cu(II), a biocompatible ligand derivate of nucleobases and a rigid ligand. The combination of these building blocks has led to obtain four new coordination polymers each one with different properties and applications.

The first of them has demonstrated that is possible to turn a coordination polymer into nanoscale in an easy way and the key role of obtain a colloidal suspension to the biological applications. The arrangement of the nucleobase ligand in the structure has enable to explore the molecular recognition property with oligonucleotides of the complementary base and a potential application as carriers. The marvelous advantages of this compound do not finish here, because its synthesis in water at room temperature to obtain the nanoscale coordination polymer can be scaled until obtain liters of the colloidal suspension. Then, the obtention of this compound at large scale allows its processability as ink for 3D printing, which enable to design and transform the material in functional objects. Moreover, a detailed study of the coordination polymer structure reveled its potential use as humidity sensor.

This work shows that coordination polymers can be designed. It was possible to prepare two isostructural coordination polymers, in which the derivate nucleobase of one of them was also an anticancer agent. This procedure enabled to compare the different behavior of each compound in biological media and their effect in two cancer cell lines. Moreover, it is the first study of a 1D coordination polymer as drug carrier.

Finally, it was demonstrated that, a slight change the synthesis conditions can generate different materials. This is the case of the last coordination polymer, which can be obtained as colloidal suspension or as gel. The advantage of a gel is that can be treated to exchange the solvent trapped inside and depends on the conditions two new materials can be obtained an aerogel and a xerogel. Thus, a 1D coordination polymer was transformed in a light and porous material like an aerogel, which in combination with the molecular recognition ability of the structure by the nucleobase led to use this polymer as stationary phase of an HPLC column, showing its efficiency with the retention of the complementary base moiety.

In summary, the building blocks and the synthesis conditions play a key role in the development of new materials and their application in new technologies such as 3D printing.

CONCLUSIONES

A lo largo de estos capítulos se ha expuesto como unos materiales tan estudiados como los polímeros de coordinación pueden ser capaces de demostrar nuevas aplicaciones. Este trabajo se basa en el diferente uso que puede tener un mismo tipo de polímero de coordinación en función de los *bloques de construcción* que lo forman, el tamaño o las condiciones de síntesis.

Los principales protagonistas de este trabajo son los componentes que se han utilizado para obtener los polímeros de coordinación. Todos ellos han tenido en común un centro metálico de Cu(II), un ligando biocompatible de derivado de nucleobase y un ligando rígido. La combinación de estos *bloques de construcción* ha llevado a la obtención de cuatro nuevas estructuras de polímeros de coordinación, cada una de ellas con diferentes propiedades y aplicaciones.

El primero de estos compuestos ha demostrado que es posible modificar el tamaño de un polímero de coordinación a escala nanométrica de una manera sencilla, así como la clave que supone obtener una suspensión coloidal para las aplicaciones biológicas. La disposición de la nucleobase en la estructura ha permitido explorar su capacidad de reconocimiento molecular con oligonucleótidos de la base complementaria y su potencial como transportadores de los mismos. Pero las fabulosas ventajas de este compuesto no acaban ahí, ya que es posible escalar la síntesis en agua y a temperatura ambiente del polímero de coordinación nanoestructurado y obtener

litros de la suspensión coloidal. Así, la posibilidad de obtener este compuesto a gran escala permite su procesado como tinta para impresión 3D, que facilita la obtención y diseño de objetos funcionales. Además, un estudio más detallado sobre la estructura del polímero de coordinación reveló su potencial como sensor de humedad.

Este trabajo también muestra como los polímeros de coordinación pueden ser diseñados. Fue posible preparar dos polímeros de coordinación isoestructurales, donde el derivado de nucleobase era además un agente anticancerígeno. Este procedimiento permitió comparar el comportamiento de cada compuesto en los medios biológicos y su efecto al incubarlos en dos líneas de células cancerígenas. Además, es el primer estudio de un polímero de coordinación 1D como transportador de medicamento.

Por último, se demostró que un pequeño cambio en las condiciones de síntesis puede dar lugar a diferentes materiales. Este es el caso del último polímero de coordinación que puede obtenerse como suspensión coloidal o como gel. La ventaja de obtenerlo como gel, es que se puede tratar para intercambiar el disolvente que tiene atrapado en su interior y dependiendo de cómo sea el proceso se pueden obtener dos nuevos materiales un aerogel o un xerogel. De esta forma se puede transformar un polímero de coordinación 1D en un material ligero y poroso como el aerogel, que combinado con la propiedad de reconocimiento molecular que aporta la estructura por tener la nucleobase, da como resultado la aplicación de este polímero como fase estacionaria de una columna de HPLC y demostrando su

eficacia al ser capaz de retener aquellos compuestos con la base complementaria.

En resumen, los bloques de construcción y las condiciones de síntesis juegan un papel fundamental para el desarrollo de nuevos materiales y su aplicación en las nuevas tecnologías como la impresión 3D.

APPENDIX

A1. General materials and methods

A1.1. Materials

All the general chemicals and solvents were obtained from standard commercial suppliers and used as received without further purification.

A1.2. Methods

Attenuated Total Reflectance Fourier-Transform Infrared Spectroscopy. ATR-FT-IR spectra were recorded in a Perkin Elmer Spectrum 100 with a PIKE Technologies MIRacle Single Reflection Horizontal ATR Accessory with a spectral range of 4000-650 cm^{-1}.

Elemental Analysis. Elemental analyses were performed on an elementary microanalyzer LECO CHNS-932, working with controlled doses of O_2 and a combustion temperature of 1000 °C.

Powder X-ray Diffraction. PXRD patterns were collected using a Bruker D8 Advance X-ray diffractometer (Cu-Kα radiation; λ = 1.5418 Å) equipped with a Lynxeye detector. Samples were mounted on a flat glass plate and analyzed with scanning θ/2θ. Patterns were collected in the 3°<2θ<35° range with a step size of 0.01° and exposure time of 0.3 s/step. Theoretical PXRD patterns were

calculated using Mercury Cambridge Structural Database (CSD) software from the Crystallographic Cambridge Data Base (CCDC).

Single Crystal X-ray Diffraction. SCXRD data collection and structure determination were carried out at 296 K on a Bruker Kappa Apex II diffractometer with graphite-monochromated (Mo-Kα radiation; λ = 0.71073 Å). The cell parameters were determined and refined by a least-squares fit of all reflections. A semi-empirical absorption correction (SADABS) was applied. All the structures were solved by direct methods using the SIR92 program[1] and refined by full-matrix least-squares on F^2, including all reflections (SHELXL)[2].

Field Emission Scanning Electron Microscopy. FESEM images were acquired on a Philips XL 30 S-FEG field emission scanning electron microscope operating at an accelerating voltage of 10 kV. Samples were previously coated with chromium in a sputter Quorum Q150T-S.

Atomic Force Microscopy. AFM images were aquired in dynamic mode using a Nanotec Electronica System operating at room temperature in ambient conditions. The images were processed using WSxM (freely downloadable scanning probe microscopy software from www.nanotec.es). For AFM measurements, commercial Olympus Si/N cantilevers were used with a nominal force constant of 0.75 N/m.

A2. Chapter 2 Experimental Section

A2.1. Materials and methods

Electrical Conductivity. Direct current electrical conductivity measurements were carried out on different single crystals of compound **CP1** with graphite paste and two contacts. The contacts were made with wolframium wires (25 μm diameter). The samples were measured at 300 K applying an electrical current with voltages from +10 to -10 V.

Magnetism. Magnetic measurements were done in a Quantum Design MPMS-XL-5 SQUID magnetometer in the 2-300 K temperature range with an applied magnetic field of 0.1 T on a polycrystalline sample of compound **CP1** and on a sample formed by nano-ribbons of **CP1n** (with masses of 4.73 and 14.64 mg, respectively). Additionally, the nanoribbons (0.54 mg) were measured in water suspension and also the dry sample after removing the water. The susceptibility data were corrected for the sample holders previously measured under the same conditions, and for the diamagnetic contributions as deduced by using Pascal´s constant Tables (χ_{dia} = -310.1·10^{-6} emu·mol^{-1} for **CP1**)[3]. The Hamiltonian is written as:

$$H = -J \sum_i S_i \cdot S_{i+1}$$

solid line in Figure 2.9.

A2.2. Experimental procedures

A2.2.1. Synthesis of CP1

A mixture of $Cu(NO_3)_2 \cdot 3H_2O$ (100 mg, 0.41 mmol), TAcOH (152 mg, 0.82 mmol) and 4,4'-bipy (64 mg, 0.41 mmol) was stirred in 18 mL of water (pH = 4.8) for 10 min at room temperature. The resulting deep blue solution was heated at 140 °C for 3 days in a solvothermal reactor and cooled down to 30 °C with a rate of 0.1 °C/min (final pH = 4.7). The deep blue crystals were filtered off, washed with water, and dried in air (110 mg, 41.9 % yield based on Cu). Elemental analysis calculated for $C_{24}H_{28}CuN_6O_{11}$ (**CP1**): C: 45.04 %, H: 4.41 %, N: 13.13 %. Found: C: 45.35 %, H: 4.36 %, N: 13.13 %. IR selected data (cm^{-1}): 3446 (s), 1704 (s), 1677 (s), 1612 (s), 1471 (w), 1419 (m), 1355 (w), 1301 (w), 1247 (w), 1230 (w), 1078 (w), 1012 (w), 971 (w), 831 (w).

A2.2.2. Synthesis of CP1 at room temperature

A mixture of $Cu(NO_3)_2 \cdot 3H_2O$ (100 mg, 0.41 mmol), TAcOH (152 mg, 0.82 mmol), NaOH (33 mg, 0.82 mmol) and 4,4'-bipy (64 mg, 0.41 mmol) was stirred in 18 mL of water (pH = 6.1) until complete dissolution. A blue solid was formed immediately, and the resulting suspension was stirred for 1 h at room temperature. Then the suspension was filtered off, washed with water, and dried in air (200 mg, 76.2 % yield based on Cu). Elemental analysis calculated for $C_{24}H_{28}CuN_6O_{11}$ (**CP1**): C: 45.04 %, H: 4.41 %, N: 13.13 %. Found: C: 45.10 %, H: 4.26 %, N: 13.08 %. IR selected data (cm^{-1}): 3521 (s), 3059

(s), 1689 (s), 1610 (s), 1470 (w), 1419 (m), 1358 (w), 1302 (w), 1245 (w), 1230 (w), 1077 (w), 1015 (w), 971 (w), 831 (w).

A2.2.3. Synthesis of nanoscale CP1 (CP1n)

A mixture of TAcOH (18 mg, 0.1 mmol) in 1 mL of water and NaOH (3.9 mg, 0.1 mmol) in 1 mL of water was added to a water solution (1 mL) of 4,4'-bipy (7.8 mg, 0.05 mmol) under stirring at room temperature. The resulting clear solution turned onto a deep blue colloid upon addition of 1 mL of a water solution of $Cu(NO_3)_2 \cdot 3H_2O$ (1.2 mg, 0.05 mmol). The blue colloid suspension was stirred for 5 min and washed by centrifuged for 5 min at 10000 rpm four times with 4 mL of Milli-Q water each time. The solid was dried in air (25 mg, 39 % yield based on Cu). Elemental analysis calculated for $C_{24}H_{28}CuN_6O_{11}$ (**CP1n**): C: 45.04 %, H: 4.41 %, N: 13.13 %. Found: C: 45.17 %, H: 4.26 %, N: 13.08 %. IR selected data (cm-1): 3523 (s), 3450 (s), 1693(m), 1681 (w), 1607 (m), 1612 (s), 1471 (w), 1419 (m), 1355 (w), 1301 (w), 1249 (w), 1230 (w), 1078 (w), 1010 (w), 971 (w), 831 (w), 770 (w).

A2.2.4. Structural studies of SCXRD

During the crystal structure solution, it became evident that the thymine residues were disordered. All the attempts to solve the crystal structure using lower symmetry space groups did not avoid the presence of this disorder. The disorder was modelled placing the thymine residues placed over two positions related by a rotation of 180°. The atoms belonging to the disordered part were kept isotropic and soft "SADI" restraints were fixed in order to ensure that the bond distances in both parts of the disordered thymine residues are similar. The hydrogen atoms were included in their calculated

positions and refined riding on the respective carbon atoms. All calculations were performed using the WINGX crystallographic software package[4]. Details of the structure determination and refinement are summarized in Table A2.1.

Table A2.1. Crystallographic data and structure refinement details of compound **CP1**[a].

Empirical formula	$C_{24}H_{28}CuN_6O_{11}$
***M*r**	640.06
Crystal system	Monoclinic
Space group	$P2_1/n$
***a*/Å**	6.5300(1)
***b*/Å**	22.2196(5)
***c*/Å**	18.7306(4)
***α*/°**	90
***β*/°**	960996(1)
***γ*/°**	90
V/Å^3	2697.46(9)
Z	4
D_c/g·cm^{-3}	1.576
μ/mm^{-1}	0.882
Reflections collected	44331
Unique data/parameters	4883/365
R_{int}	0.0414
Goodness of fit (S)[b]	1.152
R_1[c]/wR_2[d] [I>2σ(I)]	0.0693/0.1941
R_1[c]/wR_2[d] [all data]	0.0888/0.2008

[a]Reported data do not include the variable amount of solvent molecules present in the channels. [b]$S = [\Sigma w(F_0^2-F_c^2)^2/(N_{obs}-N_{param})]^{1/2}$; [c]$R_1 = \Sigma||F_0|-|F_c|| / \Sigma|F_0|$; [d]$wR_2 = [\Sigma w(F_0^2-F_c^2)^2/\Sigma wF_0^2]^{1/2}$; $w = 1/[\sigma(F_0^2) + (aP)^2 + bP]$ where $P = (\max(F_0^2,0) + 2F_c^2)/3$ with a = 0.0545 and b = 21.7714.

Table A2.2. Selected bond lengths (Å) and angles (°) for compound **CP1**.

Cu1-N31	2.005(6)	N31-Cu1-N41	171.13(17)	N41-Cu1-O291	88.02(18)
Cu1-N41	2.008(6)	N31-Cu1-O191	91.01(18)	N41-Cu1-O1w	94.7(2)
Cu1-O191	1.970(3)	N31-Cu1-O291	88.87(19)	O191-Cu1-O291	172.40(14)
Cu1-O291	2.020(4)	N31-Cu1-O1w	94.1(2)	O191-Cu1-O1w	88.14(15)
Cu1-O1w	2.307(5)	N41-Cu1-O191	90.98(18)	O291-Cu1- O1w	99.45(15)

Table A2.3. Hydrogen bonding interactions (Å,°) in compound **CP1**[a].

D–H...A[b]	H...A	D...A	D–H...A
O1w–H···O192^{i}	2.02	2.844(6)	162.5
O1w–H···O292	1.98	2.702(6)	141.7
O2wA–H···O192^{ii}	2.05	2.893(11)	171.3
O2wA–H···O191^{iii}	2.03	2.877(11)	170.6
O2wB–H···O292^{iv}	1.94	2.791(10)	170.9
O2wB–H···O291^{v}	2.03	2.877(10)	171.1
O3wA–H···O292^{vi}	1.98	2.825(10)	170.4
O3wA–H···O291^{vii}	2.02	2.865(10)	170.5
O3wB–H···O192^{viii}	2.04	2.890(10)	165.7
O3wB–H···O191^{ix}	2.00	2.842(10)	175.7
C33-H···O24A^{vi}	2.46	3.376(11)	168.2
C33-H···O24B^{vi}	2.24	3.161(10)	170.3
C35-H···O14A^{ii}	2.39	3.312(11)	169.0
C35-H···O14B^{ii}	2.18	3.103(9)	170.7
C43-H···O14A^{viii}	2.26	3.180(10)	171.1
C43-H···O14B^{viii}	2.41	3.342(10)	175.5
C45-H···O24A^{iv}	2.21	3.130(10)	170.6
C45-H···O24B^{iv}	2.37	3.299(11)	178.4
C16A-H···O12B^{ix}	2.34	3.195(14)	152.8
C16B-H···O12B^{vii}	2.32	3.178(15)	153.4
C26A-H···O22B^{v}	2.34	3.196(15)	153.6
C26B-H···O22A^{iii}	2.31	3.165(15)	152.9

[a]Symmetry codes: (i) x-1, y, z; (ii) x-3/2, -y+1/2, z-1/2; (iii) x-1/2, -y+1/2, z-1/2; (iv) –x, -y+1, -z; (v) –x+1, -y+1, -z; (vi) x+3/2, -y+1/2, z+1/2; (vii) x+1/2, -y+1/2, z+1/2; (viii) –x+3, -y+1, -z+1; (ix) –x+2, -y+1, -z+1.

A2.2.5. SEM sample preparation

The surfaces used for FESEM were SiO_2 300 nm thickness (IMS Company). SiO_2 surfaces were cleaned by ultrasonication at 37 KHz and 380 W in acetone for 15 min and in 2-propanol for another 15 min, and then dried under an argon flow.

Diluted suspensions of compound **CP1n** were prepared by adding 50 µL of blue colloid over 600 µL of Milli-Q water. 10 µL of the diluted suspension were deposited on SiO_2 substrates by drop casting deposition for 15 min at room temperature, and then dried under argon flow.

A2.2.6. AFM sample preparation

The surfaces used for FESEM were SiO_2 300 nm thickness (IMS Company). SiO_2 surfaces were cleaned by ultrasonication at 37 KHz and 380 W in acetone for 15 min and in 2-propanol for another 15 min, and then dried under an argon flow.

Diluted suspensions of compound **CP1n** were prepared by adding 50 µL of blue colloid over 600 µL of Milli-Q water. 15 µL of the diluted suspension were deposited on SiO_2 substrates by drop casting deposition for 15 min at room temperature, and then dried under argon flow.

A2.2.7. Modified oligonucleotide synthesis

The oligonucleotides were prepared using a MerMade4 DNA Synthesizer using commercial phosphoramidites (Link Technologies). After solid-phase synthesis, the solid support was transferred to a screw-cap glass vial and incubated at 55 °C for 4 h with 2 mL of ammonia solution (33 %). After the vial was cooled on ice the supernatant was transferred by pipet to microcentrifuge tubes and the solid support and the vial were rinsed with water. The combined solutions were evaporated to dryness using an evaporating centrifuge.

The samples were purified by polyacrylamide gel electrophoresis 20 % and the oligonucleotides were eluted from gel fractions using an elutrap system. The solutions were desalted using a NAP-10 column and concentrated in an evaporating centrifuge.

A2.2.8. Affinity studies

The oligonucleotides (0.0055 M) were incubated with 1n (0.011 M) for 2 hours at room temperature in 600 µL of ultrapure water. Then, the mixture was centrifuged using standard dialysis centrifugal filters (Amicon 10 K, 0.5 mL) to remove the unbound material.

The interaction between 1n and the oligonucleotides was monitored by absorbance measurements at 260 nm of the mixture just upon mixing the two fractions obtained after dialysis filtration. The absorbance was recorded in a Synergy H4 microplate reader, using a 96 well plate at room temperature.

A2.2.9. Cell viability assay

The cytotoxicity of **CP1n** was evaluated in C918, Panc-1 and HaCaTcell lines using the resazurin assayC918 cells were seeded onto 24-well plates at a density of 1.5 x 10^4 cells/well in supplemented RPMI medium (10 % Fetal Bovine Serum (FBS), 1 % L-Glutamine and 1 % Streptomycin/Penicillin). Panc-1 and HaCaT cells were seeded onto 24-well plates at a density of 2 x 10^4 cells/well in supplemented DMEM medium (10% FBS, 1 % L-Glutamine and 1 % Streptomicyn/Penicilin). Then, cells were incubated at standard conditions (37 °C, 5 % CO_2) for 16 h, and the medium was replaced with fresh culture medium containing 1, 50, 100, 150 and 200 µM of **CP1n**. After 24 h of incubation, cells were washed twice with PBS, and incubated 48 h more. Then, the medium was replace by fresh medium containing 1% of a resazurin reagent solution (1mg/mL of resazurin in PBS pH = 7.4). Cells were incubated for 3h, and the fluorescence was measured (Exc 550 nm, Em 590 nm) using a Synergy H4plate reader. Cytotoxicity was expressed as a percentage of the control. All the experiments were performed in triplicates and the standard deviation is represented in the error bars.

A2.2.10. Fluorescent microscopy studies

The sample **CP1n** containing a FITC-labelled oligonucleotide was prepared by the procedure describe before. C918 cells were seeded in a Cell Culture Slide (4 wells) at a density of 1 x 104 cells/well in supplemented RPMI medium (10% FBS, 1% L-Glutamine and 1% Penicillin-Streptomycin) and incubated overnight at standard condition (37 °C, 5% CO2). Then the medium was replaced with serum

free medium (OptiMem) containing 150 µM of 1n with 12.5 µM of labelled PolyA oligonucleotide. After 3 h of incubation, cells were washed twice with PBS, and analyzed in the microscope LEICA DMI3000 B.

A3. Chapter 3 Experimental Section

A3.1. Materials and methods

Powder X-ray Diffraction. PXRD patterns of CP1 heating from room temperature to 140 °C were collected using a Diffractometer PANalyticalX'Pert PRO MPD θ/2θ secondary monochromator and detector with fast X'Celerator. PXRD patterns of immersed samples of CP1 in solvents were collected using a Diffractometer PANalyticalX'Pert PRO ALPHA1 θ/2θ primary monochromator and detector with fast X´Celerator. The immersed samples were prepared on a silicon sample holder and covered with a sheet of kapton and the samples under nitrogen were prepared on a silicon sample holder too with polycarbonate sealing cap. The samples have been analysed with scanning θ/2θ.

Thermogravimetric analysis (TGA) was performed on a TGA Q500 Thermobalance with an EGA (Envolved Gas Analysis) furnace and quadrupole mass spectrometer Thermostat Pfeiffer of Tecnovac, to analyse gases which are given off from the sample. The powder sample was analysed using a Pt sample holder and air flow as purge gas of 90 mL/min with a heating ramp from room temperature to 1000 °C at 10 °C/min.

Differential Scanning Calorimetry was performed on a Discovery DSC. The sample was analysed using hermetic Aluminium pans from 20 °C to 200 °C in a N_2 atmosphere with two heating rate of 5 °C/min and 10 °C/min.

Synchrotron X-ray Total Scattering Data. Synchrotron X-ray total scattering data suitable for Pair Distribution Function (PDF) analyses were collected at the P02.1 beamline at PETRA IIII using 60 keV (0.207 Å) X-rays. Samples were loaded into borosilicate capillaries and sealed using epoxy. Data were collected using an amorphous silicon-based PerkinElmer detector area detector. Geometric corrections and reduction to one-dimensional data used DAWN Science software[5]. PDFs were obtained from the data within PDFgetX3[6] within xPDFsuite to a Qmax = 17 Å−1. Cu-N,O correlations of interest were quantified by fitting Gaussian functions.

Theoretical Modeling and Computational Details. All the first-principles simulations have been performed by using density functional theory (DFT) as implemented in the CASTEP simulation package[7]. Exchange–correlation interactions have been accounted by the generalized gradient approximation (GGA) within the Perdew-Burke-Ernzerhof (PBE) functional[8], which are based on a total energy pseudo-potential plane-wave framework[9]. The Vanderbilt ultrasoft pseudopotential scheme has been adopted to model the ion-electron interactions, and the valence atomic configurations considered are the following: H: $1s^1$, C: $2s^2 2p^2$; N: $2s^2 2p^3$, O: $2s^2 2p^4$, and Cu: $3d^{10} 4s^1$. The cutoff energy has been set to 380 eV, an optimal *k*-point mesh of [6×3×1] and a self-consistent field (SCF) of 1×10^{-6} eV per atom are used for geometry optimizations using the Monkhorst–Pack scheme[10]. Full geometry optimizations, where all the atoms are free to relax, have been carried out before single-point energy calculations and the final net force acting on each atom is less than 0.05 eV $Å^{-1}$, the final stress on the atoms is below 0.05 GPa.

Transition-state barriers have been computed within the Climbing-image Nudged-elastic-band (CI-NEB) approach[11], where the initial and final steps, as well as a sufficient number of intermediate images (20 in this case), have been permitted to fully relax to achieve a converged Minimum Energy Path (MEP). To check the reliability of the results, additional test-calculations with a higher plane-wave cutoff energy and a denser *k*-point grid were performed, yielding no significant changes for both geometric and electronic structures, and obtaining differences between total energies < 0.02 %, which justifies the validity of our calculations. The theoretical crystal-powder diffractograms have been simulated from the DFT-optimized structures by using the MERCURY package[12].

A3.2. Experimental procedures

A3.2.1. Synthesis of CP1-3H_2O

The **CP1-3H_2O** was obtained by heating **CP1** (section A2.2.1, page) during 20 minutes at 135 ºC. Elemental analysis calculated for $C_{24}H_{22}CuN_6O_8$ (**CP1-3H_2O**): C: 49.2 %, H: 3.8 %, N: 14.3 %. Found: C: 48.9 %, H: 3.9 %, N: 14.2 %. IR selected data (cm^{-1}): 3165 (w), 3050 (w), 2823 (w), 1689 (s), 1612 (s), 1630 (m), 1463 (m), 1418 (m), 1377 (m), 1300 (m), 1278 (m), 1246 (m), 1228 (m).

A3.2.2. Preparation of the Printing Formulation

10 wt % : $[Cu(TAcO)_2(H_2O)(4,4'\text{-bipy})]_n \cdot 2H_2O$ (2 g) was mixed with DPGDA (9 g), Sr-9035 (9 g) and DM (4 g) as a solvent. To form a homogeneous dispersion, the mixture was sonicated with a tip-

sonicator (Sonics Vibra-cell, 500 W) for 45 min (1 s ON, 2 s OFF) and 50 % amplitude. Following this, photoinitiators, Irgacure 819 (0.16 g) and Irgacure 184 (0.32 g), were dissolved in the dispersion.

40 wt % : $[Cu(TAcO)_2(H_2O)(4,4'\text{-bipy})]_n \cdot 2H_2O$ (2.26 g) was mixed with DPGDA (1.65 g), SR-9035 (1.65 g) and DM (4.44 g) as a solvent. To form a homogeneous dispersion, the mixture was mixed with a homogenizer (IKA T25) for 5 minutes and 5000 RPM. Following this, photoinitiators, Irgacure 819 (0.07 g) and Irgacure 184 (0.14 g), were dissolved in the dispersion.

A3.2.3. 3D-printing of $[Cu(TAcO)_2(4,4'\text{-bipy})(H_2O)]_n \cdot 2H_2O$ (CP1@3D)

The models containing 10 %wt $[Cu(TAcO)_2(4,4'\text{-bipy})(H_2O)]_n \cdot 2H_2O$ were printed with a digital light processing (DLP) 3D-printer (Asiga Pico2) (Figure 3.3a). The models containing 40 %wt $[Cu(TAcO)_2(4,4'\text{-bipy})(H_2O)]_n \cdot 2H_2O$ were printed with an extruder 3D-printer (Hyrel System 30M) (Figure 3.3b). In both printers, the polymerization was initiated by ultra-violet (UV) light, with a wavelength of 400-405 nm. Following the printing process, the objects were washed with isopropyl alcohol to remove the unpolymerized residues.

A3.3. Additional data

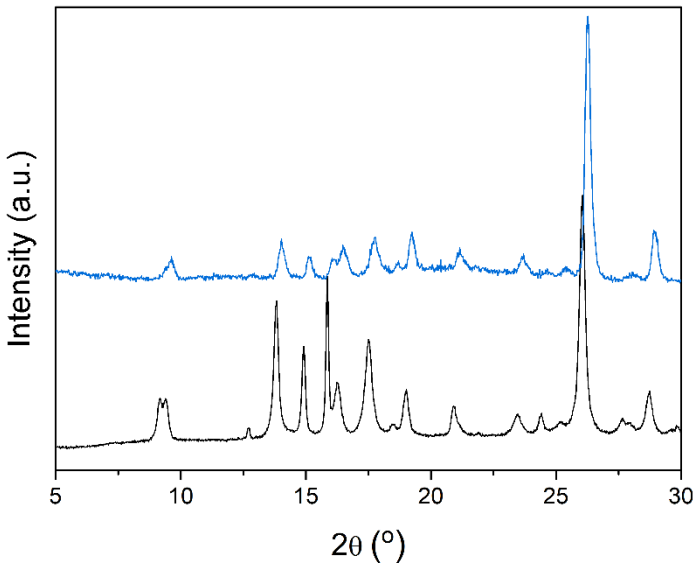

Figure A3.1. PXRD pattern of **CP1@3D** (blue) and **CP1n** (black).

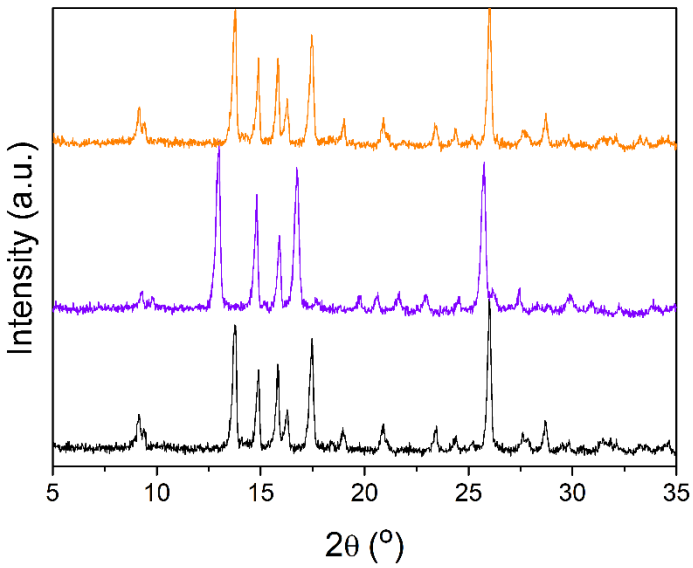

Figure A3.2. PXRD pattern of CP1 heating-cooling cycle. **CP1** at RT (black line), after heating at 60 °C (purple line) and after cooling the sample at RT.

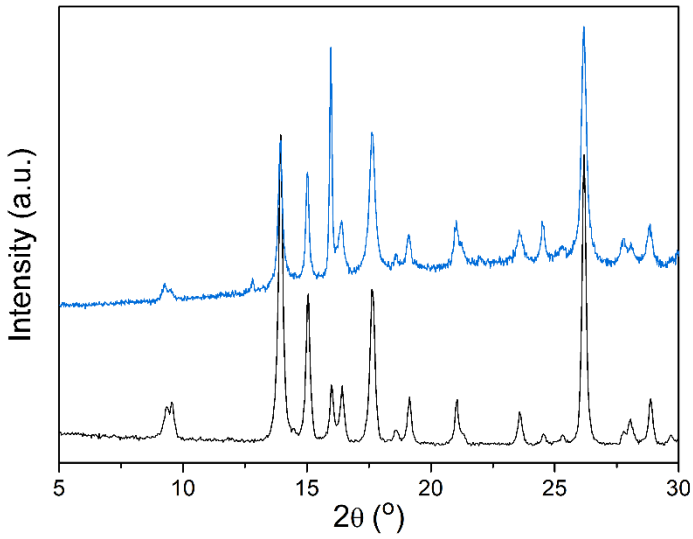

Figure A3.3. PXRD pattern of **CP1** after 20 cycles of heating at 60 °C and cooling at RT (blue line) and **CP1** freshly prepared (black line).

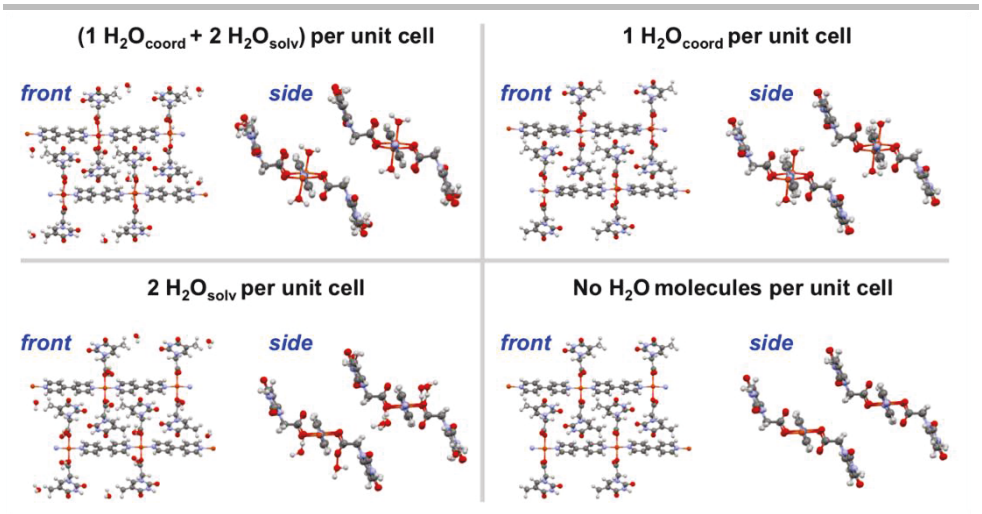

Figure A3.4. Front and side views of the computed optimal geometries for the compound **CP1**: (top-left) with 1 coordination and 2 solvation water molecules per unit cell, (top-right) with 1 coordination water molecule per unit cell, (bottom-left) with 2 solvation water molecules per unit cell, and (bottom-right) with no water molecules.

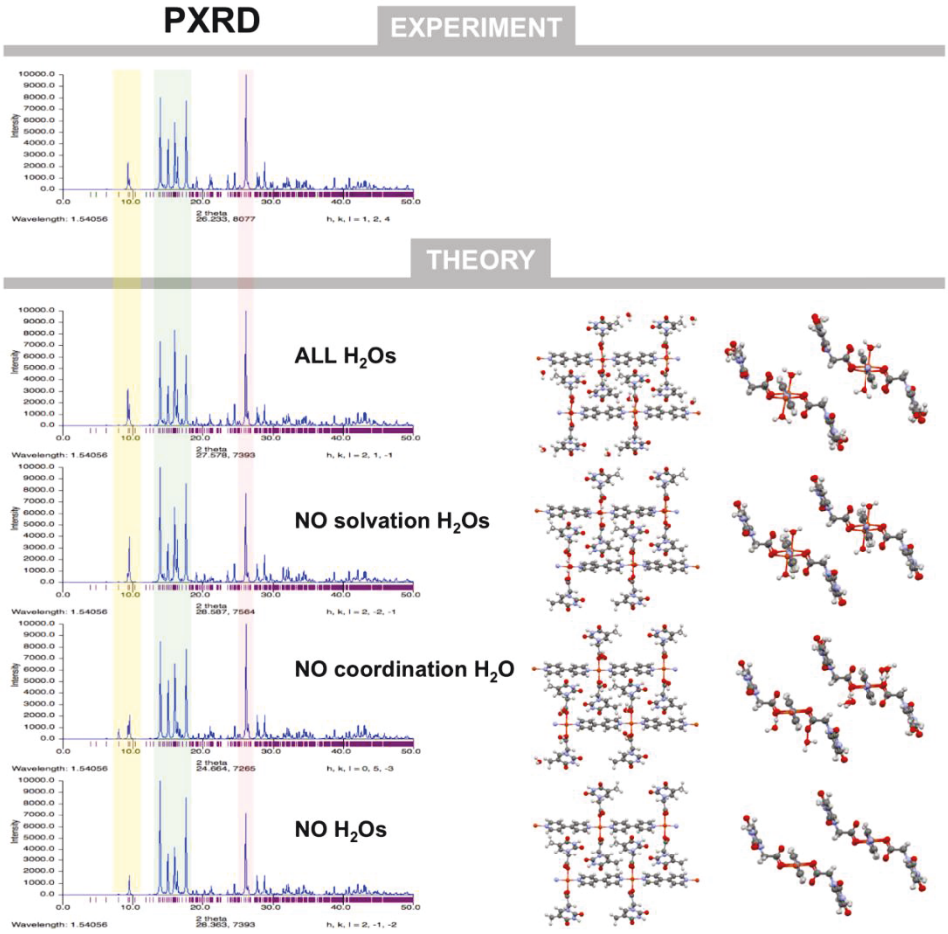

Figure A3.5. (Top panel) Experimental diffractogram for the **CP1** compound with 1 coordination and 2 solvation water molecules per unit cell. (Bottom panel) Simulated PXR diffractograms from the DFT-optimized structures; front and side views of the structures have been included for each corresponding diffractogram. Color-shadowed stripes, overlapping all the PXRD spectra, have been also added highlighting the most representative regions.

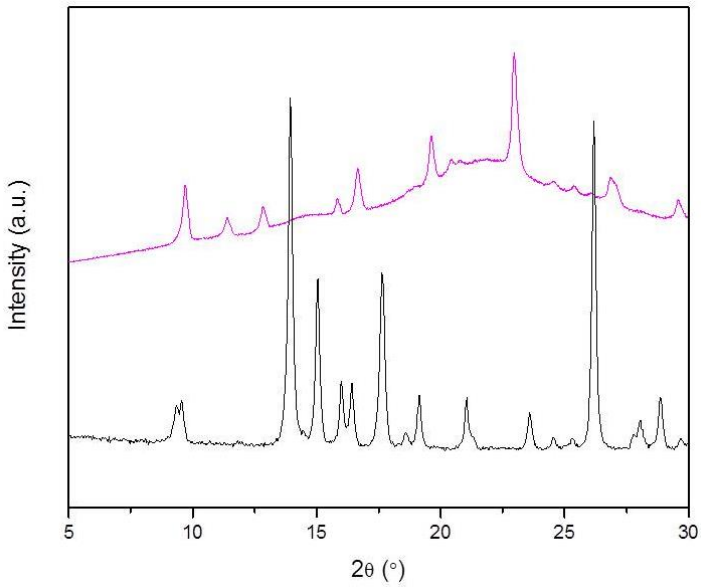

Figure A3.6. PXRD patterns of **CP1** at RT (black line) and the same compound after soaked in dry MeOH (pink line).

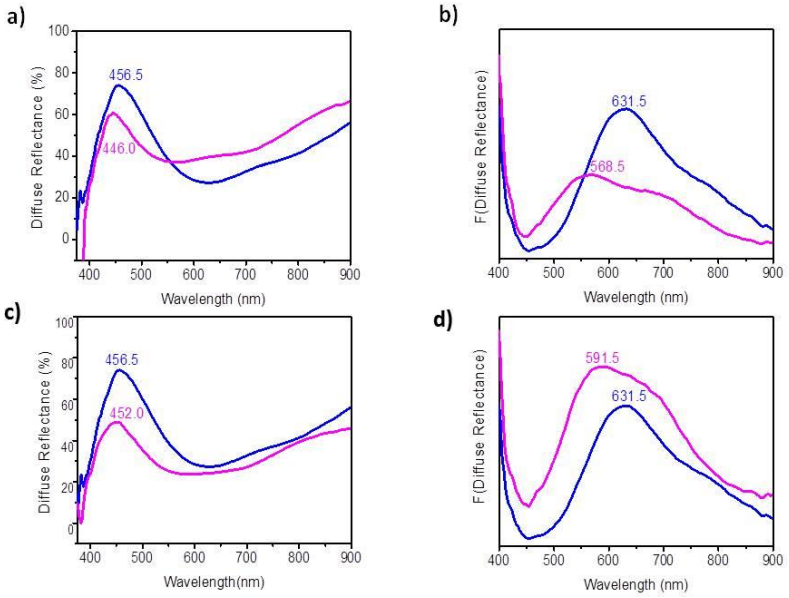

Figure A3.7. Diffuse reflectance **(a, c)** and the Kubelka-Munk **(b, d)**, remission function spectrum obtained for **CP1**, before (initial, blue line) and after (final, violet line) be heated at 66.6 °C (**a** and **b**) and before (initial, blue line) and after (final, violet line) be immersed in dry methanol (MeOH) at 25 °C (**c** and **d**).

		Maximum Wavelength of Diffuse Reflectance (nm)		Maximum Wavelength of Kubelka-Munk (nm)	
	Change	Initial	Final	Initial	final
CP1	MeOH	456.5	452.0	631.5	591.5
CP1	66.6 °C	456.5	446.0	631.5	568.5

Table A3.1. Comparison of maximum wavelengths of both, the diffuse reflectance spectra and the Kubelka-Munk remission function of **CP1,** before (initial) and after (final) heating at 66.6 °C and before (initial) and after (final) being immersed in dry methanol (MeOH) at 25 °C.

A4. Chapter 4 Experimental Section

A4.1. Materials and methods

The ligands uracil-1-acetic acid (UAcOH) and 5-fluorouracil-1-acetic acid (5-FUAcOH) were synthesized as described in the literature[13,14].

Magnetism. Magnetic measurements were carried out in a Quantum Design MPMS-XL-5 SQUID magnetometer in the 2-300 K temperature range with an applied magnetic field of 0.1 T on polycrystalline samples of compounds CP2 and CP2n (with masses of 7.009 and 30.889 mg, respectively) and CP3 and CP3n (with masses of 6.551 and 15.619 mg respectively). The susceptibility data were corrected for the sample holders, previously measured under the same conditions, and for the diamagnetic contributions as deduced by using Pascal´s constant Tables[3].

Electrochemistry. Electrochemical measurements were carried out with an AUTOLAB electrochemistry system in a three-electrode cell under N_2 atmosphere. A glassy carbon working electrode, a Pt gauze as the counter electrode, and a Ag/AgCl/KCl 3 M reference electrode were used. Typically, 4 mL of biological medium (RPMI or DMEM) were added to the cell, and cyclic voltammetry (CV) was carried out to check the background, which in both cases showed a -1.9 V to +1.2 V potential window where the studies with the analyte could be made. Then, a 1 mL of colloidal suspension of CP2n or CP3n was added to carry out the CV measurements. The final concentration was 5 mM.

Inductively Coupled Plasma Mass Spectrometry. ICP-MS was done in a Perkin-Elmer NexION 300XX ICP-MS.

A4.2. Experimental procedures

A4.2.1. Synthesis of CP2

A mixture of $Cu(NO_3)_2 \cdot 3H_2O$ (100 mg, 0.41 mmol), UAcOH (141 mg, 0.82 mmol) and 4,4'-bipy (65 mg, 0.41 mmol) was stirred in 18 mL of water (initial pH = 2.30) for 10 min at 25 °C. The resulting purple suspension was heated at 120 °C for 3 days in a solvothermal reactor and cooled down to 30 °C with a rate of 0.05 °C min^{-1} (final pH = 2.57). Purple and turquoise crystals were obtained and separated by hand. The turquoise crystals were identified as a previously reported coordination polymer with formula $[Cu_2(UAcO)_2(C_2O_4)(4,4'\text{-bipy})] \cdot 2H_2O$[15]. The purple crystals were washed with water and dried in air (190 mg, 43 % yield based on Cu). Elemental analysis calculated for $C_{44}H_{42}Cu_2N_{12}O_{19}$ (**CP2**): C: 45.17 %, H: 3.59 %, N: 14.37 %. Found: C: 44.84 %, H: 3.64 %, N: 14.06 %. IR selected data (cm^{-1}): 3450 (w), 3100 (w), 3053 (w), 1666 (s), 1630 (s), 1610 (s), 1467 (m), 1391 (s), 1345 (m), 1300 (m), 1239 (m), 1203 (m), 1076 (w), 965 (w), 812 (s), 756 (m), 721 (m), 644 (m).

A4.2.2. Synthesis of CP2n

A mixture of UAcOH (141 mg, 0.82 mmol) in 4 mL of water and NaOH (33 mg, 0.82 mmol) in 3 mL of water was added to a water suspension (4 mL) of 4,4'-bipy (65 mg, 0.41 mmol) under stirring at 5 °C. The

resulting white suspension turned onto a purple colloid upon the addition of 3 mL of an aqueous solution of $Cu(CH_3COO)_2 \cdot H_2O$ (82 mg, 0.41 mmol). The purple colloid was stirred for 5 min at 1200 rpm, centrifuged for 3 min at 5000 rpm, and washed four times with 14 mL of Milli-Q water every time. The solid was dried in air (180 mg, 38 % yield based on Cu). Elemental analysis calculated for $C_{44}H_{42}Cu_2N_{12}O_{19}$ (**CP2n**): C: 45.17 %, H: 3.59 %, N: 14.37 %. Found: C: 44.81 %, H: 3.67 %, N: 14.14 %. IR selected data (cm^{-1}): 3490 (w), 3104 (w), 3059 (w), 1676 (s), 1626 (s), 1606 (s), 1433 (m), 1390 (s), 1348 (m), 1297 (m), 1233 (m), 1203 (m), 1075 (w), 967 (w), 813 (s), 762 (m), 727 (m), 642 (m).

A4.2.3. Synthesis of CP3

A mixture of $Cu(NO_3)_2 \cdot 3H_2O$ (100 mg, 0.41 mmol), 5-FUAcOH (150 mg, 0.82 mmol) and 4,4'-bipy (65 mg, 0.41 mmol) was stirred in 18 mL of water (initial pH = 2.68) for 10 min at 25 °C. The resulting purple suspension was heated at 120 °C for 2 days in a solvothermal reactor and cooled down to 30 °C with a rate of 0.05 °C min^{-1} (final pH = 2.54). A low amount of unstable yellow crystals and deep purple crystals were obtained. The purple crystals were separated by hand, washed with water and dried in air (40 mg, 7.3 % yield based on Cu). Elemental analysis calculated for $C_{44}H_{48}Cu_2N_{12}O_{24}F_4$ (**CP2n**): C: 39.67 %, H: 3.61 %, N: 12.62 %. Found: C: 40.52 %, H: 3.66 %, N: 11.93 %. IR selected data (cm^{-1}): 3498 (w), 3171 (w), 3063 (w), 2823 (w), 1700 (s), 1661 (s), 1635 (s), 1602 (s), 1495 (w), 1475 (w), 1413 (m), 1398 (s), 1381 (s), 1368 (s), 1342 (m), 1320 (m), 1300 (s), 1241 (s), 1190 (w),

1144 (m), 1073 (m), 985 (m), 898 (m), 813 (s), 798 (s), 762 (m), 698 (m), 642 (m).

A4.2.4. Synthesis of CP3n

A mixture of 5-FUAcOH (150 mg, 0.82 mmol) in 4 mL of water and NaOH (32 mg, 0.82 mmol) in 3 mL of water was added to a water suspension (4 mL) of 4,4'-bipy (65 mg, 0.41 mmol) under stirring at 5 °C. The resulting white suspension turned onto a purple colloid upon the addition of 3 mL of an aqueous solution of $Cu(NO_3)_2 \cdot 3H_2O$ (100 mg, 0.41 mmol). The purple colloid was stirred for 5 min at 1200 rpm, centrifuged for 3 min at 5000 rpm, and washed four times with 14 mL of Milli-Q water every time. The solid was dried in air (78 mg, % yield based on Cu). Elemental analysis calculated for $C_{44}H_{48}Cu_2N_{12}O_{24}F_4$ (**CP3n**): C: 39.67 %, H: 3.61 %, N: 12.62 %. Found: C: 39.67 %, H: 3.58 %, N: 12.42 %. IR selected data (cm^{-1}): 3492 (w), 3104 (w), 3059 (w), 1675 (s), 1626 (s), 1603 (s), 1431 (m), 1389 (s), 1348 (m), 1297 (m), 1233 (m), 1201 (m), 1075 (w), 967 (w), 813 (s), 764 (m), 727 (m), 641 (m).

A4.2.5. Structural studies of SCXRD

During the crystal structure solution, it became evident that the uracil residues were disordered. All the attempts to solve the crystal structures using lower symmetry space groups did not avoid the presence of this disorder. The disorder was modelled by placing the uracil residues over two positions related by a rotation of 180°. The atoms belonging to the disordered part were kept isotropic, and soft

"SADI" restraints were fixed in order to ensure that the bond distances in both parts of the disordered uracil residues are similar. In the crystal structure of **CP3** the disorder affected the 4,4'-bipy ligand, which is disordered over two positions related by a rotation of 18.95° around the N31···N40 axis. In both crystal structures, there are voids occupied by disordered water molecules that were impossible to model in the case of **CP2** (their contribution was removed using the squeeze procedure as implemented in PLATON) and were modelled as a set of seven hydrogen-bonded water molecules disordered in two arrangements related by a symmetry centre.

In both crystal structures, the hydrogen atoms were included in their calculated positions and refined riding on the respective parent atoms, except those belonging to the disordered water molecules. All calculations were performed using the WINGX crystallographic software package[4]. Details of the structure determination and refinement are summarized in Table A4.1.

Table A4.1. Single-crystal data and structure refinement details for compounds **CP2** and **CP3**[a]

	CP2	**CP3**
Empirical formula	$C_{22}H_{24}CuN_6O_{11}$	$C_{22}H_{23}CuF_2N_6O_{11.25}$
*M*r	612.01	657.00
Crystal system	Triclinic	Monoclinic
Space group	$P\bar{1}$	*C2/c*
a/Å	10.2489(6)	17.3204(13)
b/Å	10.3638(5)	11.0969(6)

c/Å	15.0581(9)	27.933(2)
α/º	105.732(3)	90
β/º	96.365(3)	96.920(4)
γ/º	114.941(3)	90
V/Å3	1348.68(14)	5329.6(6)
Z	2	8
*D*c/Mg.m^{-3}	1.507	1.63
Color	Blue	Clear violet
Crystal habit	Prismatic	Plate
Crystal size/mm^3	0.14 x 0.06 x 0.02	0.12 x 0.09 x 0.02
μ/mm^{-1}	0.878	0.907
2ϑ max/º	50.70	50.70
Reflections collected	23534	47354
Independent reflections	4921	4880
*R*int	0.0652	0.1075
Variable parameters	322	362
*R*1[I>2σ(I)]/*wR*2[all data][a)]	0.0681/0.2098	0.0690/0.2183
Goodness-of-fit (*F*2)	1.063	1.030
$\Delta\rho_{max}/_{min}$/e Å^{-3}	0.967, -0.548	1.473, -0.599

[a] $R_1 = \Sigma\ ||F_o| - |F_c|| \ / \ \Sigma\ |F_o|$; $wR_2 = [\Sigma[w(F_o^2 - F_c^2)^2] \ / \ [\Sigma(F_o^2)^2]]^{1/2}$ where $w = 1/[\sigma^2(F_o^2)+(aP)^2+(bP)]$ with a = 0.0645 (**CP2**), 0.1222 (**CP3**) and b = 0.0000 (**CP2**), 31.8951 (**CP3**).

Table A4.2. Selected bond lengths (Å) and angles (°) for compounds **CP2**[a]

Cu1-N11	1.998(4)	Cu1-O91	1.983(4)
Cu1-N20^{i}	1.999(4)	Cu1-O91^{ii}	2.424(3)
Cu1-O81	1.945(4)		

Cu1···Cu1^{ii}	3.4179(13)	Cu1···Cu1^{iii}	11.0846(6)
N11-Cu1-N20^{i}	172.86(17)	N20^{i}-Cu1-O91	90.91(16)
N11-Cu1-O81	91.30(17)	N20^{i}-Cu1-O91^{ii}	94.50(15)
N11-Cu1-O91	91.41(16)	O81-Cu1-O91	171.35(15)
N11-Cu1-O91^{ii}	92.58(15)	O81-Cu1-O91^{ii}	92.93(14)
N20^{i}-Cu1-O81	87.39(17)	O91-Cu1-O91^{ii}	78.74(14)

[a]Symmetry codes for **CP2**: (i) x, y, z-1; (ii) 3/2-x, 1/2-y, z; (iii) 3/2-x, 1/2-y, 1+z.

Table A4.3. Hydrogen bonding interactions (Å, °) in compound **CP2**[a]

D-H···A	**H···A**	**D···A**	**D-H···A**
N3C-H···O82^{i}	2.11	2.946(8)	164.8
C5C-H···O2A^{ii}	2.55	3.324(11)	140.6
C5B-H···O4B^{iii}	2.43	3.31(2)	157.5
C13-H···O92^{i}	2.44	3.249(6)	145.8
C18-H···O92^{i}	2.39	3.268(7)	156.7
C21-H···O2C^{iv}	2.57	3.360(7)	142.6

[a]Symmetry codes for **CP2**: (i) -x+1, -y+1, -z+1; (ii) -x+2, -y+2, -z+1; (iii) -x+2, -y, -z; (iv) -x+1, -y, -z+1.

Table A4.4. Selected bond lengths (Å) and angles (°) for compound **CP3**[a]

Cu1-N31	2.014(4)	Cu1-O281	1.977(4)
Cu1-N40^{i}	2.006(4)	Cu1-O281^{ii}	2.400(3)
Cu1-O181	1.942(4)		
Cu1···Cu1^{ii}	3.3958(13)	Cu1···Cu1^{iii}	11.0969(6)
N31-Cu1-N40^{i}	173.15(19)	N40^{i}-Cu1-O281	91.79(16)
N31-Cu1-O181	91.73(16)	N40^{i}-Cu1-O281^{ii}	94.43(15)
N31-Cu1-O281	90.01(16)	O181-Cu1-O281	170.82(15)

N31-Cu1-O281^{ii}	92.40(15)	O181-Cu1-O281^{ii}	92.28(15)
N40^{i}-Cu1-O181	87.53(16)	O281-Cu1-O281^{ii}	78.64(14)

[a]Symmetry codes for **CP3**: (i) x, y-1, z; (ii) -x+1, y, -z+3/2; (iii) x, y-1, z.

Table A4.5. Hydrogen bonding interactions (Å, °) in compound **CP3**[a]

D-H···A	H···A	D···A	D-H···A
N13-H···O14^{i}	2.01	2.867(7)	168.4
N23-H···O182^{ii}	2.00	2.819(8)	156.8
C26-H···O6w^{iii}	2.53	3.39(2)	153.1
C27-H···O6w^{iii}	2.54	3.41(2)	148.1
C38A-H···O282^{iv}	2.35	3.275(14)	168.8
C41A-H···O22^{v}	2.51	3.290(18)	140.1

[a]Symmetry codes for **CP3**: (i) -x+1/2, -y+1/2, -z+1; (ii) -x+3/2, y-1/2, -z+3/2; (iii) -x+3/2, -y+3/2, -z+2; (iv) -x+3/2, y+1/2, -z+3/2; (v) –x+1, y+1, -z+3/2.

A4.2.6. SEM sample preparation

The surfaces used for FESEM were SiO_2 300 nm thickness (IMS Company). SiO_2 surfaces were cleaned by ultrasonication at 37 KHz and 380 W in acetone for 15 min and in 2-propanol for another 15 min, and then dried under an argon flow.

Diluted suspensions of compound **CP2n** and **CP3n** were prepared by adding 100 µL of each purple colloid over 500 µL of Milli-Q water. 10 µL of the diluted suspension were deposited on SiO_2 substrates by drop casting deposition for 15 min at room temperature, and then dried under argon flow.

A4.2.7. AFM sample preparation

The surfaces used for FESEM were SiO_2 300 nm thickness (IMS Company). SiO_2 surfaces were cleaned by ultrasonication at 37 KHz and 380 W in acetone for 15 min and in 2-propanol for another 15 min, and then dried under an argon flow.

Diluted suspensions of compound **CP2n** and **CP3n** were prepared by adding 100 µL of each purple colloid over 500 µL of Milli-Q water. 15 µL of the diluted suspension were deposited on SiO_2 substrates by drop casting deposition for 15 min at room temperature, and then dried under argon flow.

A4.2.8. Cell culture

Human pancreatic adenocarcinoma (Panc-1) cells were obtained from American Type Culture Collection (ATCC)®, and human uveal melanoma (Mel202) cells were provided from the University of California, San Francisco, from Dr. Susana Ortiz-Urda laboratory.

Panc-1 cells were grown in Dulbecco's modified Eagle's medium (DMEM), while Mel202 cells were cultured in RPMI 1640 medium. Both cell culture mediums were supplemented with 10 % (v/v) fetal bovine serum (FBS), 2 mM L-Glutamine, and 1 % Penicillin/Streptomycin. All experiments were carried out on subconfluent cells incubated at standard conditions (37 °C, 5 % CO_2).

A4.2.9. Cytotoxicity assay

Uveal Melanoma (Mel 202) cell line and pancreatic cancer cells (Panc-1) were seeded in 24 well plates and incubated at standard

conditions. Then, the cells were incubated with the corresponding compound for 24 h at different concentrations: CP2n, CP3n, 4,4'-bipy and UAcOH (1-200 µM); $Cu(AcO)_2$ (2.04-408 µM); and 5-FU and 5-FUAcOH (3.9-788 µM). After incubation, the culture medium was removed, and cells were washed twice with PBS 1X. Toxicity was measured 48 h after treatment, using resazurin assay following the manufacture's protocol[16]. Briefly, the cell culture medium was replaced with a fresh culture medium containing 1 % of resazurin solution (1 mg mL^{-1} in PBS), and cells were incubated for 3 h more at 37 °C, 5 % CO_2. Fluorescence was measured using a microplate reader (λ_{exc} = 550/20 nm, λ_{em} = 590/20 nm). Data corresponded to mean values ± standard deviation. For statistical calculations, one-way ANOVA and Tukey's Test in R Commander Software was used[17]. P values < 0.05 (*), < 0.01 (**) and < 0.001 (***) were considered as statistically significant .

A4.2.10. ROS generation assay

Cells were plated in 96-well plates (15×10^3 cells $well^{-1}$) and incubated at standard conditions. Then, cells were treated with different concentrations of **CP2n** and **CP3n** for 24 h and washed twice with fresh medium and further incubated 24 h. Then, cells were incubated with 5 µM of 2',7'-dichlorofluorescein, (H_2DCFDA) for 30 min at 37 °C, 5 % CO_2. Finally, cells were washed twice with 1X PBS (pH 7.4), and the fluorescence was measured using a microplate reader (λ_{exc} = 485/20 nm, λ_{em} = 535/20 nm). Values were normalized with the results of the cell viability assay. Data represent the mean values ± standard deviation. For statistical calculations, one-way ANOVA and Tukey's Test in R Commander Software was used[17]. P values < 0.05

(*), < 0.01 (**) and < 0.001 (***) were considered as statistically significant.

A4.3. Additional Data

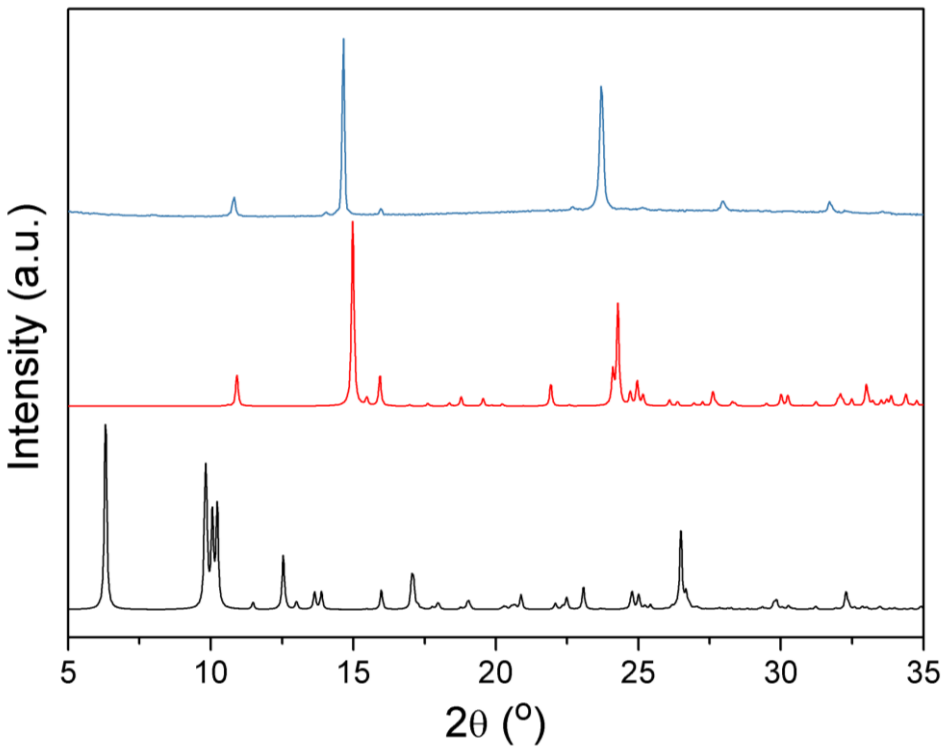

Figure A4.1. X-ray powder diffraction patterns of light green solid obtained after 48h in DMEM and RPMI (blue line), simulated data of coordination complex $[Cu(UAcO)_2(H_2O)_4]\cdot H_2O$ (red line) and simulated data of coordination polymer $[Cu_2(UAcO)_4(4,4'\text{-bipy})_2]_n\cdot 3H_2O$ (**CP2n**) (black line).

A5. Chapter 5 Experimental Section

A5.1. Materials and methods

The ligand uracil-1-acetic acid (UAcOH) was synthesized as described in the literature[13].

Nitrogen adsorption. N_2 (77 K) physisorption data were measured on outgassed samples with a Quantachrome Autosorb-iQ-MP. True density of outgassed samples was determined by an automatic helium microultrapycnometer of Quantachrome Instruments. In both cases the outgassing of the samples was conducted by subjecting the samples to 333 K under vacuum for 46 h. A INSTRON 5967 testing device with a 20 N load cell was used to record compression-strain curves using cylindrical specimens of an approximated diameter of 20–25 mm and a length of 10 to 13 mm. Test pieces were compressed to a maximum stress of 18 N at a rate of 5 mm min^{-1}.

A5.2. Experimental procedures

A5.2.1. Synthesis of CP4

A mixture of UAcOH (140 mg, 0.82 mmol) in 4 mL of water and NaOH (33 mg, 0.82 mmol) in 3 mL of water was added to a water solution (4 mL) of 4,4’-bipy (64 mg, 0.41 mmol) under stirring at room temperature. The resulting clear solution turned onto a purple colloid upon addition of 3 mL of water solution of $Cu(CH_3COO)_2 \cdot H_2O$ (82 mg, 0.41 mmol) (pH = 5.8). The purple colloid, which correspond to $[Cu_2(UAcO)_4(4,4'\text{-bipy})_2]_n \cdot 3H_2O$ 1D coordination polymer (**CP2n**, 38 %

yield), was stirred for 1 hour at 1200 rpm and the mixture filtered off. Dark blue crystals of **CP4** were isolated, from the mother liquor upon standing 1 week at 20°C. Then, the dark blue crystals were filtered, washed with water, and dried in air (0.056 mg, 15 % yield based on Cu). Elemental analysis calculated for $C_{18}H_{22}CuN_4O_9$ (**CP4**): C: 45.92 %, H: 4.00 %, N: 11.80 %. Found: C: 44.14 %, H: 4.18 %, N: 11.93 %. IR selected data (cm^{-1}): 3425 (w), 3092 (w), 3058 (w), 1671 (s), 1607 (s), 1460 (m), 1377 (s), 1328 (s), 1250 (m), 1220 (m), 1078 (m), 961 (m), 814 (s), 764 (m), 725 (m), 676 (m), 637 (m).

A5.2.2. Synthesis of CP4n and CP4-MOG

A mixture of 4,4'-bipy (64 mg, 0.41 mmol) in CH_3COOH (0.07 mL, 1.23 mmol) was added to a solution of UAcOH (70 mg, 0.41 mmol) in 4 mL of water and NaOH (16.4 mg, 0.41 mmol) in 3 mL of water. The resulting solution turned onto a purple colloid (**CP4n**) upon addition of 3 mL of an aqueous solution of $Cu(CH_3COO)_2{\cdot}H_2O$ (82 mg, 0.41 mmol) (pH = 4.5). The optimum hydrogel of CP4n, **CP4-MOG**, is formed upon stirring the **CP4n** purple colloid for 20 min in the ultrasound bath (37 KHz, 380 W) and leaving the sample 24h at room temperature. X-ray powder diffraction confirm the phase purity of the sample **CP4n**.

A5.2.3. Synthesis of CP4-MOA and CP4-MOX

Metal Organic Xerogel (**CP4-MOX**) was prepared drying **CP4-MOG** in open-atmosphere. (0.142 mg, 69 % yield based on Cu). IR selected data (cm^{-1}): 3425 (w), 3092 (w), 3058 (w), 1671 (s), 1607 (s), 1460 (m), 1377 (s), 1328 (s), 1250 (m), 1220 (m), 1078 (m), 961 (m), 814 (s), 764 (m), 725 (m), 676 (m), 637 (m).

To prepare the metal-organic aerogel (**CP4-MOA**), an E3100 critical point dryer from Quorum Technologies equipped with gas inlet, vent, and purge valves, and with a thermal bath, was employed. First, several solvent exchanges cycles were performed in the **CP4-MOG** to replace water solvent by ethanol. Then, the metallogel was immersed in liquid CO_2 at 293 K and 50 bar for 1 hour. Then, the exchanged ethanol was removed through the purge valve. This process was repeated five times. Subsequently, the sample was dried under supercritical conditions, increasing the temperature and pressure to 313 K and 85−95 bar. Finally, under constant temperature (313 K), the chamber was slowly vented up to atmospheric pressure to achieve **CP4-MOA** (0.158 mg, 77 % yield based on Cu). IR selected data (cm^{-1}): 3425 (w), 3092 (w), 3058 (w), 1671 (s), 1607 (s), 1460 (m), 1377 (s), 1328 (s), 1250 (m), 1220 (m), 1078 (m), 961 (m), 814 (s), 764 (m), 725 (m), 676 (m), 637 (m).

A5.2.4. Structural studies of SCXRD

Crystal parameters and details of the final refinements of compound **CP4** are summarized in Table A5.1. The hydrogen atoms were included in their calculated positions and refined riding on the respective carbon atoms. All calculations were performed using the WINGX crystallographic software package[4].

Table A5.1. Single-crystal data and structure refinement details for compound **CP4**

Empirical formula	$C_{18}H_{22}CuN_4O_9$
Mr	501.93
Crystal system	Orthorhombic
Space group	*Fdd2*
a/Å	21.561(3)
b/Å	35.637(5)
c/Å	11.1216(17)
V/Å^3	8545(2)
Z	16
*D*c/Mg.m^{-3}	1.561
Color	Dark blue
Crystal habit	Platy
Crystal size/mm^3	0.37 x 0.18 x 0.02
μ/mm^{-1}	1.081
$2\theta_{max}$/°	50.69
Reflections collected	21054
Independent reflections	3823
R_{int}	0.1207
Variable parameters	290
R_1[I>2σ(I)]/wR_2[all data][a]	0.0570/0.1089
Goodness-of-fit (F^2)	1.034
$\Delta\rho_{max/min}$/e Å^{-3}	0.709, -0.491

[a] $R_1 = \Sigma\,||F_o| - |F_c||\,/\,\Sigma\,|F_o|$; $wR_2 = [\Sigma[w(F_o^2 - F_c^2)^2]\,/\,[\Sigma(F_o^2)^2]]^{1/2}$ where $w = 1/[\sigma^2(F_o^2)+(aP)^2+(aP)]$ with a = 0.0645 (**CP4n**), and b = 0.0000 (**CP4n**).

A5.2.5. SEM sample preparation

The surfaces used for FESEM were SiO_2 300 nm thickness (IMS Company). SiO_2 surfaces were cleaned by ultrasonication at 37 KHz and 380 W in acetone for 15 min and in 2-propanol for another 15 min, and then dried under an argon flow.

Diluted suspensions of compound **CP4n** were prepared by adding 20 µL of each purple colloid over 400 µL of Milli-Q water. 10 µL of the diluted suspension were deposited on SiO_2 substrates by drop casting deposition for 15 min at room temperature, and then dried under argon flow. Small fragments of **CP4-MOA** and **CP4-MOX** were deposited directly over carbon tape.

A5.2.6. AFM sample preparation

The surfaces used for FESEM were SiO_2 300 nm thickness (IMS Company). SiO_2 surfaces were cleaned by ultrasonication at 37 KHz and 380 W in acetone for 15 min and in 2-propanol for another 15 min, and then dried under an argon flow.

Diluted suspension of compound **CP4n** were prepared by adding 20 µL of purple colloid suspension over 400 µL of Milli-Q water. Suspensions of 9.5 mg of **CP4-MOA** in 1 mL of Milli-Q water and 6.5 mg of **CP4-MOX** in 1 mL of Milli-Q water were also prepared. The corresponding mixtures were stirred for 5 seconds. 15 µL of the diluted suspension were deposited on SiO_2 substrates by drop casting

deposition for 15 min at room temperature, and then dried under argon flow.

A5.2.7. Mechanical compression test

An INSTRON 5967 testing device with a 20 N load cell was used to record compression-strain curves of cylindrical aerogel specimens. Physical features of the tested samples are gathered in Table A5.2. All specimens were compressed to a maximum force of 18 N at a rate of 5 mm min^{-1}, without exhibiting failure upon the explored range.

Stress-strain curves are gathered in Figure A5.1, while Young modulus curve fitting and data are gathered in Figure A5.1 and Table A5.3.

Table A5.2. Physical features of **CP4-MOA** specimens of compression tests.

Sample	Mass (g)	Shape	H (mm)	D (mm)	A (mm^2)	V (cm^3)	ρ ($g \cdot cm^3$)
46	0.0760	cylinder	10.6	20.1	317.3	3.347	0.0227
49	0.1596	cylinder	12.6	24.5	471.4	4.849	0.0329
50	0.1593	cylinder	11.9	25.0	492.1	4.679	0.0340

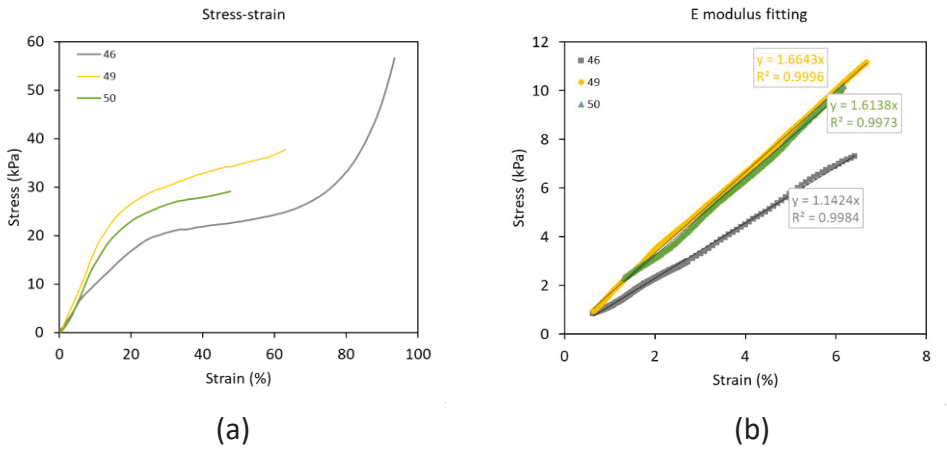

Figure A5.1. (a) Compression-strain curves performed on **CP4-MOA** specimens. (b) Corresponding fittings for the estimation of the Young's modulus.

Table A5.3. Elastic modulus of CP4-MOA specimens.

Sample	E (kPa)	$E_{specific}$ (kPa·m^3·Kg^{-1})
46	114.24	5.03
49	166.43	5.06
50	170.99	5.02

A5.2.8. N_2 adsorption experiments

All physisorption measurements were performed on a Quantachrome Autosorb-iQ-MP. Prior to N_2 adsorption measurements all samples where outgassed under vacuum at 50 °C for 6 hours. Figure 5.9 shows the N_2 adsorption isotherms at 77 K, while the subtracted adsorption data is gathered in Table A5.4. All curves resemble a type II isotherm indicative of a dominating

macroporosity. The sample exhibits certain contribution of microporosity which can be ascribed to the presence of narrow interlamellar cavities in the aerogel microstructure.

Table A5.4. Surface area, lamella thickness and pore volume data

Sample	S_{BET} [a] (m^2g^{-1})	$D_{lamella}$ [b] (nm)	S_{micro} [c] (m^2g^{-1})	V_{micro} [c] (cm^3g^{-1})	V_T [d] (cm^3g^{-1})
CP4-MOA	21.1	52.08	1.4	<0.001	0.088

[a]BET specific surface area. [b]lamella thickness; see calculation details below. [c]micropore surface area (S_{micro}) and volume (V_{micro}) are estimated from the *t*-plot calculation. [d]total specific pore volume (V_T) are computed at P/P_0 = 0.93 and 0.99 to account for pores smaller than 50 and 200 nm, respectively.

Calculation of lamella thickness

As the coordination polymer lacks intrinsic porosity, the specific surface area (S_T) can be approached as the product of the number of particles per sample gram (Np) and the particle mean area (Sp) (Equation 1)[18]. Since the number of particles can be calculated from the ratio between specific sample volume and particle mean volume (Vp) Equation 1 can be rewritten as Equation 2, where the specific volume has been replaced by the specific density (ρ).

$$S_T = S_p x N_p \qquad \textit{Equation 1}$$

$$S_T = \frac{S_p}{\rho \cdot V_p} \qquad \textit{Equation 2}$$

When particles are spherical or resemble regular polyhedrons, particle diameter or size can directly be derived. In principle it is not a useful equation for irregular polyhedrons as they are defined by

more than one variable parameter, unless certain approaches are made. In this sense, the lamellar shape of the nanocrystal comprising the aerogels, imply that the lateral dimensions (L1 and L2) are much greater than the the thickness ($d_{lamella}$). Thus, the contribution of the lamella edges to the particle area can be discarded and lamella thickness can stimated from Equation 3.

$$d_{lamella} = \frac{2}{\rho \cdot S_T} \qquad \textit{Equation 3}$$

Note that herein we used the density value measured by He picnometry (1.82 g·cm^3).

A5.3. Additional data

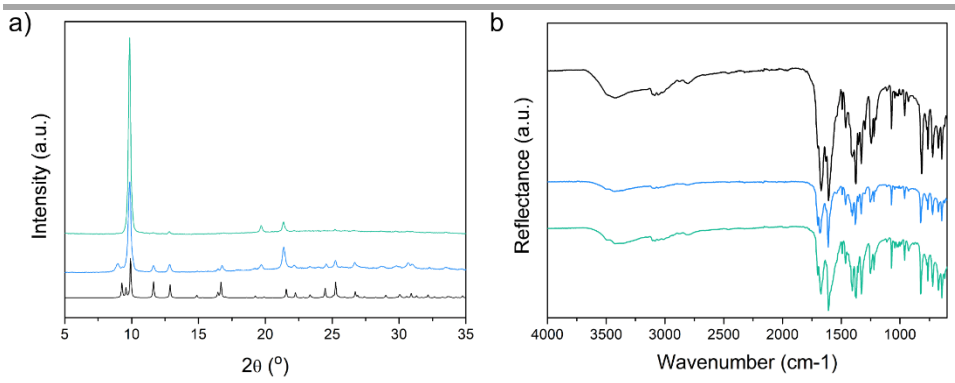

Figure A5.2. PXRD patterns and ATR-FT-IR spectra of **CP4n** (black line), **CP4-MOX** (blue line) and **CP4-MOA** (green line)

A5.3.1. Stability studies

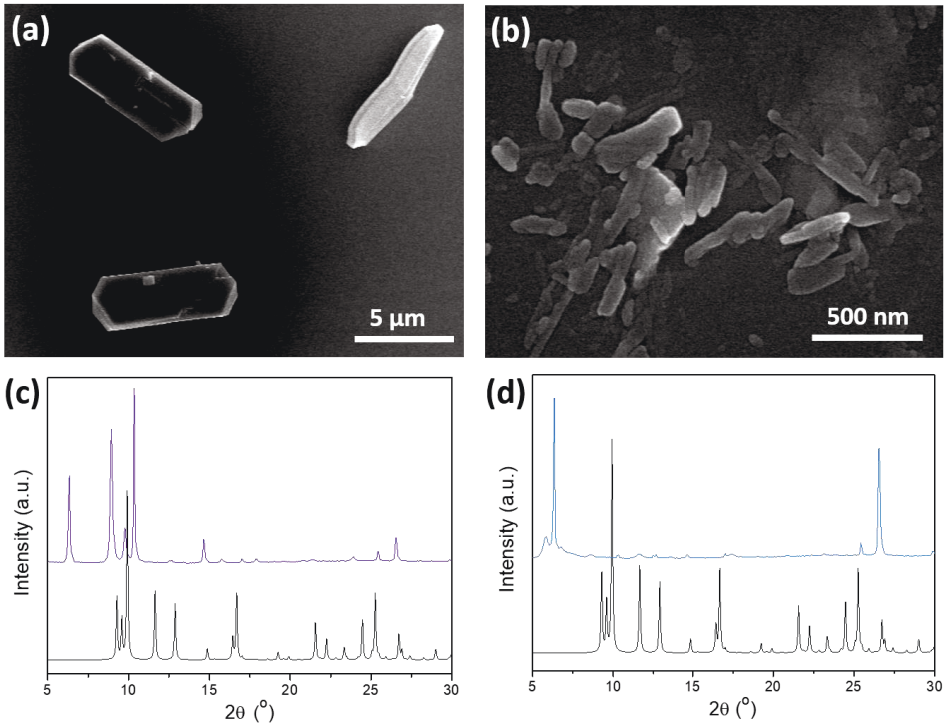

Figure A5.3. FESEM images of compound **CP4n** at: (a) pH = 4.5 and (b) at pH = 6.0. Compound **CP4n** is transformed after 24 hours at pH 4.5 and 6 (c-d). Compound **CP4n** was immersed in 3 mL of two buffer solutions at pH 4.5 and pH 6.5 during 24h.

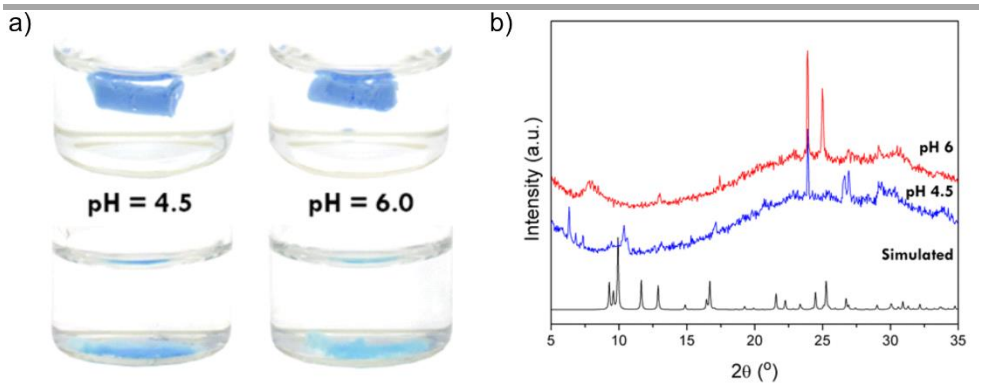

Figure A5.4. a) Fragments of compound **CP4-MOG** immersed at pH = 4.5 (left) and pH = 6.0 (right) buffer solutions at 25 °C recently prepared (up) and after 24h (down). **CP4-MOG** was immersed in 3 mL of two buffer solutions at pH = 4.5 and pH = 6.5 during 24h. b) PRXD patterns of **CP4-MOG** after 24h immersed at pH 4.5 (blue line) and pH 6.0 (red line) buffer solutions at 25 °C and simulated from single crystal structure of **CP4** (black line).

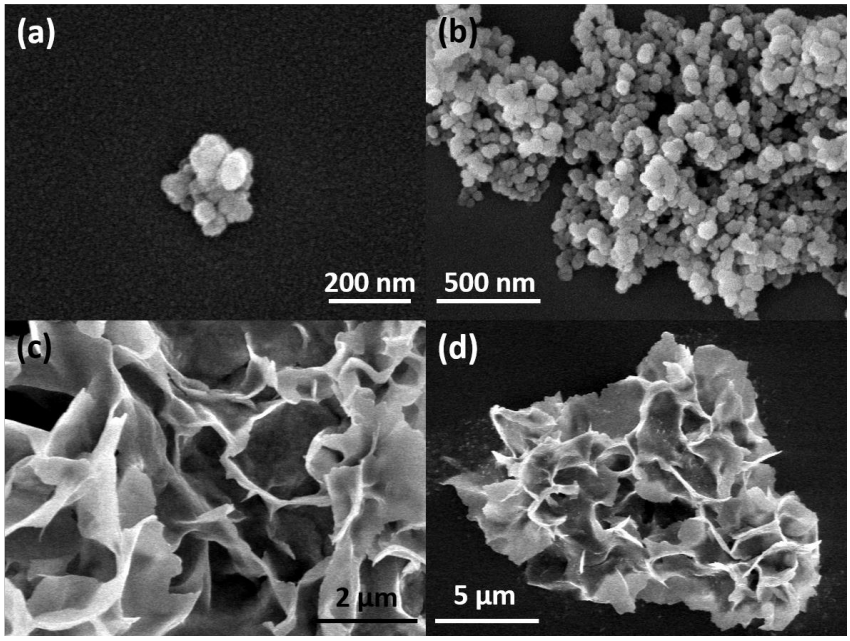

Figure A5.5. FESEM images of **CP4-MOG** after 24h immersed at pH 4.5 (a,b) and pH 6.0 (c,d) buffer solutions at 25 °C.

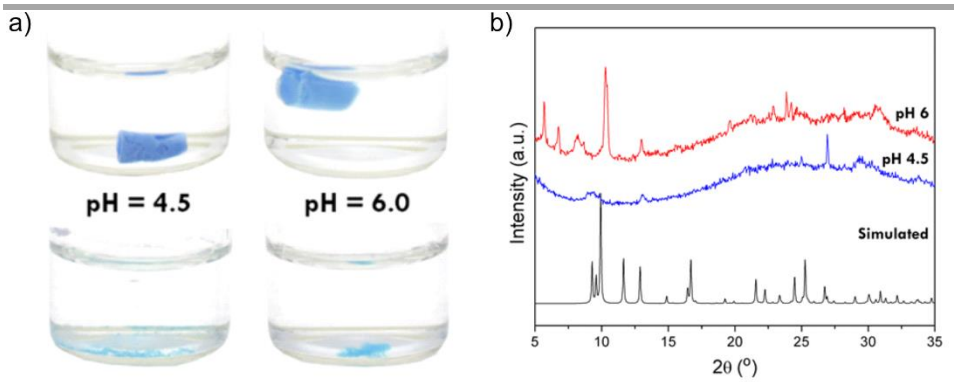

Figure A5.6. a) Fragments of compound **CP4-MOA** immersed at pH = 4.5 (left) and pH = 6.0 (right) buffer solutions at 25 ºC recently prepared (up) and after 24h (down). **CP4-MOA** was immersed in 3 mL of two buffer solutions at pH = 4.5 and pH = 6.5 during 24h. b) PRXD patterns of **CP4-MOA** after 24h immersed at pH 4.5 (blue line) and pH 6.0 (red line) buffer solutions at 25 ºC and simulated from single crystal structure of **CP4** (black line).

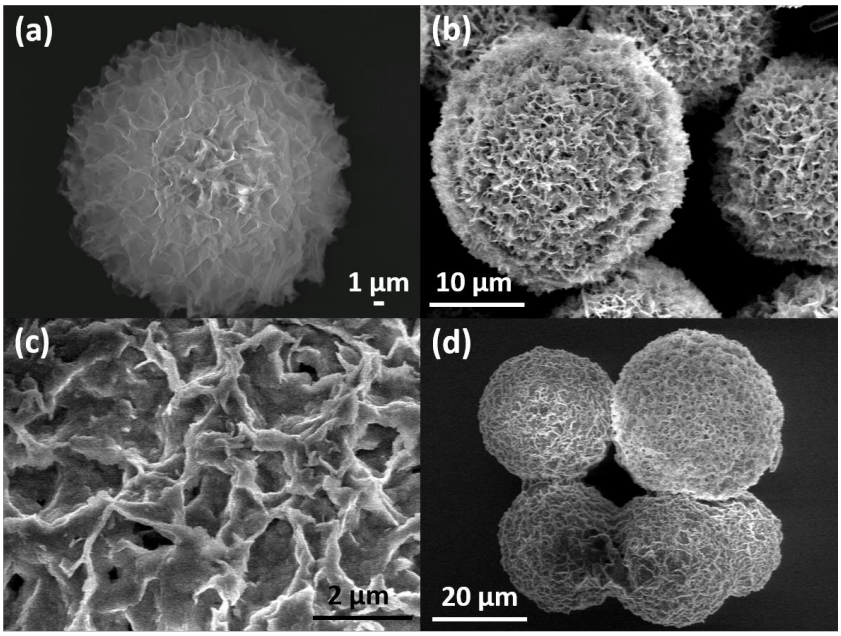

Figure A5.7. FESEM images of **CP4-MOA** after 24h immersed at pH 4.5 (a,b) and pH 6.0 (c,d) buffer solutions at 25 ºC.

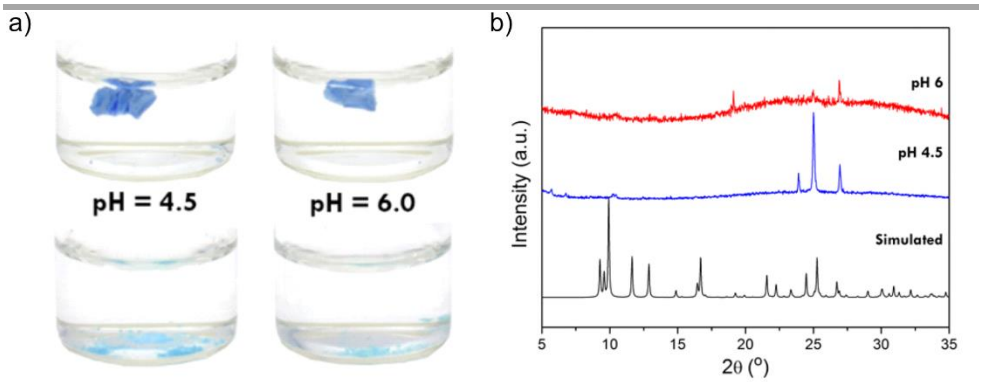

Figure A5.8. a) Fragments of compound **CP4-MOX** immersed at pH = 4.5 (left) and pH = 6.0 (right) buffer solutions at 25 ºC recently prepared (up) and after 24h (down). **CP4-MOX** was immersed in 3 mL of two buffer solutions at pH = 4.5 and pH = 6.5 during 24h. b) PRXD patterns of **CP4-MOX** after 24h immersed at pH 4.5 (blue line) and pH 6.0 (red line) buffer solutions at 25 ºC and simulated from single crystal structure of **CP4** (black line).

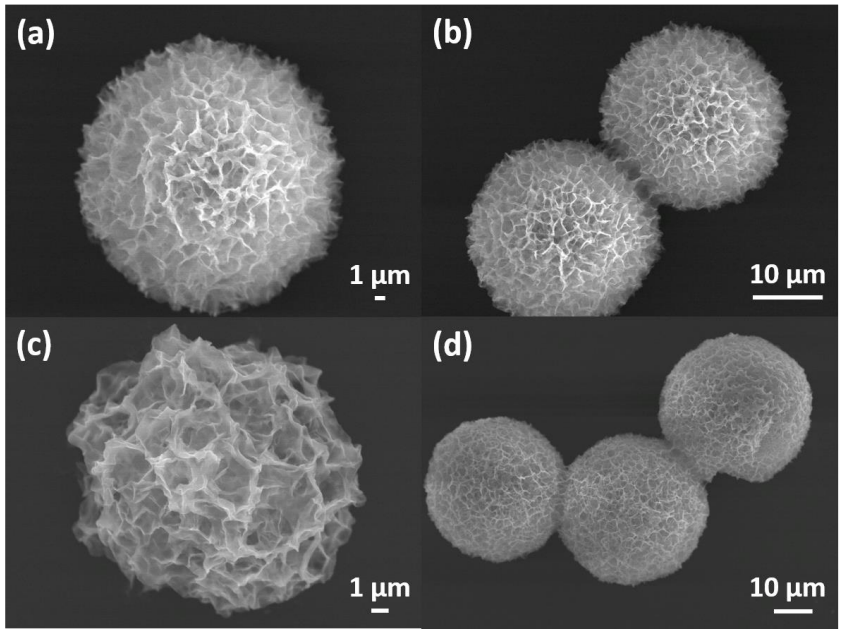

Figure A5.9. FESEM images of **CP4-MOX** after 24h immersed at pH 4.5 (a,b) and pH 6.0 (c,d) buffer solutions at 25 ºC.

Figure A5.10. CP4-MOG immersed in different solvents recently prepared (up) and after one week (down).

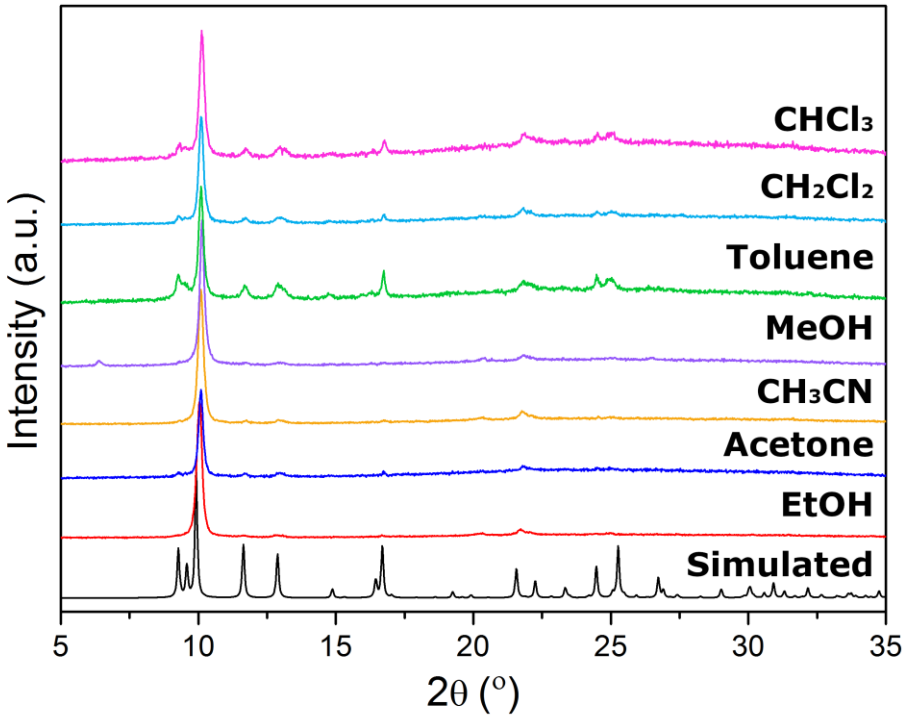

Figure A5.11. PXRD patterns of simulated and **CP4-MOG** after 1 week immersed in different solvents.

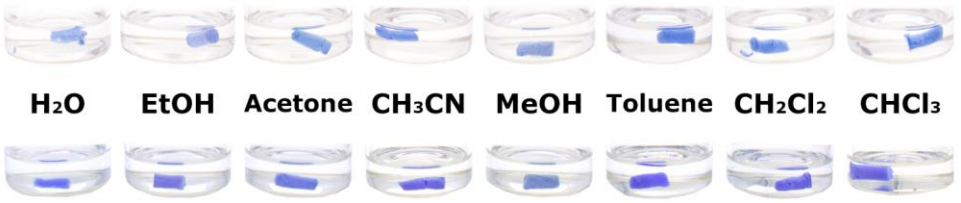

Figure A5.12. CP4-MOA immersed in different solvents recently prepared (up) and after one week (down).

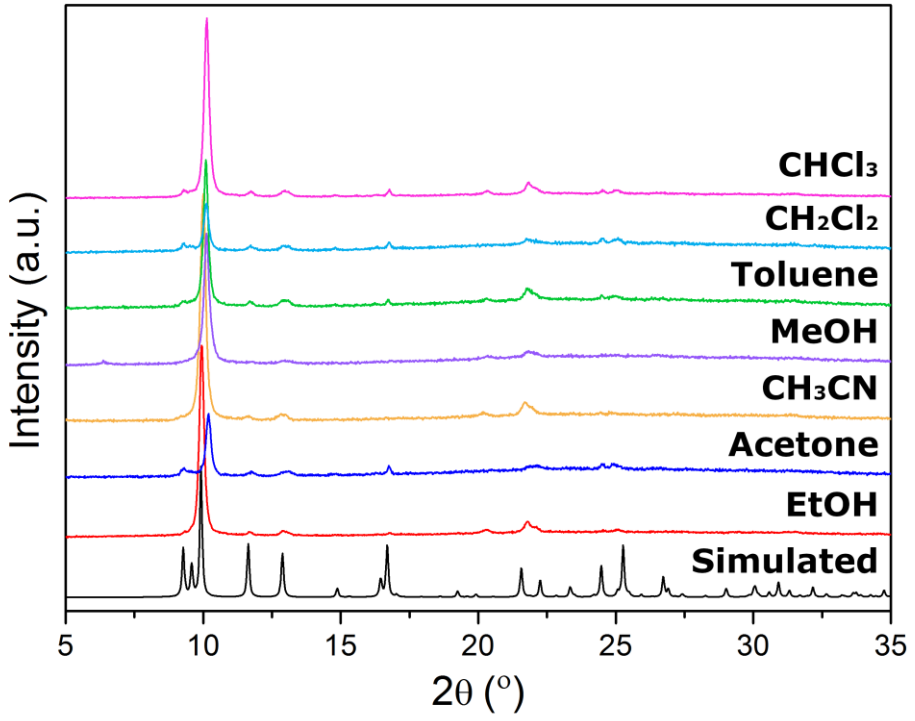

Figure A5.13. PXRD patterns of simulated and **CP4-MOA** after 1 week immersed in different solvents.

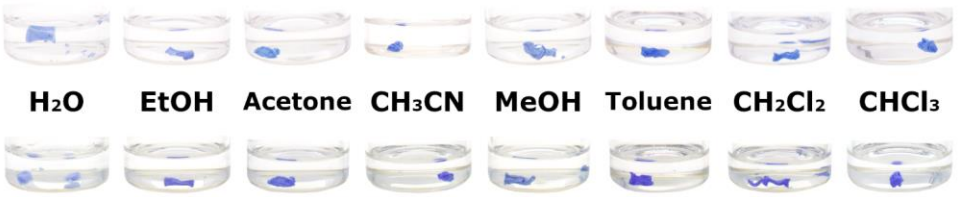

Figure A5.14. CP4-MOX immersed in different solvents recently prepared (up) and after one week (down).

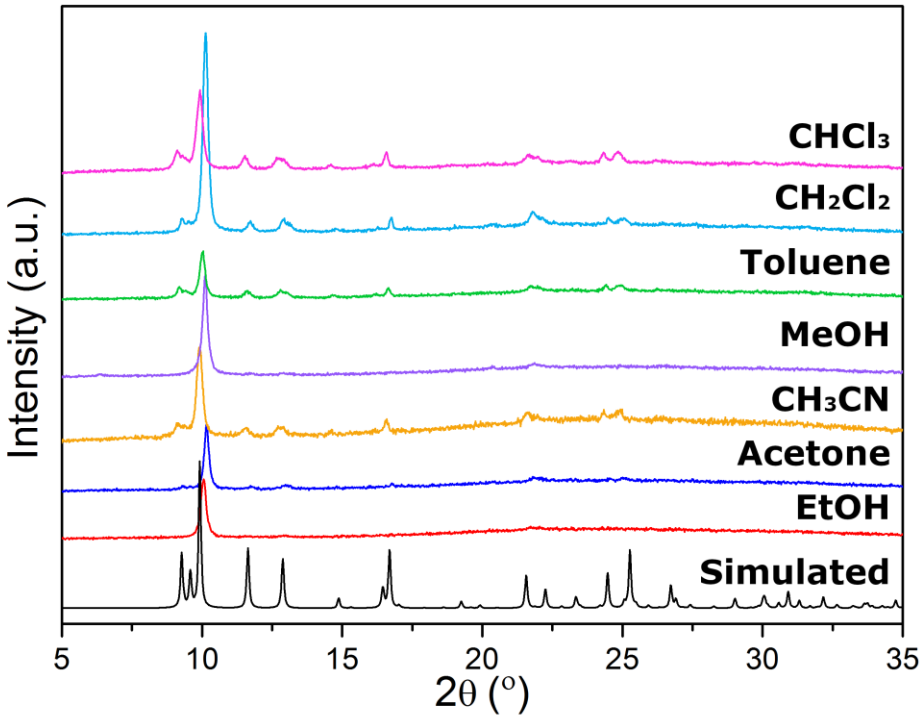

Figure A5.15. PXRD patterns of simulated and **CP4-MOX** after 1 week immersed in different solvents.

A6. References

1. Altomare, A., Cascarano, G., Giacovazzo, C. & Guagliardi, A. Completion and refinement of crystal structures with SIR 92. *J. Appl. Crystallogr.* **26**, 343–350 (1993).

2. Gruene, T., Hahn, H. W., Luebben, A. V., Meilleur, F. & Sheldrick, G. M. Refinement of macromolecular structures against neutron data with SHELXL2013. *J. Appl. Crystallogr.* **47**, 462–466 (2014).

3. Bain, G. A. & Berry, J. F. Diamagnetic Corrections and Pascal's Constants. *J. Chem. Educ.* **85**, 532 (2008).

4. Prakash, M. J. & Lah, M. S. Metal–organic macrocycles, metal–organic polyhedra and metal–organic frameworks. *Chem. Commun.* 3326 (2009). doi:10.1039/b902988e

5. Basham, M. *et al.* Data Analysis WorkbeNch (DAWN). *J. Synchrotron Radiat.* **22**, 853–858 (2015).

6. Juhás, P., Davis, T., Farrow, C. L. & Billinge, S. J. L. PDFgetX3 : a rapid and highly automatable program for processing powder diffraction data into total scattering pair distribution functions. *J. Appl. Crystallogr.* **46**, 560–566 (2013).

7. Segall, M. D. *et al.* First-principles simulation: ideas, illustrations and the CASTEP code. *J. Phys. Condens. Matter* **14**, 2717–2744 (2002).

8. Perdew, J. P., Burke, K. & Ernzerhof, M. Generalized Gradient Approximation Made Simple. *Phys. Rev. Lett.* **77**, 3865–3868 (1996).

9. Vanderbilt, D. Soft self-consistent pseudopotentials in a generalized eigenvalue formalism. *Phys. Rev. B* **41**, 7892–7895 (1990).

10. Monkhorst, H. J. & Pack, J. D. Special points for Brillouin-zone integrations. *Phys. Rev. B* **13**, 5188–5192 (1976).

11. Berne, B. J., Ciccotti, G. & Coker, D. F. *Classical and Quantum Dynamics in Condensed Phase Simulations*. *Front Mater* **13**, (WORLD SCIENTIFIC, 1998).

12. Macrae, C. F. *et al.* Mercury CSD 2.0 – new features for the visualization and investigation of crystal structures. *J. Appl. Crystallogr.* **41**, 466–470 (2008).

13. Xiong, J., Liu, M.-C. & Yuan, J.-X. 1-(Carboxymethyl)uracil. *Acta Crystallogr. Sect. E Struct. Reports Online* **61**, o2665–o2667 (2005).

14. Tada, M. Antineoplastic Agents. The Preparation of 5-Fluorouracil-1-acetic Acid Derivatives. *Bull. Chem. Soc. Jpn.* **48**, 3427–3428 (1975).

15. Vegas, V. G., Maldonado, N., Castillo, O., Gómez-García, C. J. & Amo-Ochoa, P. Multifunctional coordination polymers based on copper with modified nucleobases, easily modulated in size and conductivity. *J. Inorg. Biochem.* **200**, 110805 (2019).

16. Strovel, J. *et al. Early Drug Discovery and Development Guidelines: For Academic Researchers, Collaborators, and Start-up Companies*. *Assay Guidance Manual* (2004).

17. Acton, C., Miller, R., Maltby, J. & Fullerton, D. Analysis of Variance (ANOVA). in *SPSS for Social Scientists* **6**, 183–198 (Macmillan Education UK, 2009).

18. HERDAN, G. Relation of the Harmonic Mean Particle Size to the Specific Surface of Participate Matter. *Nature* **165**, 858–859 (1950).

LIST OF PUBLICATIONS

Publications discussed in this dissertation

(1) Vegas, V. G.; Lorca, R.; Latorre, A.; Hassanein, K.; Gómez-García, C. J.; Castillo, O.; Somoza, Á.; Zamora, F.; Amo-Ochoa, P. Copper(II)-Thymine Coordination Polymer Nanoribbons as Potential Oligonucleotide Nanocarriers. *Angew. Chemie Int. Ed.* **2017**, *56* (4), 987–991.

(2) Maldonado, N.; Vegas, V. G.; Halevi, O.; Martínez, J. I.; Lee, P. S.; Magdassi, S.; Wharmby, M. T.; Platero-Prats, A. E.; Moreno, C.; Zamora, F.; et al. 3D Printing of a Thermo- and Solvatochromic Composite Material Based on a Cu(II)–Thymine Coordination Polymer with Moisture Sensing Capabilities. *Adv. Funct. Mater.* **2019**, *29* (15), 1808424.

(3) Verónica G. Vegas, Ana Latorre, María Luisa Marcos, Carlos J. Gómez-García, Óscar Castillo, Félix Zamora, Jacobo Gómez-González, José Martínez-Costas, Miguel Vázquez López, Á. S. and P. A.-O. Rational Design of Copper(II)-Uracil Nano-Processed Coordination Polymers to Improve Their Cytotoxic Activity in Biological Media. *ACS Appl. Mater. Interfaces* **2021** (sent).

(4) Vegas, V. G.; Beobide, G.; Castillo, O.; Reyes, E.; Gómez-García, C. J.; Zamora, F.; Amo-Ochoa, P. A Bioinspired Metal–Organic Approach to Cross-Linked Functional 3D Nanofibrous Hydro- and Aero-Gels with Effective Mixture Separation of Nucleobases by Molecular Recognition. *Nanoscale* **2020**, *12* (27), 14699–14707.

Other publications during Ph.D.

(1) Vegas, V.; Villar-Alonso, M.; Gómez-García, C.; Zamora, F.; Amo-Ochoa, P. Direct Formation of Sub-Micron and Nanoparticles of a Bioinspired Coordination Polymer Based on Copper with Adenine. *Polymers.* **2017**, *9* (11), 565.

(2) Vegas, V. G.; Maldonado, N.; Castillo, O.; Gómez-García, C. J.; Amo-Ochoa, P. Multifunctional Coordination Polymers Based on Copper with Modified Nucleobases, Easily Modulated in Size and Conductivity. *J. Inorg. Biochem.* **2019**, *200*, 110805.

LIST OF ABBREVIATIONS

1D: One-dimensional

2D: Two-dimensional

3D: Three-dimensional

4,4'-bipy: 4,4'-bypiridine

5-FUAcOH: 5-fluorouracil-1-acetic acid

AC: Alternate Current

AFM: Atomic Force Microscopy

ATR-FT-IR: Attenuated Total Reflectance-Fourier Transform-Infrared spectroscopy

CB: Conduction band

CP: Coordination Polymer

DC: Direct Current

DFT: Density Functional Theory

DMEM: Dulbecco's Modified Eagle Medium

DMF: Dimethylformamide

DMSO: Dimethylsulfoxide

DOS: Density of States

DR: Diffuse Reflectance

EIS: Electrochemical Impedance Spectroscopy

EoS: Equation of State

EtOH: Ethanol

FE-SEM: Field-Emission Scanning Electron Microscopy

HT: High temperature

LT: Low temperature

MeOH: Methanol

MOA: Metal-Organic Aerogel

MOF: Metal-Organic Framework

MOG: Metal-Organic Xerogel

MOX: Metal-Organic Xerogel

MS: Mass Spectrometry

NCP: Nanoscaled Coordination Polymer

PVDF: Polyvinylidene difluoride

RPMI: Roswell Park Memorial Institute

RT: Room temperature

SEM: Scanning Electron Microscopy

TGA: Thermogravimetric Analysis

THF: Tetrahydrofuran

UV-vis: Ultraviolet-visible spectroscopy

VB: Valence band

VdW: Van der Waals